JOURNAL OF PETROLOGY

Journal of Petrology, 2020, 1–38
doi: 10.1093/petrology/egaa048
Advance Access Publication Date: 20 April 2020
Original Article

OXFORD

Magmatic and Metasomatic Effects of Magma–Carbonate Interaction Recorded in Calc-silicate Xenoliths from Merapi Volcano (Indonesia)

Sean Whitley[1], Ralf Halama[1]*, Ralf Gertisser[1], Katie Preece[2], Frances M. Deegan[3] and Valentin R. Troll[3,4]

[1]School of Geography, Geology and the Environment, Keele University, Keele ST5 5BG, UK; [2]Department of Geography, College of Science, Swansea University, Swansea SA2 8PP, UK; [3]Section for Natural Resources and Sustainable Development (NRHU), Department of Earth Sciences, Uppsala University, 752 36 Uppsala, Sweden; [4]Faculty of Geological Engineering, Universitas Padjajaran (UNPAD), Bandung 40132, Indonesia

*Corresponding author. Telephone: +44 (0) 1782 7 34960; E-mail: r.halama@keele.ac.uk

Received 11 July 2019; Accepted 7 April 2020

ABSTRACT

Magma–carbonate interaction is an increasingly recognized process occurring at active volcanoes worldwide, with implications for the magmatic evolution of the host volcanic systems, their eruptive behaviour, volcanic CO_2 budgets, and economic mineralization. Abundant calc-silicate skarn xenoliths are found at Merapi volcano, Indonesia. We identify two distinct xenolith types: magmatic skarn xenoliths, which contain evidence of formation within the magma; and exoskarn xenoliths, which more likely represent fragments of crystalline metamorphosed wall rocks. The magmatic skarn xenoliths comprise distinct compositional and mineralogical zones with abundant Ca-enriched glass (up to 10 wt % relative to lava groundmass), mineralogically dominated by clinopyroxene ($En_{15\text{-}43}Fs_{14\text{-}36}Wo_{41\text{-}51}$) + plagioclase ($An_{37\text{-}100}$) ± magnetite in the outer zones towards the lava contact, and by wollastonite ± clinopyroxene ($En_{17\text{-}38}Fs_{8\text{-}34}Wo_{49\text{-}59}$) ± plagioclase ($An_{46\text{-}100}$) ± garnet ($Grs_{0\text{-}65}Adr_{24\text{-}75}Sch_{0\text{-}76}$) ± quartz in the xenolith cores. These zones are controlled by Ca transfer from the limestone protolith to the magma and by the transfer of magma-derived elements in the opposite direction. In contrast, the exoskarn xenoliths are unzoned and essentially glass-free, representing equilibration at sub-solidus conditions. The major mineral assemblage in the exoskarn xenoliths is wollastonite + garnet ($Grs_{73\text{-}97}Adr_{3\text{-}24}$) + Ca-Al-rich clinopyroxene ($CaTs_{0\text{-}38}$) + anorthite ± quartz, with variable amounts of either quartz or melilite ($Geh_{42\text{-}91}$) + spinel. Thermobarometric calculations, fluid-inclusion microthermometry and newly calibrated oxybarometry based on $Fe^{3+}/\Sigma Fe$ in clinopyroxene indicate magmatic skarn xenolith formation conditions of ~850 ± 45°C, < 100 MPa and at an oxygen fugacity between the NNO (nickel–nickel oxide) and HM (hematite-magnetite) buffer. The exoskarn xenoliths, in turn, formed at 510–910°C under oxygen-fugacity conditions between NNO and air. These high oxygen fugacities are likely imposed by the large volumes of CO_2 liberated from the carbonate. Halogen- and sulphur-rich mineral phases in the xenoliths testify to infiltration by a magmatic brine. In some xenoliths, this is associated with the precipitation of copper-bearing mineral phases by sulphur dissociation into sulphide and sulphate, indicating potential mineralization in the skarn system below Merapi. The compositions of many xenolith clinopyroxene and plagioclase crystals overlap with that of magmatic minerals, suggesting that the crystal cargo in Merapi magmas may contain a larger proportion of skarn-derived xenocrysts than previously recognized. Assessment of xenolith formation timescales demonstrates that magma–carbonate interaction and associated CO_2 release could affect eruption intensity, as recently suggested for Merapi and similar carbonate-hosted volcanoes elsewhere.

Key words: Merapi; magma–carbonate interaction; skarn; xenolith; carbonate assimilation; oxybarometry

INTRODUCTION

Calc-silicate (skarn) xenoliths are found within the deposits of many hazardous arc volcanoes worldwide, including Popocatépetl (e.g. Goff *et al.*, 2001), Vesuvius (e.g. Fulignati *et al.*, 2001), Merapi (e.g. Chadwick *et al.*, 2007), Colli Albani (e.g. Di Rocco *et al.*, 2012) and Nisyros (Spandler *et al.*, 2012). Formed as a result of interaction between crustal carbonate and the host magmatic system, these xenoliths preserve evidence of complex reaction processes that can have a profound impact on the host magmatic system, including altering magmatic differentiation paths (e.g. Iacono-Marziano *et al.*, 2008), influencing eruptive dynamics (e.g. Freda *et al.*, 2011; Troll *et al.*, 2012; Caricchi et al., 2018; Carr *et al.*, 2018), and liberating large volumes of crustal CO_2 into the atmosphere (e.g. Mason *et al.*, 2017).

Our knowledge about crustal magma–carbonate interaction processes has been derived from diverse approaches. Isotope mass-balance calculations (e.g. Troll *et al.*, 2012, 2013; Jolis *et al.*, 2015) have shown that crustal carbonate makes up a large percentage (up to 30%) of the volume of some volcanic systems , and in situ stable isotopes have demonstrated that decarbonation is highly efficient in magmatic systems (Whitley *et al.*, 2019). Experimental magma–carbonate studies (e.g. Iacono-Marziano *et al.*, 2008; Deegan *et al.*, 2010; Jolis *et al.*, 2013; Blythe *et al.*, 2015; Carter & Dasgupta, 2016) have further demonstrated how magmatic melt differentiation paths are modified towards silica undersaturation in mafic melts, and that magma–carbonate interaction may be extremely rapid (syn-magmatic), operating on the order of minutes to hours. Moreover, detailed petrographical and geochemical studies of individual xenoliths have provided insights into the architecture of subvolcanic skarn contact aureoles (Matthews *et al.*, 1996; Fulignati *et al.*, 2004), the depth of magma–carbonate interaction from fluid inclusions (Clocchiatti *et al.*, 1982), xenocryst incorporation into the magma and skarn recycling (Chadwick *et al.*, 2007; Jolis *et al.*, 2015), changes in magmatic redox conditions and phase equilibria (Wenzel *et al.*, 2002), and the economic metallogenic potential of magmatic fluids that interact with the country rock (Fulignati *et al.*, 2013).

In this study, we present a detailed analysis of the petrography, mineralogy and geochemistry of calc-silicate xenoliths from the 1994–2010 eruptions of Merapi volcano, Indonesia. We demonstrate that these xenoliths either represent fragments of the complete replacement of carbonate wall rock with calc-silicate mineral assemblages around the magma reservoir margins, or are transient fragments of entrained carbonate that are caught in the process of being metamorphosed within the magma itself. The xenoliths record evidence of interaction with a magmatic-derived halogen-bearing fluid that produced exotic halogen-bearing mineral phases whilst enriching the xenoliths in economically important metals such as copper and iron, and by analogy similar processes can be inferred to have affected the more extensive skarn system below Merapi. We also show that traditional mineral-melt thermobarometry and fluid-inclusion analysis can be applied to some of the xenoliths, and we present a new calibration of a single clinopyroxene crystal oxybarometer to determine the intensive variables (T, P, fO_2) during xenolith formation.

GEOLOGICAL BACKGROUND

Merapi is the most active of Indonesia's volcanoes, and is considered one of the Sunda Arc's most dangerous (e.g. Voight *et al.*, 2000; Gertisser *et al.*, 2011, 2012; Surono *et al.*, 2012). Activity is nearly continuous, with periods of dome growth frequently interrupted by gravitational dome collapse and associated pyroclastic density currents (e.g. Andreastuti *et al.*, 2000; Camus *et al.*, 2000; Newhall *et al.*, 2000; Voight *et al.*, 2000; Gertisser *et al.*, 2012). Larger explosive Vulcanian and sub-Plinian eruptions occur at longer ~100-year timescales, such as the 2010 VEI 4 eruption, which killed close to 400 people (Surono *et al.*, 2012; Komorowski *et al.*, 2013). Compositionally, the erupted material is medium- to high-K basalt to basaltic andesite with a restricted range of ~49 to 58 wt % SiO_2 (Gertisser & Keller, 2003a, 2003b). Early work at Merapi suggested a subducted sediment contamination component to the Merapi magmas (Gertisser & Keller, 2003b), while subsequent work also highlighted a significant influence from crustal carbonate on magma genesis (e.g. Chadwick *et al.*, 2007; Troll *et al.*, 2013; Aiuppa *et al.*, 2017). Merapi overlies an upper crust of 8 to 11 km thick sediments of the Kendeng basin, where Cretaceous to Cenozoic volcaniclastic sediments are overlain by shallow marine limestones and marls, all of which overlie inferred Cretaceous arc and ophiolite basement rocks (van Bemmelen, 1949; Smyth *et al.*, 2005). Fragments of the sedimentary basement are frequently found as thermally metamorphosed xenoliths within the eruptive deposits (Brouwer, 1928; Clocchiatti *et al.*, 1982; Camus *et al.*, 2000; Gertisser and Keller, 2003b; Chadwick *et al.*, 2007; Troll *et al.*, 2012, 2013). These xenoliths testify to prevalent magma–carbonate interaction (Chadwick *et al.*, 2007; Troll *et al.*, 2013; Whitley *et al.*, 2019), a process that is ongoing and occurs on rapid timescales (Deegan *et al.*, 2010, 2011; Troll *et al.*, 2012; Reagan *et al.*, 2017). Radiogenic ($^{87}Sr/^{86}Sr$) and stable ($\delta^{13}C$, $\delta^{18}O$) isotope analysis of bulk xenoliths and mineral separates of calc-silicate mineral phases (wollastonite, diopside, calcite)

have been used to demonstrate up to 30% crustal carbonate assimilation during the genesis of Merapi magmas (Chadwick *et al.*, 2007; Troll *et al.*, 2013; Whitley *et al.*, 2019). The liberation of large volumes of crustal CO_2 during syn-magmatic activity has additionally been linked to increased eruptive explosivity at Merapi (e.g. Troll *et al.*, 2012, 2013; Borisova *et al.*, 2013; Carr *et al.*, 2018). The available evidence thus indicates that magma–carbonate interaction at Merapi may have wide-ranging implications for the magmatic evolution and volcanic hazard potential at Merapi.

METHODS

Scanning electron microscopy was undertaken at Keele University, UK, using a Hitachi TM3000 scanning electron microscope (SEM). A rare unknown mineral found in sample MX1, compositionally similar to wadalite, was analysed with Raman spectroscopy at Keele University using a confocal Thermo Scientific DXR Raman spectrometer with a 532 nm laser, a 50× objective, and a standard 30 μm uncovered polished thin section.

Microthermometry was carried out at Keele University using a Linkam THMS600 freezing-heating stage. Thermocouples were calibrated at –56.6°C, 0.0°C and +374.1°C using synthetic fluid inclusions provided by Linkam. The precision of temperature measurements at –56.6°C is ±0.1°C, and it is ±2°C at 374.1°C. Measurements were made on ~100 μm thick double polished wafer fragments.

Major-element concentrations in minerals, and major-element, chlorine and sulphur concentrations in groundmass glasses and melt inclusions were determined with a JXA 8900R electron probe microanalyser (EPMA) at the University of Kiel, Germany. Silicate and oxide minerals were analysed with a 15 kV accelerating voltage, a 15 nA beam current and a 2 μm beam diameter. Calcite was measured with a 15 kV accelerating voltage, a 10 nA beam current and a 7 μm beam diameter. Glasses were measured with a 15 kV accelerating voltage, a 12 nA beam current and a 5 μm beam diameter. Measurement times were 15 s at the peak and 7 s on the background, excluding S, Cl, P, which were measured for 30 s at the peak and 10 s on the background. Extended counting times of 30 s on the peak and 10 s on the background for Fe, Mg and Mn, and 60 s on the peak and 30 s on the background for Ba and Sr were applied during calcite analyses. Na was measured first to minimize alkali migration. Natural mineral standards were used for calibration, and Smithsonian basaltic glass A-99, forsterite 83 USNM2566, plagioclase USNM115900, garnet RV2 USNM 87375 and obsidian ASTIMEX Block SPGLASS7 were used as secondary within-run standards to assess accuracy and precision, as presented in the Supplementary Data, which may be downloaded from http://www.petrology.oupjournals.org.

All Mg# values were calculated assuming all Fe as Fe^{2+} using $Mg = 100\frac{Mg}{Mg+Fe_{total}}$. Ternary clinopyroxene components were calculated assuming all Fe as Fe^{2+}, e.g. $Fs = 100\frac{Fe_{total}}{Mg+Fe_{total}+Ca}$. Fe^{3+} was estimated for clinopyroxene from stoichiometry using Droop (1987). Al^{IV} was calculated as 2-Si, and any remaining Al was allocated as Al^{VI}. Components for clinopyroxene thermobarometry were calculated using Putirka *et al.* (1996). Garnet end-member mole fractions and Fe^{3+} were estimated using the Arai (2010) R script implementation of the Muhling & Griffin (1991) calculation scheme, which provides a more accurate Fe^{3+} estimate for garnet than Droop (1987). Melilite mole fractions were calculated considering four end-members by first allocating Na to the Na-melilite end-member, and then the remaining cations, minus the Al required for Na-melilite, were allocated between gehlenite, åkermanite and Fe-åkermanite. These mole fractions were calculated as follows (abbreviations as in Table 1):

$$\mathrm{Na-Mel} = \frac{Na}{Na + Ca - 1}$$

$$\mathrm{Geh} = (1 - \mathrm{Na} - \mathrm{Mel}) \cdot \frac{\frac{Al-2Na}{2}}{\frac{Al-2Na}{2} + Fe + Mg}$$

$$\mathrm{Ak} = (1 - \mathrm{Na} - \mathrm{Mel}) \cdot \frac{Mg}{\frac{Al-2Na}{2} + Fe + Mg}$$

$$\mathrm{Fe-Ak} = (1 - \mathrm{Na} - \mathrm{Mel}) \cdot \frac{Fe}{\frac{Al-2Na}{2} + Fe + Mg}$$

Owing to the small size of most xenoliths (typically < 5 cm), combined with the textural and mineralogical uniqueness of each sample, whole-rock compositions for six representative xenoliths were determined by point counting (1000–2000 points) combined with averaged mineral and glass chemistry. Each zone was counted individually, and then the respective areas of the zones were combined to calculate a whole-rock composition. The zone and whole-rock compositions were corrected for varying mineral densities using mineral densities from Deer *et al.* (1997), and the bulk compositions were obtained using the Rock-Maker spreadsheet (Büttner, 2012), which generates bulk compositions from mineral volumes. All calculated compositions are presented in the Supplementary Data.

Thermodynamic modelling of the exoskarn samples MX99-5s and MX99-3s was undertaken using the Theriak-Domino software (build date 3-1-2012, de Capitani & Petrakakis, 2010), using calculated whole-rock compositions (see above) in the system Si-Al-Fe-Mg-Ca-C. The database used (Holland & Powell, 1998, version 5.5) lacks solid-solution models that include the CaTs component in clinopyroxene, and mixing between gehlenite and åkermanite. Therefore, ideal mixing was assumed for these two solid solutions (Charlu *et al.*, 1981; Povoden *et al.*, 2002). Implementing a CaTs-DiHd

Table 1: Mineral phases identified within the Merapi calc-silicate xenoliths in this study, and abbreviations used throughout the text.

Mineral	Abbreviation	Formula	Mag	Exo A	Exo B
Rock-forming and their end-members					
Clinopyroxene	Cpx	$Ca(Fe,Mg)Si_2O_6$	M		
–Calcium Tschermak's Pyroxene	CaTs	$CaAlAlSiO_6$	m	M	M
–Esseneite (Clinopyroxene)	Ess	$CaFe^{3+}AlSiO_6$	m	M	M
Garnet	Grt	$Ca_3(Fe^{3+},Al,Ti)_2Si_3O_{12}$	m	M	M
–Andradite	Adr	$Ca_3Fe_2^{3+}Si_3O_{12}$	m	M	m
–Grossular	Grs	$Ca_3Al_2Si_3O_{12}$	m	M	M
–Schorlomite	Sch	$Ca_3Ti_2Si_3O_{12}$	m		
Melilite					
–Åkermanite	Åk	$Ca_2MgSi_2O_7$	m	m	M
–Fe-Åkermanite	Fe-Åk	$Ca_2FeSi_2O_7$	m	m	M
–Gehlenite	Gh	$Ca_2Al_2SiO_7$	m	m	M
–Na-Melilite	Na-Mel	$CaNaAl_2SiO_7$			
Plagioclase	Pl	$(Ca,Na)(Al,Si)_4O_8$	M	M	m
–Anorthite	An	$CaAl_2Si_2O_8$	M	M	m
Wollastonite	Wo	$CaSiO_3$	M	M	m
–Ferrobustamite	Bst	$Ca(Fe^{2+},Ca,Mn^{2+})Si_2O_6$	m	m	
Sulphur- and halogen-bearing					
Anhydrite	Anh	$CaSO_4$	m	m	
Apatite	Ap	$Ca_5(PO_4)_3(OH,F,Cl)$	m		
Baryte	Ba	$BaSO_4$	m		
Cotunnite*	Cot	$PbCl_2$	m		
Cubanite	Cu	$CuFe_2S_3$	m		
Cuspidine	Cusp	$Ca_4Si_2O_7(F,OH)_2$	m	m	
Ellestadite	El	$Ca_5(SiO_4,PO_4,SO_4)_3(F,OH,Cl)$		m	m
Fluorite	Fl	CaF_2	m		
Larnite	Lrn	Ca_2SiO_4		m	
Pyrrhotite	Po	$Fe_{1-x}S$ (x=0-0.2)	m	m	
Spurrite	Spu	$Ca_5Si_2O_8CO_3$		m	
Wadalite†	Wad	$Ca_{12}Al_{10}Si_4O_{32}Cl_6$	m		
Oxides, other silicates, and accessory minerals					
Calcite	Cal	$CaCO_3$	m	M	
Ca-Zr-Ti oxide*	CaZrTi	Ca-Zr-Ti	m		
Cebollite†	Ce	$Ca_5Al_2(SiO_4)_3(OH)_4$		m	
Chromite*	Chr	$FeCr_2O_4$	m		
Hematite	Hm	Fe_2O_3		m	
Ilmenite	Ilm	$FeTiO_3$	m		
Magnetite	Mgt	$Fe^{2+}Fe_2^{3+}O_4$	M	m	
Quartz	Qtz	SiO_2	M	m	
Monazite*	Mo	$(Ce,La)PO_4$		m	
Perovskite	Psk	$CaTiO_3$	m		
Titanite	Ttn	$CaTiSiO_4$	m	m	
Spinel	Sp	$(Fe,Mg)Al_2O_4$			M
Xenotime*	Xe	YPO_4		m	

*Identified with SEM only; † uncertain identification.
Abbreviations: Mag, magmatic skarn xenoliths; Exo A, exoskarn type-A xenoliths; Exo B, exoskarn type-B xenoliths; M, major rock-forming mineral; m, minor to accessory (<1 vol%) mineral.

ideal mixing model for clinopyroxene over the default database model has, however, little effect on the calculated phase boundaries of the system. For example, this clinopyroxene model produces only a ~20°C variation in melilite–garnet phase boundaries, which is relevant to the xenoliths.

PETROGRAPHY

Calc-silicate xenoliths (n=33) collected from the 1994 to 2010 eruption deposits at Merapi can be subdivided into three distinct groups (magmatic skarn, n=25; exoskarn, n=5; and buchite, n=3) on the basis of their dominant mineralogy, modal zonation, and the presence of glass. Twelve xenoliths that best represent the three groups, and which highlight the mineralogical and textural variety of the xenoliths, were chosen for detailed study. The xenoliths are generally centimetres to tens of centimetres in size, and texturally complex variations in mineralogy and zonation can be seen at hand-specimen scale. Volcaniclastic and metasedimentary xenoliths are additionally present at Merapi but not discussed in this paper (see Chadwick *et al.*, 2007). A summary of the mineral phases identified in this study and their formulas are presented in Table 1.

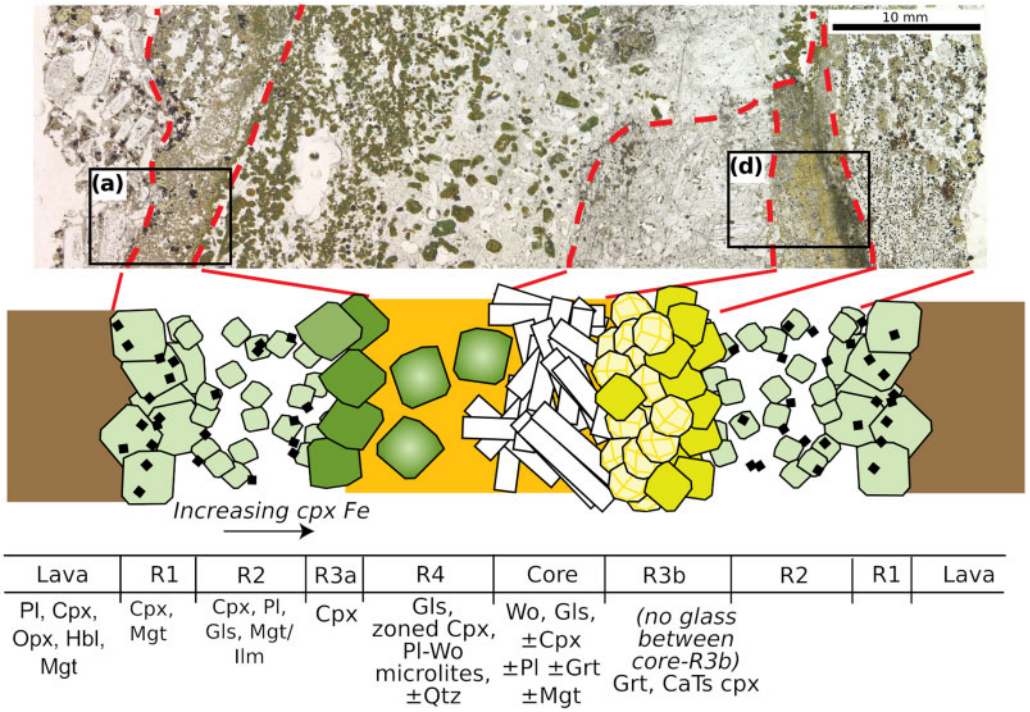

Fig. 1. Zoning in sample MX1 (thin section) and idealized diagram for zoning patterns in the magmatic skarn xenoliths. Highlighted zones (a) and (d) correspond to the respective panels in Fig. 2. See Table 1 for all mineral abbreviations used. Gls: interstitial Ca-rich glass.

Magmatic skarn xenoliths

The most abundant calc-silicate xenolith type (n=25) is the one we term 'magmatic skarn' (cf. Fulignati *et al.*, 2004), based on the abundance of Ca-enriched magmatic glass, melt inclusions in the newly formed calc-silicate skarn minerals, and pronounced reaction zones at contacts with the host lava. In an attempt to explain the variety of xenoliths in this group, we subdivided the magmatic skarn xenoliths into a series of idealized mineralogical/textural zones, such as a series of reaction zones and a core zone (Figs. 1, 2). The lava contact (R1) is represented by a zone of coarse (100–300 μm), pale green clinopyroxene and a concentration of magnetite (Fig. 2a). This is followed by a finer-grained (up to 100 μm) zone (R2) of plagioclase + clinopyroxene ± glass (Fig. 2a), with rare amphibole also present in sample MX1. This zone grades into a zone of coarse, dark green/yellow pleochroic clinopyroxene (R3), separating R2 from a zone of vesicular glass (R4) (Fig. 2a, b). The glass zone typically contains strongly irregularly Fe-Mg zoned (see mineral chemistry), colourless to deep green/yellow pleochroic diopsidic clinopyroxene crystals (Fig. 2b). These clinopyroxene crystals are similar to those of zone R3, and often appear to be incorporated from zone R3. Plagioclase and wollastonite microlites are additionally present within the glass. Sample MX5 has comparatively large quartz and plagioclase crystals (~100 μm) within the glass zone, and sample MX3 shows this zone to be almost fully crystallized to quartz and plagioclase, with scarce melt inclusions within the quartz crystals. The xenolith core (Fig. 2c) has a sharp contact to decussate wollastonite, but occasionally the core is a mixture of wollastonite, clinopyroxene, and accessory garnet. Additionally, glass is often present within the core of these xenoliths. At glass–wollastonite contacts, a thin rim of semi-dendritic ferrobustamite often forms. The samples have a vesicular texture across all zones.

The described zonation is idealized, and variations naturally occur. Samples MX1 and M13-10, for instance, show no glass zone (R4) separating the wollastonite-dominant core from R3 and R2. In this case, a pale yellow clinopyroxene and garnet zone formed instead of the coarse clinopyroxene of zone R3, which we call R3b (Figs. 1, 2d). This clinopyroxene is optically and chemically distinct (CaTs: $CaAlAlSiO_6$-rich, see the section Mineral Chemistry) from any others in the Merapi magmatic skarn xenoliths. In sample MX1, one half of the xenolith shows the common zonation (with glass zone R4 present), whilst the other half has no glass and instead has the zone R3b CaTs clinopyroxene and garnet zone (Fig. 1). Rare patches of garnet are found interstitial to wollastonite in the MX1 core, and also together with wollastonite and CaTs clinopyroxene in sample CS16.

Accessory phases are generally restricted to the xenolith cores, and include calcite, titanite, chromite, gehlenite, a wadalite-like Si-Al-Fe-Ca-O-Cl mineral,

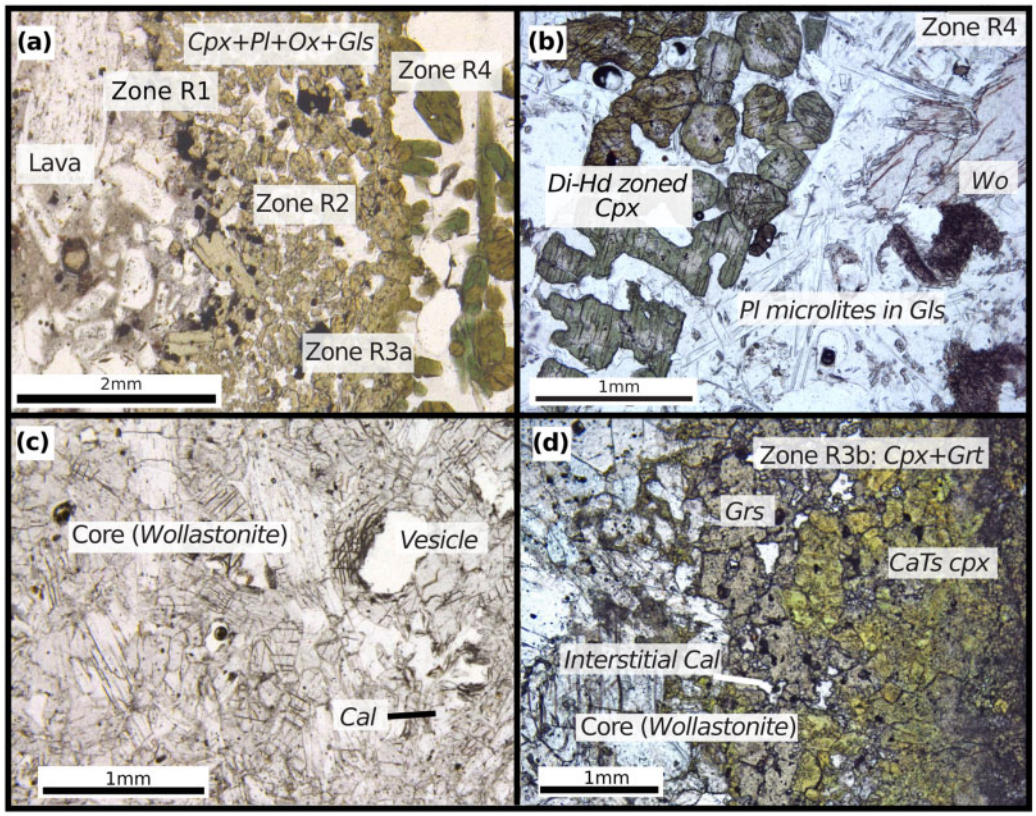

Fig. 2. Examples of the respective zones in magmatic skarn xenoliths. (a) Host lava contact and zones R1 to R4. Note the progressive darkening of the clinopyroxene colour due to the changing composition to iron enrichment. Sample MX1. (b) Normally zoned diopside-hedenbergite clinopyroxene within glass-dominant zone R4. Also present are plagioclase microlites and wollastonite. Sample CS2. (c) Wollastonite-dominant xenolith core with vesicles and accessory calcite. Sample MX5. (d) Zone R3b, showing garnet + CaTs clinopyroxene formation where there is no glass zone R4 between the core and zone R2. Sample MX1. See Table 1 for mineral abbreviations. Gls: interstitial Ca-rich glass.

perovskite, a Ca-Zr-Ti-O mineral, cotunnite, sulphates (anhydrite and baryte) and sulphides (pyrrhotite and cubanite) (Table 1). Titanite is also present within the glass in zone R4, and ilmenite is exclusively found in sample MX3 in zone R2. Calcite is present as four distinct textural types: (1) globular crystals within the glass R4 zone, (2) interstitial to wollastonite in the cores, (3) inclusions in wollastonite and garnet, and (4) a melt-like infiltrative texture containing rare Cl-F-rich phases such as fluorite, cuspidine and the wadalite-like mineral within regions where the calcite pools (Fig. 3a, b). These calcites are discussed in detail in Whitley *et al.* (2019).

Many crystals contain significant quantities of melt inclusions. (Fig. 3c–g), exceeding 80 in a single 600-μm-long wollastonite crystal. Melt inclusions are also present in clinopyroxene in zones R3–4, plagioclase in zone R4 and titanite within the xenolith cores. The inclusions are most commonly glassy and have a single shrinkage bubble, but, in rare cases, they can contain daughter crystals and multiple bubbles. The daughter crystals are found either in the glass or in the bubble, and are most commonly Fe-bearing phases (pyrrhotite, cubanite, magnetite) and occasionally apatite. Vapour-rich CO_2 fluid inclusions are also common in wollastonite.

Exoskarn xenoliths

Exoskarn xenoliths are distinct from the magmatic skarn xenoliths by having a different mineralogy, lacking mineralogical zonation, and by almost entirely lacking glass. On the basis of their mineral assemblages, which resemble typical high-temperature skarns worldwide (e.g. Meinert, 1992), and the lack of glass, which indicates formation by subsolidus reactions, we classify these xenoliths as exoskarns (cf. Fulignati *et al.*, 2004, see also Discussion). These xenoliths comprise two distinct skarn mineral assemblages (A and B), often with a rim of clinopyroxene and plagioclase at the host lava contact. The most common assemblage (A) is wollastonite + garnet + plagioclase ± CaTs clinopyroxene ± quartz ± calcite with a granoblastic texture (Fig. 4a). Some clinopyroxenes and garnets exhibit weak, patchy zonation. Accessory S, Cl, and F-bearing phases such as cuspidine, ellestadite, anhydrite and pyrrhotite are additionally present, and also unidentified Ca-Al-Si-Cl-F minerals that are distinct from the wadalite-like mineral in the magmatic skarn xenoliths. No hydrous phases that can often occur in skarns, such as epidote and vesuvianite (cf. Meinert, 1992), have been identified in this study, although epidote and prehnite have been

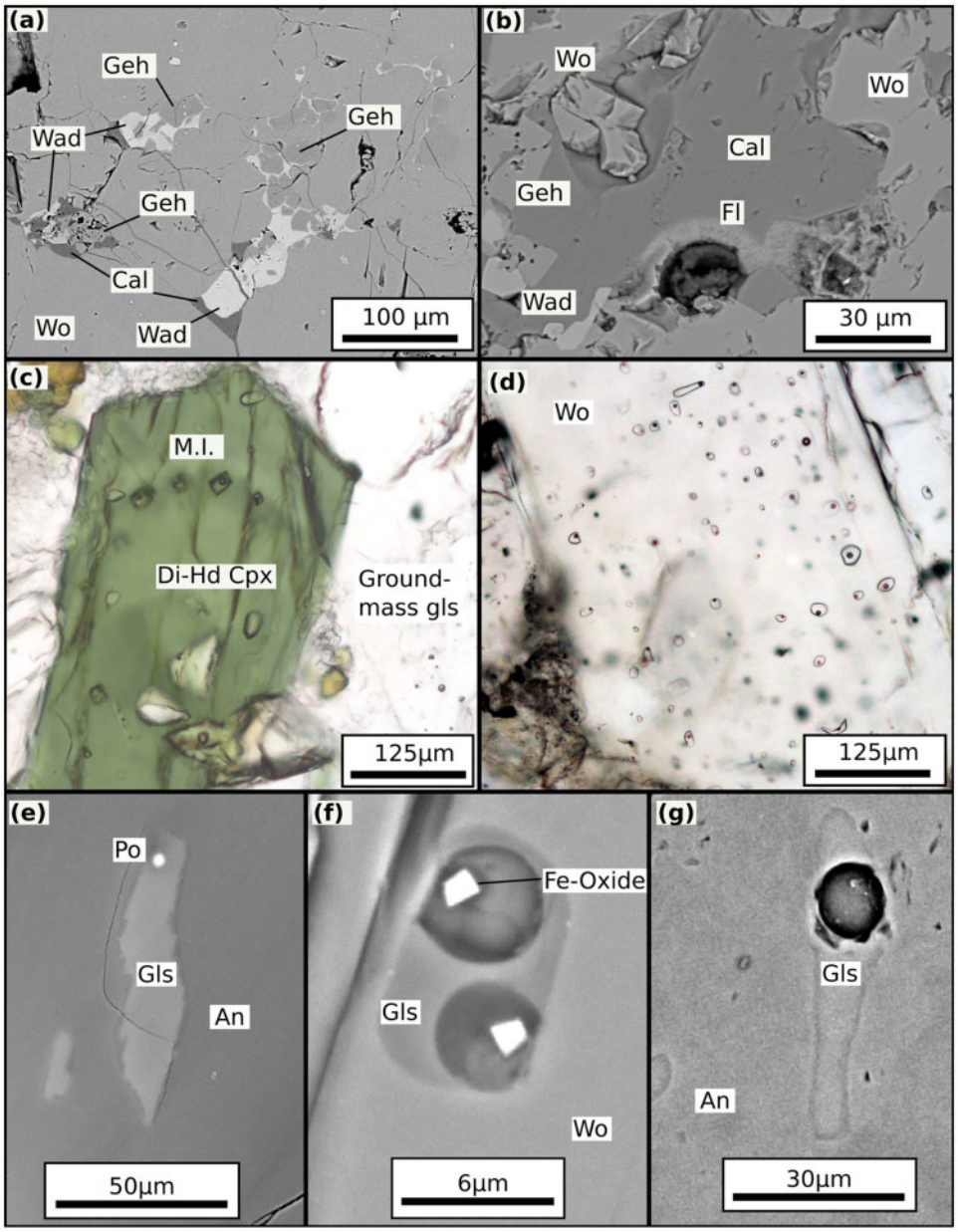

Fig. 3. Magmatic skarn accessory minerals and melt inclusions. All images are from sample MX1, apart from panels (e) and (g), which are from sample CS16. (a, b) Accessory gehlenite, fluorite, calcite and the wadalite-like mineral in the xenolith core. (c–g) Examples of wollastonite, clinopyroxene and plagioclase-hosted melt inclusions, showing variable abundance and textural forms. Mineral abbreviations as in Table 1. M.I.: melt inclusions; Gls: interstitial Ca-rich glass.

identified in earlier descriptions of Merapi xenoliths (Kerinec, 1982; Camus *et al.*, 2000). Garnet often contains inclusions of plagioclase and wollastonite. Calcite is present either as rare inclusions within garnet crystals or as large millimetre-sized crystals, surrounded by complex reaction rims that contain larnite, spurrite, and Ca-Si-rich S-Cl-F-bearing phases including fluorite, cuspidine, ellestadite, anhydrite, and many additional unidentified phases (Ca-Si-O, Ca-Al-Si-O, Ca-Al-Si-P-O Table 8, Fig. 4b). Xenotime and monazite form accessory inclusions within these calcites.

The second assemblage (B), found in only one sample (MX99-3s), comprises gehlenite + grossular garnet + CaTs clinopyroxene + spinel + wollastonite + plagioclase, with trace amounts of ellestadite (Fig. 4c). This sample shows evidence for disequilibrium, such as patchy compositional zoning of garnets, and spinel with rims of gehlenite followed by an outer rim of CaTs clinopyroxene. Patches of localized equilibrium are shown by granular ~120° triple junctions in the gehlenite-dominant areas of the sample.

Buchite

These rare xenoliths (samples M13-04C, CS14, CS10) contain abundant (> 70 vol. %) quartz (or SiO_2 polymorphs) with interstitial glass around the crystal

borders, and minor small interstitial clinopyroxene, plagioclase and wollastonite (Supplementary Fig. S1). Patches of clinopyroxene-rich glass are present, similar to zone R4 of the magmatic skarn xenoliths. We have classified these samples as buchites (pyrometamorphic glass-rich rocks), following the classification by Matthews *et al.* (1996) of texturally similar xenoliths at Lascar volcano, Chile. Similar quartz-rich, partially melted xenoliths have also been described from the Aeolian islands (e.g. Frezzotti *et al.*, 2004; Zanon & Nikogosian, 2004; Del Moro *et al.*, 2011), Etna (Mollo *et al.*, 2017) and the Central Apennines (Melluso *et al.*, 2003). Although the quartz-rich assemblage could be derived from a volcaniclastic protolith, the presence of wollastonite suggests a carbonate or marl component. The rounded shape of the quartz crystals, separated by interstitial glass, indicates that partial melting has occurred. The dissolution of quartz xenocrysts in arc magmas was observed in products of the 1991 Pinatubo eruption, where highly silicic glass (~80–85 wt % SiO_2) formed in reaction zones around the xenocrysts, pointing to possible compositional modifications of the melt, at least on a micrometre scale (Borisova *et al.*, 2014). However, although the Merapi buchite xenoliths are briefly mentioned here for completeness, details of their occurrence and the potential ramifications for melt chemistry at Merapi are beyond the scope of the current study and will not be discussed further.

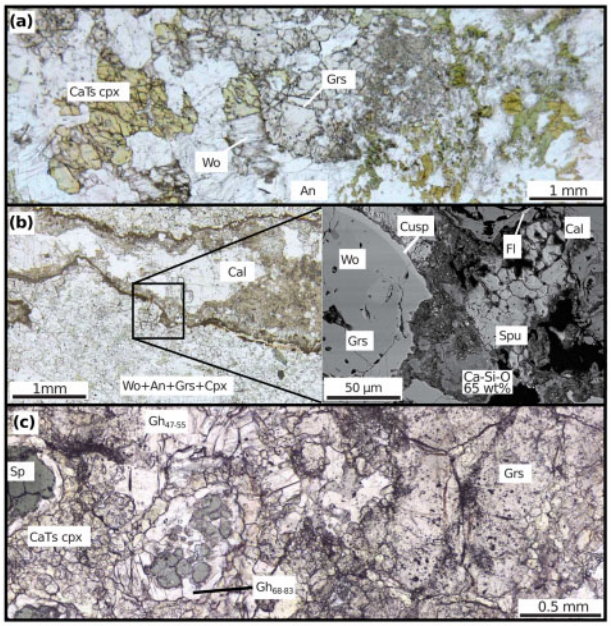

Fig. 4. Typical textures in exoskarn xenoliths. (a) CaTs-cpx + Wo + An + Grs in exoskarn type-A xenolith MX99-5s. (b) Large residual calcite crystals in exoskarn type-A xenolith CS11. The expanded image shows the complex decarbonation textures and reactions occurring influenced by a F-rich fluid. A Ca-Si-O phase is present with low analytical totals (~65 wt %). (c) Exoskarn type-B xenolith MX99-3s shows a unique assemblage of spinel, gehlenite, CaTs-cpx, grossular, with accessory wollastonite and anorthite. Spinel is rimmed by gehlenite followed by CaTs-cpx. For mineral abbreviations, see Table 1.

RESULTS

Whole-rock major-element chemistry

Calculated major-element compositions of individual zones in magmatic xenoliths are compared for two selected samples to evaluate chemical changes (Fig. 5). There are distinct differences between the zones, and some systematic variations from the lava contact towards the xenolith cores point to a progressive change from magmatic to calcic compositions (Fig. 5a; Supplementary Figs. S2, S3) (cf. Troll *et al.*, 2012). CaO contents are lowest in the lavas and highest in the xenolith cores, whereas Al_2O_3 contents show exactly the opposite behaviour. One xenolith (sample MX1) shows a systematic increase in CaO from the contact towards the core, except for glass zone R4 which creates a distinct anomaly in the element profiles, having higher SiO_2 and lower CaO than the adjacent zones. FeO is relatively enriched in zone R1, decreasing towards the core, whereas SiO_2 is lowest in this zone. MgO shows only limited variation and has the lowest contents in the innermost zone (R4) and in the core.

In terms of whole-rock major-element composition (Fig. 5b), magmatic skarn xenoliths fall within the range of xenoliths analysed by Chadwick *et al.* (2007), which we believe classify as magmatic skarn xenoliths in our grouping, forming diverging trends from basaltic-andesite compositions. Magmatic skarn xenoliths have lower Al_2O_3 contents than lavas (< 16 wt %), while exoskarn xenoliths display Al_2O_3 contents comparable to lava values (18 to 25 wt %), although at a much lower SiO_2 content (33 to 45 wt %). All xenoliths have much higher CaO than the lavas, up to 36 wt %, but lower TiO_2 and K_2O contents. FeO and MgO span the range of lava values, with FeO up to 10.0 wt %, and MgO up to 6.6 wt %. Exoskarn xenoliths generally plot distinct from magmatic skarn xenoliths when considered with the Chadwick *et al.* (2007) data (Fig. 5b). For instance, the exoskarn xenoliths have low SiO_2, TiO_2 and FeO relative to the magmatic skarn xenoliths, but form a linear trend of decreasing TiO_2 and FeO with increasing SiO_2.

Mineral chemistry

Feldspar

Feldspar compositions in the Merapi calc-silicate xenoliths are entirely plagioclase, but span a wide compositional range (An_{46-100}) (Table 2). In magmatic skarn xenoliths, anorthite content progressively increases towards the xenolith cores (Fig. 6a). Zoning within individual crystals is relatively insignificant compared with the differences between magmatic skarn zones. Magmatic skarn xenolith plagioclase comprises both microlites (An_{46-59}) within the interstitial glass in zone R4, and interstitial plagioclase in the high-An cores (An_{73-100}). Where analyses of the host lava attached to the xenolith were possible (An_{29-81}), plagioclase in zones R2 and R4 overlap magmatic plagioclase compositions, including

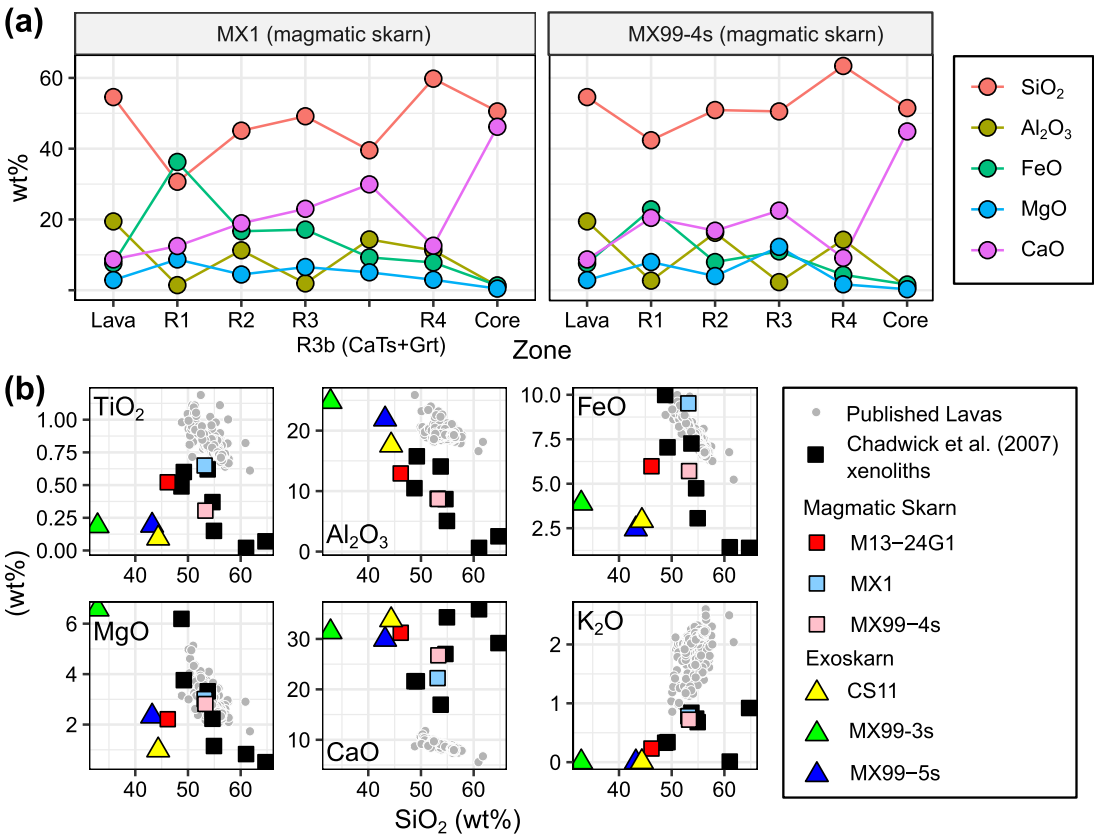

Fig. 5. Xenolith whole-rock geochemistry (calculated from mineral modes and mineral chemistry, corrected for mineral densities using data from Deer *et al.* (1997) and the Rock-Maker spreadsheet (Büttner, 2012)). (a) Profiles through the distinct zones of two magmatic xenoliths. (b) Calculated whole-rock compositions of bulk xenoliths compared with published lava and xenolith data. Published volcanic whole-rock data are from Nadeau *et al.* (2013b), Borisova *et al.* (2013), Costa *et al.* (2013), Innocenti *et al.* (2013) and the GEOROC database (http://georoc.mpch-mainz.gwdg.de/georoc/, accessed 03/2019). Published Merapi calc-silicate xenoliths from Chadwick *et al.* (2007).

the previously published data (Gertisser, 2001; Preece, 2014; Erdmann *et al.*, 2016). In An–FeO space, xenolith core plagioclase compositions generally fall within and extend the high FeO–An compositional ellipse of Merapi xenolith plagioclase from Chadwick *et al.* (2007) (Fig. 6b). Plagioclase microlites within the zone R4 glass have strong FeO enrichment (up to 1.7 wt % FeO), as is observed with the strong FeO enrichment of both clinopyroxene and ferrobustamite overgrowths on wollastonite within this glass zone (see below). Exoskarn plagioclase is essentially pure anorthite, with lower anorthite contents restricted to the lava contact (Table 2). FeO concentrations in exoskarn anorthite are characteristically lower than those in magmatic plagioclase and the majority of the magmatic skarn plagioclase data.

Clinopyroxene

Clinopyroxene compositions range from quadrilateral diopside-hedenbergite (DiHd) (Morimoto, 1988) to high-Al diopside (Table 3). These high-Al clinopyroxenes are enriched both in esseneite ($CaFe^{3+}AlSiO_6$) and in calcium Tschermak's (CaTs: $CaAlAlSiO_6$) components, demonstrated by the strong correlation between Fe^{3+} and Al^{IV} (R^2=0.88, Fig. 7a), and Al^{IV} with Al^{VI} (R^2=0.81, not shown) across all analysed crystals. Incorporation of Al^{IV} is accommodated by a strong reduction of Si in the tetrahedral site. These clinopyroxenes are commonly generalized as fassaite [$Ca(Mg,Fe^{3+},Al)(Si,Al)_2O_6$] where $Al^{IV} > 0.25$; Deer *et al.* (1997)]. As this is not a formal name (Morimoto, 1988) and the clinopyroxenes show an enrichment in the CaTs component, we refer to these clinopyroxenes as CaTs-clinopyroxene in this paper.

In magmatic skarn xenoliths, the clinopyroxene compositions are generally comparable to Merapi magmatic clinopyroxenes in zone R1 (Fig. 7a–c), and progressively become more Ca/wollastonite-rich until sitting along the diopside–hedenbergite (Di–Hd) join (Wo_{50}) in zones R3, R4 and in the core (Fig. 7c). There is a sharp compositional change at zone R4 and within the core, where the clinopyroxenes closely follow the Di–Hd join and progressively become more Hd-rich (Fig. 7c). Xenolith core clinopyroxenes can also be enriched in Al_2O_3 (up to 11.57 wt %, corresponding to 18 mol % CaTs), bringing compositions above the Di–Hd join in the traditional clinopyroxene composition

Table 2: Average plagioclase compositions for the zones in the magmatic skarn xenoliths and in the exoskarn xenoliths.

Type	Magmatic skarn				Exoskarn	
Zone	Host lava	R2	R4	Core	Exoskarn A	Exoskarn B
n	8	49	27	76	63	7
SiO_2	53.61 (4.03)	48.91 (4.42)	52.91 (4.28)	45.21 (2.80)	44.43 (3.50)	42.51 (0.51)
Al_2O_3	28.10 (2.94)	31.73 (3.31)	28.68 (3.00)	33.98 (2.03)	34.90 (2.48)	36.55 (0.37)
FeO	0.72 (0.34)	0.58 (0.16)	0.94 (0.33)	0.65 (0.22)	0.33 (0.33)	0.24 (0.02)
MgO	0.06 (0.07)	0.02 (0.02)	0.02 (0.03)	0.01 (0.02)	0.02 (0.02)	
CaO	11.12 (3.28)	15.05 (3.72)	12.25 (2.99)	17.82 (2.18)	19.09 (2.63)	20.17 (0.26)
Na_2O	5.06 (1.70)	3.01 (2.12)	4.25 (1.65)	1.34 (1.23)	0.78 (1.45)	0.08 (0.03)
K_2O	0.68 (0.52)	0.23 (0.20)	0.53 (0.44)	0.10 (0.14)	0.07 (0.17)	0.02 (0.01)
Total	99.47 (0.64)	99.56 (0.87)	99.76 (1.20)	99.12 (1.09)	99.75 (1.01)	99.56 (1.06)
Cations based on 8 oxygens						
Si	2.449 (0.166)	2.252 (0.188)	2.416 (0.168)	2.108 (0.113)	2.063 (0.138)	1.983 (0.009)
Al	1.515 (0.168)	1.724 (0.191)	1.546 (0.178)	1.869 (0.118)	1.912 (0.146)	2.009 (0.009)
Fe	0.028 (0.013)	0.022 (0.006)	0.036 (0.013)	0.025 (0.009)	0.013 (0.013)	0.009 (0.001)
Mg	0.004 (0.005)	0.001 (0.001)	0.001 (0.002)	0.000 (0.001)	0.001 (0.001)	0.000 (0.000)
Ca	0.546 (0.165)	0.744 (0.189)	0.601 (0.154)	0.891 (0.114)	0.951 (0.135)	1.008 (0.006)
Na	0.448 (0.147)	0.267 (0.188)	0.375 (0.143)	0.120 (0.109)	0.069 (0.126)	0.007 (0.003)
K	0.039 (0.030)	0.013 (0.012)	0.030 (0.025)	0.006 (0.008)	0.004 (0.010)	0.001 (0.000)
$\sum$Cations	5.032 (0.009)	5.025 (0.011)	5.011 (0.020)	5.020 (0.007)	5.017 (0.018)	5.017 (0.006)
An	52.9 (16.2)	72.8 (19.1)	59.8 (15.5)	87.6 (11.1)	92.9 (13.1)	99.2 (0.3)
Ab	43.3 (14.0)	25.9 (18.1)	37.2 (14.1)	11.8 (10.7)	6.7 (12.2)	0.7 (0.3)
Or	3.8 (2.9)	1.3 (1.1)	3.1 (2.7)	0.6 (0.8)	0.4 (0.9)	0.1 (0.0)

All analyses normalized to 8 oxygens. Lava analyses are where the xenolith section had a small rind of lava still attached. Analyses are reported as the mean with one standard deviation in brackets. Plagioclase components: An, anorthite; Ab, albite; Or, orthoclase. n is the number of analyses.

ternary diagrams, although this is uncommon and observed only in sample CS16. These Al-rich clinopyroxenes are strongly zoned, from this Al-rich core to weakly oscillatory Di–Hd zoned mantle and rim zones (Fig. 7e). Commonly, however, magmatic skarn xenolith clinopyroxene zonation is restricted to the Di–Hd join (Fig. 7c), with patchy, highly irregular resorption surfaces (Fig. 7f). Titanium is correlated well with Al^{IV} across the magmatic skarn xenolith zones, excluding zone 3b, where CaTs-rich clinopyroxenes form with low Ti, comparable to the compositionally distinct exoskarn xenolith clinopyroxene (Fig. 7b).

Exoskarn clinopyroxenes are highly Al-enriched (Fig. 7a, b, d; Table 3), containing up to 22.3 wt % Al_2O_3, approaching the highest natural terrestrial values known to the authors (24.0 wt % in gehlenite-rich skarns from the Carpathians, Romania; Pascal *et al.*, 2005). $Fe^{3+}/\sum Fe$ (calculated following Droop, 1987) approaches unity (Fig. 7a). Clinopyroxene compositions at the exoskarn xenolith rim overlap magmatic compositions, but then immediately jump to highly Al-rich compositions, usually lacking the gradual progression observed in the magmatic skarn xenoliths (Fig. 7a–c).

Pyroxenoids

Wollastonite, present in all xenoliths, ranges from essentially pure $CaSiO_3$ to 5 mol % $FeSiO_3$, with $<$ 1.5 mol % $MnSiO_3$ (Fig. 8a; Table 3). Wollastonite compositions from 17 to 21 mol % $FeSiO_3$ are attributed to the ferrobustamite member of the wollastonite group rather than to iron-rich wollastonite, as bustamite is the stable crystal structure above $\sim$12 mol % $FeSiO_3$ (Rutstein, 1971; Rutstein & White, 1971). The ferrobustamite crystals are found as overgrowth crystals on wollastonite in the glass-bearing magmatic skarn xenoliths, in rare inclusions in wollastonite in magmatic skarn xenoliths, and in accessory phases in the calcite reaction rims in large calcite-bearing exoskarn xenoliths.

Garnet

Garnet is found predominantly in the exoskarn xenoliths as a main rock-forming mineral, with magmatic skarn xenolith garnet restricted to small interstitial patches in the cores or in zone R3b (Figs. 1, 2b). Garnet compositions across all xenolith types closely follow the grossular ($Ca_3Al_2Si_3O_{12}$)–andradite ($Ca_3Fe_2^{3+}Si_3O_{12}$) join, with only schorlomite ($Ca_3Ti_2SiFe_2^{3+}O_{12}$) being a notable additional component (Fig. 8b; Table 4), increasing with andradite content (Sch_{0-76}). Pyrope ($Mg_3Al_2Si_3O_{12}$) and almandine ($Fe_3Al_2Si_3O_{12}$) end-members combined are $<$ 6 mol %.

Magmatic skarn xenolith garnets exhibit a wide compositional range ($Grs_{0-66}Adr_{24-75}Sch_{0-76}$). In zone R3b, these garnets are compositionally distinct ($Grs_{60-66}Adr_{31-37}Sch_{1-2}$) from interstitial garnets within the wollastonite core ($Grs_{0-66}Adr_{24-75}Sch_{1-76}$). The interstitial garnets, in close spatial association with calcite, cuspidine, gehlenite and a wadalite-like phase (see below), have inclusions of this wadalite-like phase, possibly as a result of similarities between the crystal structure between hydrogarnet and wadalite-mayenite (e.g. Glasser, 1995; Grew *et al.*, 2013). Garnets with 76 mol % schorlomite [$Ca_{3.0}(Ti_{1.5}Fe_{0.1}^{2+}Fe_{0.2}^{3+}Mg_{0.1})(Si_{1.8}Al_{0.6}Fe_{0.6}^{3+})O_{12}$] are found as rims around titanite, in

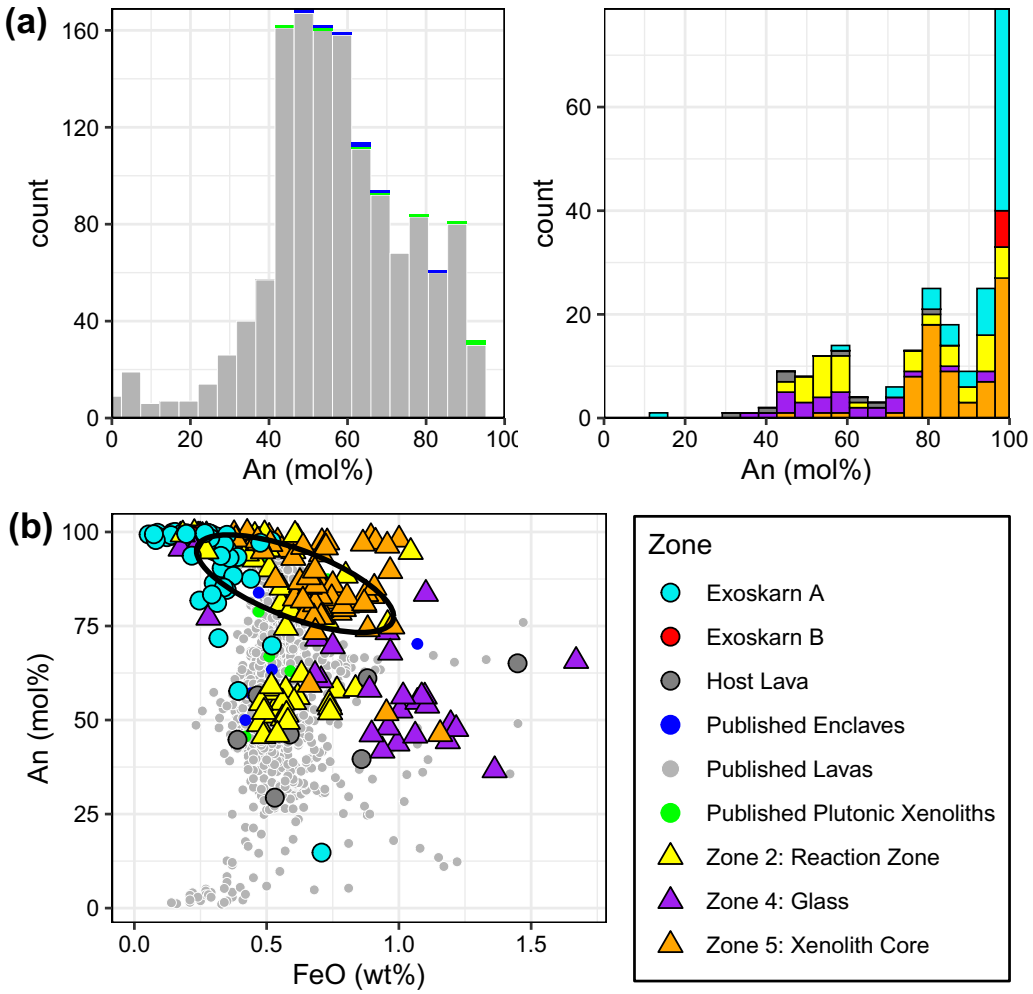

Fig. 6. Merapi xenolith and magmatic feldspar compositions. (a) Anorthite content histograms showing (left) published data from Merapi lavas (grey), enclaves (dark blue) and plutonic xenoliths (green) for comparison with xenolith and host lava feldspar data (right, key below). (b) An vs FeO plot showing the different xenolith plagioclase compositions compared with Merapi lava plagioclase. Ellipse of xenolith and xenocryst plagioclase compositions from Chadwick *et al.* (2007). Notably, plagioclase from zones R1 and R2 overlaps with the lava compositions, although they are formed from magma–carbonate interaction. Published lava feldspar data from Gertisser (2001), Preece (2014) and Erdmann *et al.* (2016). Enclave and plutonic xenolith data from Chadwick *et al.* (2013).

close association with perovskite. Ti gradients are found across rare wadalite-like phase-bearing garnet crystals ($Sch_{3\text{-}21}$).

Exoskarn xenolith garnets have a more restricted compositional range (Table 4), limited to higher grossular contents ($Grs_{73\text{-}97}Adr_{3\text{-}24}Sch_{0\text{-}2}$). The highest grossular contents, up to Grs_{97}, are found exclusively within exoskarn type-A xenoliths, around residual calcite crystals and their spurrite ± larnite-rich reaction rims.

Melilite

Melilite is found only in non-trace quantities in exoskarn assemblage-B xenoliths. Melilite compositions are gehlenite-rich, closely following the gehlenite–åkermanite join, with < 8 mol % Na-melilite and < 10 mol % Fe-åkermanite ($Gh_{43\text{-}91}Ak_{2\text{-}45}Na\text{-}Mel_{0\text{-}8}$) (Fig. 8c; Table 5). In exoskarn type-B xenoliths, melilite has three textural forms: surrounding spinel, intergrown with CaTs-clinopyroxene, and locally texturally equilibrated with 120° grain boundaries (Fig. 4c). Melilite in association with spinel is richer in gehlenite ($Gh_{68\text{-}83}$) than the clinopyroxene intergrowths ($Gh_{57\text{-}58}$) and well-equilibrated types ($Gh_{47\text{-}50}$).

Sulphur and halogen-bearing phases

Pyrrhotite is found in both magmatic and exoskarn xenoliths, often touching or rimmed by anhydrite. In magmatic skarn xenoliths, pyrrhotite is found in zone R2, as accessory inclusions in wollastonite and CaTs-clinopyroxene, and as rare inclusions in melt inclusions in the core. Fe/S ranges from 83 to 85%, and Cu concentrations range from 0.06 to 0.59 wt %. Pyrrhotite is sometimes found with near-stoichiometric cubanite (Table 6). The associated anhydrite is pure, with < 0.04 wt % BaO and < 0.1 wt % SrO.

Table 3: Average clinopyroxene (cpx), wollastonite (wo) and ferrobustamite (bst) compositions for each zone in the magmatic skarn xenoliths, exoskarns, and across all samples for wollastonite and ferrobustamite, as there is very little compositional variability for the pyroxenoids.

Type	Magmatic skarn							Exoskarn		All	All
Zone	Host lava	R1	R2	R3	R3b	R4	Core	Exoskarn A	Exoskarn B		
Mineral	Cpx	Cpx	Cpx	Cpx	Cpx	Cpx	Cpx	Cpx	Cpx	Wo	Bst
n	7	19	43	44	18	71	112	40	18	94	16
SiO_2	51.13 (0.72)	50.11 (1.54)	50.37 (0.94)	49.89 (1.41)	40.89 (0.46)	49.83 (1.70)	46.26 (1.94)	43.24 (2.67)	40.52 (1.87)	50.70 (0.69)	49.81 (0.52)
TiO_2	0.5 (0.11)	0.49 (0.10)	0.45 (0.16)	0.42 (0.10)	0.57 (0.10)	0.37 (0.23)	0.67 (0.27)	0.53 (0.36)	0.36 (0.27)	0.04 (0.05)	0.06 (0.04)
Al_2O_3	2.63 (0.43)	2.71 (1.56)	2.09 (0.64)	2.37 (0.59)	14.64 (0.40)	2.08 (0.96)	5.76 (2.89)	13.93 (5.95)	18.19 (1.97)	0.07 (0.08)	0.02 (0.02)
Cr_2O_3	0.00 (0.01)	0.02 (0.02)	0.02 (0.02)	0.02 (0.02)	0.01 (0.01)	0.01 (0.02)	0.02 (0.02)	0.01 (0.01)	0.02 (0.02)	0.01 (0.01)	0.01 (0.01)
FeO	8.85 (0.12)	12.38 (5.99)	10.62 (1.85)	12.58 (2.84)	8.58 (0.47)	13.46 (4.14)	11.26 (3.03)	7.96 (6.72)	5.65 (1.15)	1.31 (0.80)	10.81 (0.97)
MnO	0.56 (0.11)	0.57 (0.19)	0.55 (0.11)	0.48 (0.10)	0.32 (0.02)	0.50 (0.16)	0.21 (0.10)	0.24 (0.32)	0.08 (0.03)	0.37 (0.16)	1.13 (0.19)
MgO	14.43 (0.43)	11.38 (4.68)	11.74 (1.77)	10.82 (2.83)	9.07 (0.52)	9.45 (2.73)	9.66 (1.41)	8.59 (2.25)	9.57 (1.12)	0.22 (0.08)	0.70 (0.22)
CaO	21.20 (0.66)	22.06 (1.27)	22.62 (0.68)	22.72 (1.12)	25.18 (0.17)	23.90 (0.77)	23.76 (0.70)	25.04 (0.84)	25.88 (0.47)	47.09 (0.92)	38.08 (1.48)
Na_2O	0.43 (0.04)	0.34 (0.12)	0.41 (0.08)	0.38 (0.07)	0.02 (0.02)	0.29 (0.14)	0.33 (0.15)	0.07 (0.07)	0.04 (0.02)	0.02 (0.02)	0.04 (0.03)
Total	99.75 (0.50)	100.08 (0.81)	98.87 (0.71)	99.67 (0.82)	99.28 (0.64)	99.93 (0.60)	97.92 (0.70)	99.62 (1.24)	100.31 (0.81)	99.93 (0.88)	100.80 (1.40)
Cations based on 6 oxygens, 4 cations											
Si	1.901 (0.021)	1.895 (0.059)	1.918 (0.028)	1.898 (0.024)	1.535 (0.013)	1.906 (0.040)	1.786 (0.086)	1.624 (0.136)	1.485 (0.065)	1.967 (0.025)	1.956 (0.038)
Ti	0.014 (0.003)	0.014 (0.003)	0.013 (0.005)	0.012 (0.003)	0.016 (0.003)	0.011 (0.006)	0.019 (0.008)	0.015 (0.011)	0.010 (0.008)	0.001 (0.001)	0.002 (0.001)
Al^{IV}	0.099 (0.021)	0.105 (0.059)	0.082 (0.028)	0.102 (0.024)	0.465 (0.013)	0.094 (0.040)	0.214 (0.086)	0.376 (0.136)	0.515 (0.065)	0.033 (0.025)	0.044 (0.038)
Al^{VI}	0.018 (0.013)	0.018 (0.021)	0.013 (0.009)	0.006 (0.008)	0.183 (0.013)	0.007 (0.018)	0.047 (0.047)	0.238 (0.117)	0.271 (0.036)	0.000 (0.000)	0.000 (0.000)
Cr	0.000 (0.000)	0.000 (0.001)	0.001 (0.001)	0.000 (0.001)	0.000 (0.000)	0.000 (0.001)	0.000 (0.001)	0.000 (0.000)	0.000 (0.001)	0.000 (0.000)	0.000 (0.000)
Fe^{2+}	0.190 (0.032)	0.309 (0.241)	0.264 (0.071)	0.300 (0.087)	0.019 (0.022)	0.339 (0.122)	0.212 (0.106)	0.138 (0.230)	0.000 (0.002)	0.010 (0.018)	0.269 (0.076)
Fe^{3+}	0.086 (0.033)	0.088 (0.060)	0.075 (0.031)	0.102 (0.024)	0.251 (0.014)	0.094 (0.041)	0.153 (0.038)	0.117 (0.051)	0.173 (0.037)	0.033 (0.023)	0.086 (0.075)
Mn	0.017 (0.004)	0.018 (0.007)	0.018 (0.004)	0.015 (0.003)	0.010 (0.001)	0.016 (0.005)	0.007 (0.003)	0.008 (0.011)	0.002 (0.001)	0.012 (0.005)	0.038 (0.006)
Mg	0.800 (0.021)	0.635 (0.255)	0.665 (0.092)	0.611 (0.148)	0.507 (0.027)	0.536 (0.143)	0.555 (0.072)	0.478 (0.118)	0.523 (0.058)	0.013 (0.005)	0.041 (0.013)
Ca	0.844 (0.028)	0.895 (0.064)	0.923 (0.037)	0.927 (0.060)	1.013 (0.006)	0.980 (0.022)	0.982 (0.014)	1.006 (0.016)	1.017 (0.008)	1.957 (0.033)	1.601 (0.043)
Na	0.031 (0.003)	0.024 (0.009)	0.030 (0.006)	0.028 (0.005)	0.002 (0.001)	0.022 (0.010)	0.025 (0.012)	0.005 (0.005)	0.003 (0.001)	0.002 (0.001)	0.003 (0.002)
#Mg	74.4 (0.6)	60.6 (22.7)	66.1 (7.3)	59.8 (11.3)	65.3 (2.5)	55.3 (14.2)	60.7 (9.9)	68.3 (21.5)	75 (5.8)	27.5 (14.1)	10.4 (3.0)
Wo	43.6 (1.2)	46 (3.3)	47.5 (1.9)	47.4 (3.0)	56.3 (0.6)	49.8 (0.8)	51.5 (1.7)	57.9 (3.9)	59.3 (1.3)	96.7 (1.5)	78.7 (1.5)
En	41.3 (1.1)	32.7 (13.1)	34.2 (4.7)	31.3 (7.6)	28.2 (1.4)	27.3 (7.1)	29.1 (4.1)	27.8 (7.8)	30.4 (2.9)	0.6 (0.2)	2.0 (0.6)
Fs	15.1 (0.3)	21.3 (10.8)	18.3 (3.2)	21.3 (4.8)	15.5 (0.9)	22.9 (7.1)	19.4 (5.3)	14.3 (11.4)	10.3 (2.3)	2.7 (1.4)	19.3 (1.5)

Fe^{3+} calculated using Droop (1987). Analyses are reported as the mean, with one standard deviation in brackets. Clinopyroxene components: Wo, wollastonite; En, enstatite; Fs, ferrosilite. All Fe assumed as Fe^{2+} for ternary component calculation. n is the number of analyses.

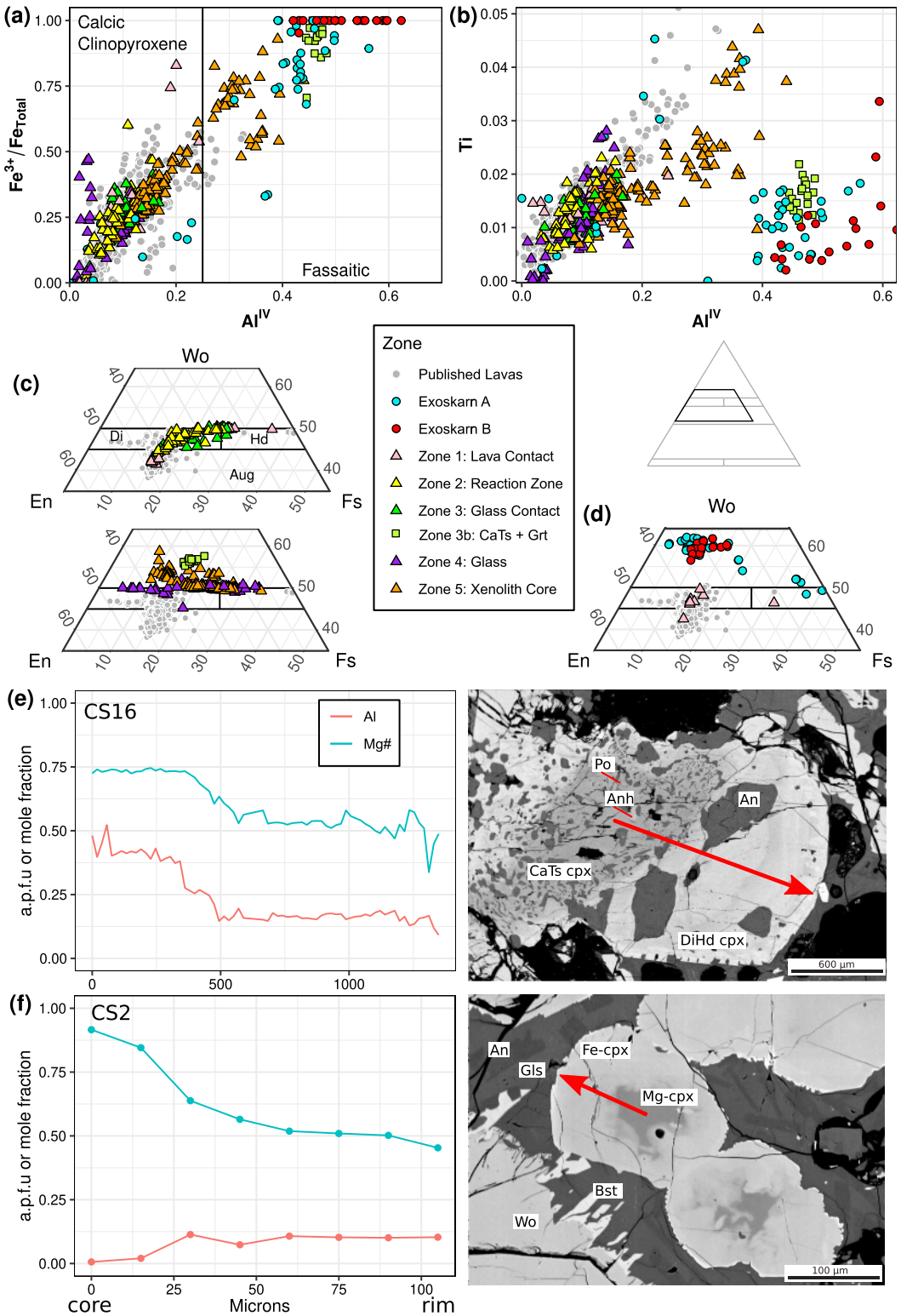

Fig. 7. Clinopyroxene compositions. (a) Fe^{3+}/Fe_{total} versus Al^{IV} plot showing a strong correlation (R^2=0.88). The fassaitic boundary ($Al^{IV} \geq 0.25$) is from Deer *et al.* (1997). (b) Ti versus Al^{IV} plot. Exoskarn clinopyroxene plot distinct from magmatic skarn clinopyroxenes. Zone 3b plots with the exoskarn data, showing a metamorphic character to this zone. (c) Ternary Wo-En-Fs components for magmatic skarn clinopyroxene. Two partial ternary diagrams are shown for clarity, with ternary location shown on the inset figure. Clinopyroxenes in zones 1 to 3 progressively become more Wo-rich, diverging from magmatic compositions. The remaining zones follow the Di–Hd join or plot above owing to the large amount of Al. (d) Partial ternary Wo-En-Fs components for exoskarn clinopyroxenes. (e) Al and Mg# traverse along a magmatic skarn clinopyroxene (sample CS16). Al- and Mg-rich cores progressively grade to low Al–high Fe compositions. (f) Al and Mg# traverse in magmatic skarn clinopyroxene from sample CS2. These crystals do not have an Al-rich core, and compositions instead follow the Di–Hd join. Published data sources as in Fig. 6 and additionally Deegan *et al.* (2016b).

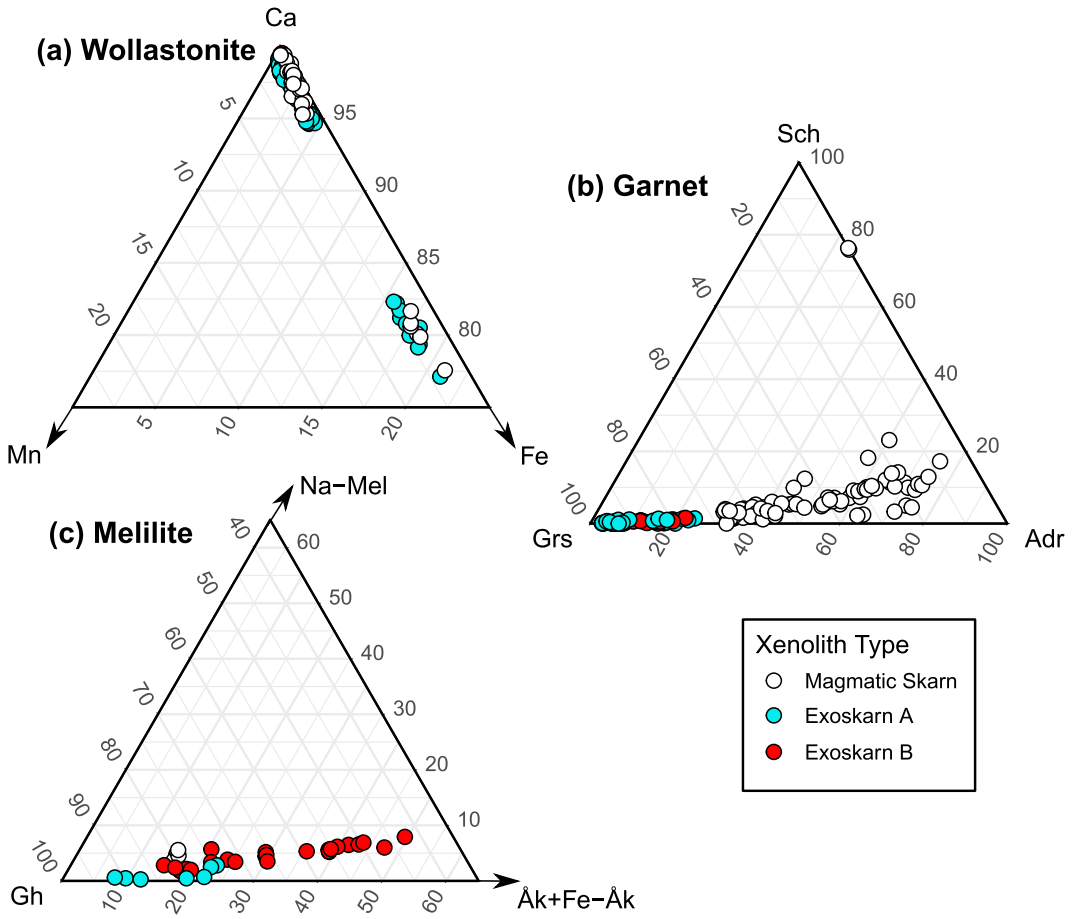

Fig. 8. Additional rock-forming mineral compositions. (a) Wollastonite and ferrobustamite. (b) Garnet. (c) Melilite. Note the different ternary scales for each plot. Arrows indicate truncated scales. Mineral abbreviations as in Table 1.

Cuspidine is found as crystals within calcite (magmatic skarn xenoliths) or forming within the reaction rim around calcite (exoskarn xenoliths) associated with stoichiometric spurrite ± larnite and an unidentified Ca-Si-Al-O phase. Fluorine atoms per formula unit (a.p.f.u.) approach the ideal 2 (1.937–2.035), indicating negligible OH. Fluorite is a fine-grained (< 20 μm) accessory phase replacing calcite in both xenolith types, and evidently nucleated at crystal borders or forming fine halos around vesicles in calcite.

Apatite is found in magmatic skarn xenolith zone R4, and contains 0.7 to 0.8 wt % Cl and no detectable SO_3. Ellestadite is found as an accessory phase in exoskarn xenoliths with 7.2 to 10.0 wt % SO_3 and 0.7 to 1.2 wt % Cl. F was not analysed with the EPMA; however, ∼2 wt % F was identified using SEM energy dispersive X-ray spectrometry (EDS), indicating that OH is minimal. Stoichiometric ellestadite (undetectable P_2O_5) with ∼1.9 wt % Cl was determined with SEM/EDS, coexisting with anhydrite in sample M13-02, within the reaction rim around large remnant calcite crystals.

Qualitative EDS analyses have identified trace quantities of small (< 5 μm) baryte crystals in both magmatic and exoskarn xenoliths, and additionally a crystal of cotunnite ($PbCl_2$) is present in the magmatic skarn xenoliths.

There are unidentified Cl-bearing minerals, which may possibly be new minerals. Skarn xenoliths, such as those from the Upper Chegem caldera, Russia, can host numerous new minerals (e.g. Galuskin *et al.*, 2013), and this may be the case at Merapi. A wadalite-like Ca-Al-Fe-Si-Cl mineral compositionally similar to the wadalite-eltyubyuite mayenite solid solution (when normalized to 26 cations) is found in association with calcite, cuspidine, garnet and gehlenite in magmatic skarn xenolith MX1 (Table 7). These crystals, however, have compositions with Si a.p.f.u. 4.6–5.5, higher than the ideal Si 4, and lack sufficient Mg to balance this increase in Si in wadalite (cf. Galuskin *et al.*, 2015). Raman spectra of this phase are included as the supplementary Fig. S4.

A Ca-Al-Si-Cl-F mineral is found in exoskarn xenoliths CS11 and M-XCS-b in the rim around areas where larnite and spurrite have replaced calcite. Concentrations of Cl and F in this mineral have been determined only by SEM-EDS, and as it contains 10 wt % more CaO than the wadalite-like mineral, and lower volatile contents (∼7 wt %) we believe it to be a different mineral.

Table 4: Average garnet compositions for the zones in the magmatic skarn xenoliths, and in the exoskarn xenoliths.

Xenolith type	Magmatic skarn				Exoskarn			
Zone	R3b		Core		Exoskarn A		Exoskarn B	
n	10		65		47		10	
SiO_2	38.27	(0.23)	35.01	(2.93)	39.27	(0.55)	38.94	(0.30)
TiO_2	0.76	(0.24)	3.45	(3.73)	0.23	(0.20)	0.29	(0.19)
Al_2O_3	14.24	(0.50)	9.64	(3.16)	20.37	(1.68)	18.88	(1.02)
Cr_2O_3			0.02	(0.03)	0.01	(0.02)	0.01	(0.02)
FeO	10.14	(0.49)	15.25	(3.60)	3.26	(1.88)	4.66	(1.11)
MnO	0.47	(0.05)	0.26	(0.09)	0.72	(0.68)	0.15	(0.03)
MgO	0.57	(0.04)	0.49	(0.19)	0.42	(0.17)	0.74	(0.10)
CaO	35.13	(0.26)	33.75	(0.78)	35.86	(0.78)	36.68	(0.54)
Total	99.59	(0.29)	97.86	(0.98)	100.23	(0.92)	100.35	(0.65)
Cations based on 12 oxygens, 8 cations								
Si	2.972	(0.013)	2.831	(0.196)	2.966	(0.026)	2.944	(0.032)
Ti	0.044	(0.014)	0.214	(0.243)	0.013	(0.012)	0.016	(0.011)
Al	1.304	(0.043)	0.913	(0.281)	1.813	(0.139)	1.681	(0.077)
Cr	0.000	(0.000)	0.001	(0.002)	0.000	(0.001)	0.001	(0.001)
Fe^{2+}	0.007	(0.017)	0.042	(0.042)	0.013	(0.024)	0.000	(0.000)
Fe^{3+}	0.652	(0.038)	0.995	(0.247)	0.194	(0.120)	0.295	(0.073)
Mn	0.031	(0.003)	0.018	(0.007)	0.046	(0.043)	0.010	(0.002)
Mg	0.066	(0.004)	0.059	(0.023)	0.047	(0.019)	0.083	(0.011)
Ca	2.923	(0.023)	2.926	(0.039)	2.902	(0.064)	2.970	(0.024)
Grs	64.3	(1.6)	37.5	(17.2)	87.7	(6.6)	83.9	(4.0)
Adr	33.5	(1.9)	52.0	(14.4)	9.6	(6.4)	15.1	(3.7)
Sch	1.4	(0.6)	9.3	(12.7)	0.4	(0.4)	0.7	(0.4)
Alm	0.0	(0.2)	0.2	(0.5)	0.4	(0.7)	0.0	(0.0)
Prp	0.7	(0.8)	0.8	(0.9)	0.7	(0.8)	0.3	(0.6)
Sp	0.1	(0.4)	0.1	(0.3)	1.2	(1.7)	0.0	(0.0)
Uv	0.0	(0.0)	0.0	(0.1)	0.0	(0.0)	0.0	(0.0)

Abbreviations as in Table 1. Additional garnet abbreviations: Prp, pyrope; Alm, almandine; Sp, spessartite; Uv, uvarovite. See Methods section for end-member calculation details. Fe^{3+} calculated using Arai (2010). Analyses are reported as the mean, with one standard deviation in brackets. n is the number of analyses.

Oxides, other silicates, and accessory minerals

The dominant Fe-Ti oxide in the magmatic skarn xenoliths is magnetite, with 0.3 to 11.5 wt % TiO_2. Magnetite within the xenolith cores is distinct ($<$ 0.3 wt % TiO_2) from magnetite in the other zones (8.9–11.5 wt % TiO_2). Ilmenite is present in zone R2 of one xenolith. Qualitative EDS analysis has identified micrometre-sized chromite in the xenolith cores. Hematite is the dominant oxide found in the exoskarn xenoliths, with rare magnetite present as well. Perovskite is found as a 50-μm vermicular cluster intergrown with wollastonite and plagioclase in one magmatic skarn xenolith (sample MX1) and is essentially stoichiometric $CaTiO_3$. A Ca-Zr-Ti-O mineral (calzirtite?) is found in the same magmatic skarn xenolith. Titanite across all xenolith types contains 1.04 to 2.51 wt % Al_2O_3 and 0.73 to 2.86 wt % FeO. An unidentified Ca-Al-Si-P mineral is found in exoskarn type-A samples CS11 and MXCS, approximating the formula $Si_{3.1}Ti_{0.1}Al_{2.9}Ca_{3.0}P_{0.9}O_{16}$ when assuming 16 oxygens. Xenotime and monazite are very rare calcite inclusions in exoskarn type-A xenoliths. Spinel ($Sp_{83\text{-}89}Her_{11\text{-}17}$) is found exclusively in the gehlenite-garnet-CaTs clinopyroxene-spinel exoskarn type-B xenolith (MX99-3s). These mineral analyses are given in Table 8.

Glass chemistry

Melt inclusions and interstitial glass are almost entirely restricted to magmatic skarn xenoliths, with melt inclusions and glass found only in the exoskarn xenoliths within the clinopyroxene-rich reaction rim at the host lava contact. Xenolith interstitial (zones R1, R2, R4 and core) and melt inclusion (zones R1, R3, R4 and core) glass compositions show a strong deviation from lava groundmass glass and melt-inclusion compositions, and also show compositional differences between zones (Fig. 9; Table 9). Melt inclusions are compositionally more diverse than the interstitial glass. CaO concentrations in interstitial glass and melt inclusions from zone R1 and some R2 analyses overlap lava glass CaO values (0.2 to 3.8 wt %). CaO concentrations in the interstitial glass (0.9–6.5 wt %) and in melt inclusions (0.5–11.3 wt %) within the xenolith zones R3, R4 and the core are elevated by up to ~4 wt % in the interstitial glasses in relation to magmatic values, and by up to 10 wt % in the melt inclusions. These glasses, especially the melt inclusions, are also characterized by low Al_2O_3 and K_2O relative to lava glasses (Fig. 9), and smaller variations from the lavas are observed in all other major and minor elements. Al_2O_3 concentrations are up to 5 wt % lower than in the lavas, and K_2O concentrations are up

Table 5: Average melilite compositions for the magmatic skarn xenolith core, and in the exoskarn xenoliths.

Xenolith type	Magmatic skarn		Exoskarn			
Zone	Core		Exoskarn A		Exoskarn B	
n	4		7		26	
SiO_2	24.72	(0.43)	25.29	(1.80)	29.06	(3.01)
TiO_2	0.01	(0.02)	0.01	(0.02)	0.01	(0.02)
Al_2O_3	29.87	(0.47)	28.92	(2.03)	25.09	(4.37)
Cr_2O_3	0.02	(0.01)	0.02	(0.01)	0.01	(0.01)
FeO	2.66	(0.07)	1.87	(0.97)	0.93	(0.18)
MnO	0.10	(0.02)	0.35	(0.24)	0.05	(0.03)
MgO	0.69	(0.03)	1.22	(1.05)	3.74	(1.43)
CaO	39.56	(0.16)	40.60	(0.43)	40.56	(0.95)
Na_2O	0.54	(0.10)	0.13	(0.12)	0.52	(0.21)
Total	98.17	(0.88)	98.55	(0.93)	99.99	(1.09)
Cations based on 7 oxygens						
Si	1.165	(0.013)	1.186	(0.074)	1.331	(0.136)
Ti	0.000	(0.001)	0.000	(0.001)	0.000	(0.001)
Al	1.659	(0.012)	1.600	(0.120)	1.354	(0.237)
Cr	0.001	(0.000)	0.001	(0.001)	0.000	(0.000)
Fe	0.105	(0.002)	0.074	(0.038)	0.036	(0.007)
Mn	0.004	(0.001)	0.014	(0.010)	0.002	(0.001)
Mg	0.048	(0.002)	0.085	(0.072)	0.255	(0.097)
Ca	1.998	(0.021)	2.042	(0.032)	1.990	(0.036)
Na	0.049	(0.009)	0.012	(0.011)	0.046	(0.018)
∑Cations	5.029	(0.013)	5.018	(0.012)	5.015	(0.017)
Gh	79.7	0.7	82.3	7.1	65.2	12.5
Ak	4.9	0.2	8.9	7.6	26.6	10.5
Fe-Ak	10.7	0.2	7.7	3.9	3.7	0.7
Na-Mel	4.7	0.8	1.1	1.1	4.5	1.8

All analyses are normalized to 7 oxygens. Abbreviations as in Table 1. See Methods section for details about the calculation of mole fractions of end-member compositions. Analyses are reported as the mean, with one standard deviation in brackets. n is the number of analyses.

to 2 wt % lower. Volatile concentrations of xenolith glasses are broadly comparable to those of the lava glasses, with only a few analyses showing concentrations exceeding those of the lavas. Sulphur exceeds lava groundmass concentrations in some zone R1 and zone R4 analyses, containing up to 510 ppm sulphur. Chlorine is typically within lava groundmass glass concentrations, and only exceeds lava glass values in plagioclase-hosted melt inclusions in sample CS16 and in interstitial glasses in MX99-4s. The few analyses for F ($<$ 1110 ppm) show that concentrations are within the wider range of lava values ($<$ 2637 ppm). Although the melt-inclusion analyses for MX1 show negligible F, localized patches of cuspidine and fluorite have been observed.

Fluid inclusions

Fluid inclusions in the magmatic skarn xenoliths (n=28) are two-phase, vapour-rich inclusions in wollastonite. The dominant fluid composition is CO_2, confirmed by instantaneous melting at –57.3°C to –56.1°C. The slight deviation from ideal melting at –56.6°C indicates the presence of a small percentage of other dissolved gases such as SO_2, N_2, which are not thought to have a significant effect on pressure estimates (Frezzotti *et al.*, 2002). No H_2O is observed either as ice or as clathrate.

Table 6: Cu-bearing mineral compositions.

	Po		Cub	
n	10		5	
Fe	58.44	(0.49)	38.70	(1.12)
S	39.83	(0.24)	35.08	(0.67)
Co	0.20	(0.02)	0.12	(0.03)
Ni	0.48	(0.11)	0.06	(0.05)
Cu	0.30	(0.17)	24.26	(1.51)
Zn	0.03	(0.02)	0.09	(0.05)
Total	99.28	(0.60)	98.30	(0.57)
Normalisation Sulphurs	1		3	
Fe	0.842	(0.007)	1.899	(0.036)
Co	0.003	(0.003)	0.005	(0.001)
Ni	0.007	(0.002)	0.003	(0.002)
Cu	0.004	(0.002)	1.048	(0.082)
Zn	0.005	(0.003)	0.004	(0.002)
Total	0.856	(0.007)	2.959	(0.072)
Fe/S	0.84	(0.01)		

Cubanite has only been found in magmatic skarn xenoliths, whilst pyrrhotite is found across all xenolith types, with little chemical variation between xenolith types. Analyses are reported as the mean, with one standard deviation in brackets. n is the number of analyses.

Homogenization is to the vapour phase at 12.9°C to 29.9°C. These temperatures correspond to densities of 0.15 to 0.35 g/cm^3, indicating trapping pressures of 33 to 92 MPa, when assuming a formation temperature of 850°C (see Discussion), utilizing the Hansteen & Klügel (2008) spreadsheet implementation of Sterner & Pitzer (1994) and the Span & Wagner (1996) density and equation of state models. An extreme temperature estimate increase to 1200°C only increases pressure estimates by ~30 MPa. No inclusions for barometry with resolvable homogenization were found in the exoskarn xenoliths, but CO_2 melting was observed in some inclusions.

DISCUSSION

In this section, we discuss the processes occurring during the formation of the xenoliths, and the pressure, temperature and fO_2 conditions that can be determined from the recorded mineral assemblages. We also discuss the implications for the magmatic system at Merapi, such as magmatic contamination by xenolith phases, metal transport, and the CO_2 output by decarbonation reactions. An accurate determination of temperature in the magmatic skarn xenoliths requires accurate estimates of the melt composition during xenolith formation; therefore, we first discuss the implications for any modification of melt-inclusion compositions.

Post-entrapment modification of melt inclusions

The abundance of melt inclusions in the magmatic skarn xenoliths allows the original composition of the melt present during xenolith formation to be constrained, and, potentially, the application of thermobarometric models (discussed below). Post-entrapment modification of melt inclusion compositions is a well-documented phenomenon, occurring via the diffusive

Table 7: Selected analyses of halogen- and sulphur-bearing minerals.

Sample	Multiple		Multiple		MX1		MX1		CS11		M-XCS-b	
Mineral	Cusp		El		Wad-1		Wad-2		Unk1		Unk2	
Type	Magmatic skarn		Magmatic skarn		Magmatic skarn		Magmatic skarn		Exoskarn A		Exoskarn B	
n	5		4		11		2		2		2	
SiO_2	32.70	(0.42)	8.37	(1.27)	17.63	(0.41)	24.98	(1.99)	26.70	(0.05)	23.33	(0.44)
TiO_2	0.19	(0.15)	0.02	(0.03)	0.38	(0.17)	0.56	(0.29)	0.00	(0.00)	0.01	(0.02)
Al_2O_3	0.02	(0.01)	0.03	(0.02)	23.85	(1.05)	19.59	(0.98)	14.47	(0.42)	12.98	(0.02)
Cr_2O_3	0.02	(0.02)	0.00	(0.00)	0.01	(0.02)	0.00	(0.01)	0.00	(0.00)	0.00	(0.00)
FeO	0.14	(0.08)	0.08	(0.03)	5.63	(1.21)	6.26	(2.60)	1.52	(0.37)	0.71	(0.15)
MnO	0.08	(0.02)	0.03	(0.01)	0.18	(0.05)	0.24	(0.15)	0.26	(0.10)	0.07	(0.06)
MgO	0.07	(0.07)	0.05	(0.02)	0.60	(0.08)	0.43	(0.09)	0.24	(0.01)	0.01	(0.01)
CaO	60.20	(0.24)	54.16	(1.19)	40.18	(0.43)	39.67	(3.09)	52.48	(0.13)	56.23	(0.26)
Na_2O	0.02	(0.02)	0.01	(0.02)	0.17	(0.16)	0.09	(0.04)	0.00	(0.00)	0.01	(0.02)
K_2O	0.01	(0.01)	0.00	(0.00)	0.00	(0.01)	0.02	(0.00)	0.00	(0.00)	0.01	(0.01)
P_2O_5	0.00	(0.00)	24.03	(3.25)	0.13	(0.13)	0.13	(0.18)			0.04	(0.02)
SO_3	0.00	(0.00)	8.12	(1.42)	0.01	(0.01)	0.00	(0.00)			0.02	(0.01)
Cl	0.01	(0.00)	1.04	(0.22)	12.91	(0.17)	8.87	(2.74)			2.12	(0.00)
F	10.26	(0.14)			0.02	(0.02)	0.00				4.90	(0.00)
Total	103.70	(0.40)	95.94	(0.81)	101.69	(0.56)	100.85	(2.08)	95.67	(0.12)	100.61	(0.10)
$O=(F_2,Cl_2)$	−4.32	(0.06)	−0.23	(0.05)	−2.92	(0.04)	−2.00	(0.62)	0.00	(0.00)	−2.54	(0.00)
Total	99.38	(0.44)	95.71	(0.78)	98.77	(0.53)	98.85	(1.46)	95.67	(0.12)	98.07	(0.10)
Normalisation cations	6		8		26		26		9		16	
Si	2.002	(0.009)	0.701	(0.106)	4.753	(0.092)	6.168	(0.277)	2.337	(0.006)	4.042	(0.058)
Ti	0.009	(0.007)	0.002	(0.002)	0.078	(0.034)	0.103	(0.051)	0.000	(0.000)	0.001	(0.002)
Al	0.001	(0.001)	0.003	(0.002)	7.578	(0.297)	5.713	(0.484)	1.493	(0.037)	2.649	(0.009)
Cr	0.001	(0.001)	0.000	(0.000)	0.003	(0.003)	0.001	(0.001)	0.000	(0.000)	0.000	(0.000)
Fe	0.007	(0.004)	0.006	(0.002)	1.270	(0.277)	1.285	(0.493)	0.112	(0.028)	0.103	(0.022)
Mn	0.004	(0.001)	0.002	(0.001)	0.042	(0.012)	0.050	(0.030)	0.019	(0.008)	0.011	(0.008)
Mg	0.007	(0.006)	0.007	(0.003)	0.240	(0.032)	0.159	(0.039)	0.031	(0.001)	0.002	(0.002)
Ca	3.949	(0.026)	4.858	(0.102)	11.610	(0.160)	10.524	(1.187)	4.923	(0.008)	10.436	(0.096)
Na	0.002	(0.002)	0.001	(0.003)	0.087	(0.083)	0.045	(0.022)	0.000	(0.000)	0.004	(0.005)
K	0.001	(0.001)	0.000	(0.000)	0.002	(0.003)	0.007	(0.000)	0.000	(0.000)	0.002	(0.002)
P	0.000	(0.000)	1.704	(0.230)	0.031	(0.029)	0.027	(0.038)	0.000	(0.000)	0.006	(0.003)
S	0.000	(0.000)	0.510	(0.089)	0.001	(0.003)	0.000	(0.000)	0.000	(0.000)	0.002	(0.001)
Cl	0.001	(0.000)	0.147	(0.031)	5.903	(0.087)	3.735	(1.277)	0.000	(0.000)	0.622	(0.003)
F	1.986	(0.044)	0.000	(0.000)	0.006	(0.011)	0.000	(0.000)	0.000	(0.000)	2.684	(0.012)

Wad-1, Wad-2 are the wadalite-like phase, found in sample MX1. Unk1 and Unk2 are unknown volatile-bearing minerals in samples CS11 and M-XCS-b, respectively. SEM-EDS analysis shows the presence of Cl and F in these latter two minerals. Normalization cations for the unknown volatile-bearing minerals are chosen to produce plausible formula units, and are not to represent any currently known minerals. Analyses are reported as the mean, with one standard deviation in brackets. n is the number of analyses.

Table 8: Average analyses of oxides and other silicate minerals found in the Merapi xenoliths.

Xenolith type	Magmatic skarn					Exoskarn A	Exoskarn B
Mineral	Mgt	Ilm	Hem	Psk	Ttn	CaSiAlP	Sp
n	27	1	4	3	8	1	8
SiO_2	0.14 (0.10)	5.92	0.31 (0.15)	1.13 (0.83)	30.91 (1.13)	33.30	0.01 (0.01)
TiO_2	9.91 (5.16)	43.22	0.15 (0.20)	54.75 (0.63)	36.28 (2.33)	1.19	0.01 (0.01)
Al_2O_3	2.66 (1.15)	1.10	0.59 (1.14)	0.43 (0.16)	1.70 (0.51)	26.28	66.59 (0.58)
Cr_2O_3	0.18 (0.20)	0.19	0.02 (0.02)	0.01 (0.01)	0.03 (0.03)	0.00	0.10 (0.07)
FeO	78.73 (4.81)	42.16	86.61 (2.79)	0.80 (0.15)	1.31 (0.70)	0.28	8.48 (1.41)
MnO	0.89 (0.30)	0.87	0.13 (0.14)	0.04 (0.03)	0.08 (0.07)	0.00	0.38 (0.08)
MgO	1.78 (0.55)	1.54	0.35 (0.58)	0.01 (0.01)	0.12 (0.29)	0.00	22.69 (0.77)
CaO	0.17 (0.21)	1.74	0.47 (0.19)	40.71 (0.47)	28.13 (1.04)	29.53	0.01 (0.00)
Na_2O	0.05 (0.05)	0.40	0.06 (0.04)	0.02 (0.02)	0.02 (0.01)	0.46	0.00 (0.00)
Total	94.51 (1.37)	97.37	88.70 (1.67)	97.92 (0.45)	98.66 (2.18)	102.40	98.27 (0.68)
Normalisation oxygens	4	3	3	3	5	16	4
Si	0.005 (0.004)	0.146	0.006 (0.005)	0.026 (0.019)	1.010 (0.034)	3.098	0.000 (0.000)
Ti	0.280 (0.153)	0.802	0.001 (0.001)	0.944 (0.008)	0.892 (0.053)	0.084	0.000 (0.000)
Al	0.117 (0.048)	0.032	0.001 (0.001)	0.012 (0.004)	0.065 (0.019)	2.880	1.965 (0.012)
Cr	0.005 (0.006)	0.004	0.000 (0.000)	0.000 (0.000)	0.001 (0.001)	0.000	0.002 (0.001)
Fe^{2+}	1.145 (0.181)	0.774	0.000 (0.000)	0.000 (0.000)	0.002 (0.007)	0.000	0.145 (0.023)
Fe^{3+}	1.311 (0.288)	0.095	1.478 (0.985)	0.015 (0.003)	0.033 (0.022)	0.022	0.033 (0.013)
Mn	0.028 (0.009)	0.018	0.001 (0.001)	0.001 (0.000)	0.002 (0.002)	0.000	0.008 (0.002)
Mg	0.098 (0.029)	0.057	0.002 (0.002)	0.000 (0.000)	0.006 (0.014)	0.000	0.847 (0.024)
Ca	0.006 (0.008)	0.046	0.009 (0.007)	1.000 (0.014)	0.985 (0.033)	2.942	0.000 (0.000)
Na	0.003 (0.004)	0.019	0.003 (0.002)	0.001 (0.001)	0.001 (0.001)	0.082	0.000 (0.000)

Analyses are reported as the mean, with one standard deviation in brackets. n is the number of analyses.

exchange of elements, crystallization of a host mineral boundary layer, or from the crystallization of daughter crystals (e.g. Nakamura & Shimakita, 1998; Danyushevsky *et al.*, 2000; Nielsen, 2011). Therefore, assessment of these effects is required before interpreting the inclusion compositions. Melt inclusions are found within clinopyroxene, plagioclase and wollastonite hosts in the magmatic skarn xenoliths, and for all of them there is no universally accepted way to back-calculate the original composition. The interstitial glass within the xenoliths provides a first-order constraint on the original melt composition, showing that it is strongly elevated in CaO compared with lava glass compositions (Fig. 9). We have not attempted correction of our melt inclusions, and consider the wollastonite-hosted melt inclusions to be the best estimates of melt CaO concentrations for the following reasons.

Examples of correcting for inclusion modification in clinopyroxene hosts include adding the host clinopyroxene to the inclusion (e.g. Hartley et al., 2018) until Fe-Mg partitioning between the inclusion and clinopyroxene (KD^{cpx-MI}_{Fe-Mg}) approaches the widely accepted equilibrium value of 0.28 ± 0.08 (Putirka, 2008), and adding calculated equilibrium clinopyroxene back to the melt inclusion until the calculated clinopyroxene has the same Mg# as the host (e.g. Preece et al., 2014). A compilation of magma–carbonate (both limestone and dolomite) interaction experimental data shows that $KD^{cpx-melt}_{Fe-Mg}$ in carbonate-contaminated systems may strongly diverge from the magmatic-derived 0.28 ± 0.08 (Putirka, 2008) (Fig. 10a), suggesting that $KD^{cpx-melt}_{Fe-Mg}$ is redox-sensitive (see oxybarometry discussion below) and that an Fe-Mg partitioning equilibrium-based correction is not appropriate.

The difference between observed and predicted clinopyroxene diopside-hedenbergite (DiHd) components (ΔDiHd: Putirka, 1999, 2008; Mollo *et al.*, 2013; Neave & Putirka, 2017) is more accurate at predicting equilibrium (Fig. 10b), with 68% of magma–carbonate experimental equilibrium clinopyroxene-melt pairs predicted to fall within model error (±0.07; Mollo *et al.*, 2013). Applied to the Merapi xenoliths, clinopyroxene-hosted melt inclusions within zones R3 and R4 have irregular embayed forms, suggesting some sidewall crystal growth, and ΔDiHd values > 0.07, indicating some potential modification of trapped melt compositions. Melt-inclusion–clinopyroxene pairs from zones R1 and R2 have ΔDiHd values from 0 to 0.14, with an average of 0.05, indicating that some may represent unmodified melt values. These compositions overlap lava glass compositions, consistent with their proximity to the lava contact, indicating a magmatic character.

An example of plagioclase-hosted melt-inclusion correction is regressing the magmatic liquid line of descent in TiO_2–Al_2O_3 space, and adding plagioclase back until the inclusions lie on the liquid line of descent (Hartley *et al.*, 2018). This cannot be applied here, as our measured xenolith melt-inclusion compositions, evidenced by elevated CaO in xenolith interstitial glass compositions, are contaminated and are not closed-system magmatic values (see below), and therefore

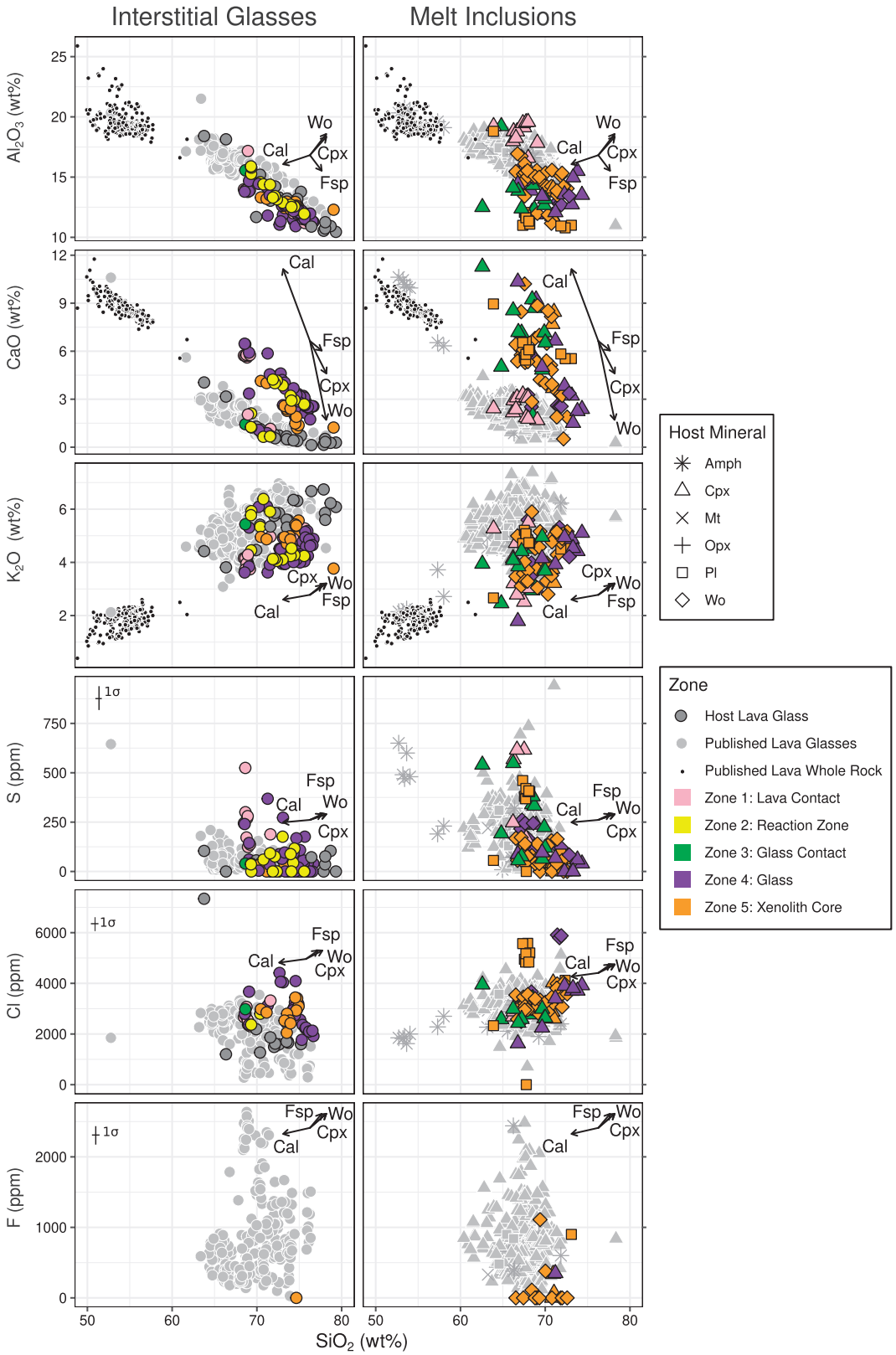

Fig. 9. Interstitial and melt inclusion glass compositions. All values are normalized to 100 wt % volatile-free. Host mineral refers to the crystal that the melt inclusion is found within. Published data for whole rock, glass and melt inclusions at Merapi are shown for comparison. Published data from Nadeau *et al.* (2013b), Borisova *et al.* (2013), Costa *et al.* (2013), Innocenti *et al.* (2013) and the GEOROC database (accessed 03/2019). Arrows show the effect of adding 10% calcite, and subtracting 10% clinopyroxene, wollastonite or plagioclase. Mineral abbreviations as in Table 1.

Table 9: Average interstitial glass and melt inclusion compositions for the zones in the magmatic skarn xenoliths.

Glass type	Interstitial glasses										Melt inclusions			
Zone	Host lava		R1		R2		R4		Core		R1		R4 and core	
n	15		11		15		48		12		12		70	
SiO_2	70.45	(3.36)	69.02	(2.54)	71.07	(2.76)	73.23	(2.21)	73.32	(1.78)	63.99	(3.03)	67.38	(3.72)
TiO_2	0.42	(0.11)	0.37	(0.10)	0.31	(0.14)	0.35	(0.13)	0.32	(0.09)	0.44	(0.05)	0.40	(0.19)
Al_2O_3	13.75	(1.83)	13.29	(0.95)	13.47	(1.17)	12.00	(0.88)	12.60	(0.38)	17.55	(0.82)	13.33	(1.97)
Cr_2O_3	0.01	(0.01)	0.01	(0.01)	0.01	(0.01)	0.01	(0.01)	0.01	(0.01)	0.02	(0.02)	0.01	(0.01)
FeO	2.59	(0.79)	3.03	(0.15)	2.52	(0.28)	2.22	(0.46)	2.22	(0.56)	2.55	(0.56)	2.84	(1.31)
MnO	0.12	(0.08)	0.13	(0.05)	0.10	(0.04)	0.07	(0.03)	0.05	(0.03)	0.13	(0.04)	0.09	(0.06)
MgO	0.40	(0.57)	0.12	(0.09)	0.12	(0.12)	0.06	(0.06)	0.07	(0.04)	0.33	(0.22)	0.35	(0.90)
CaO	1.05	(1.04)	4.71	(1.79)	2.49	(1.29)	3.04	(1.15)	2.26	(0.97)	2.44	(0.52)	5.87	(3.47)
Na_2O	3.89	(1.15)	3.41	(0.46)	3.59	(0.46)	3.22	(0.37)	3.32	(0.53)	4.01	(0.90)	3.43	(0.74)
K_2O	5.28	(0.72)	4.20	(0.52)	4.71	(0.80)	4.51	(0.56)	4.92	(0.50)	3.82	(1.03)	4.00	(0.99)
P_2O_5	0.12	(0.12)	0.08	(0.05)	0.07	(0.08)	0.09	(0.36)	0.04	(0.02)	0.23	(0.08)	0.08	(0.04)
SO_3	0.01	(0.01)	0.06	(0.03)	0.01	(0.01)	0.02	(0.02)	0.00	(0.01)	0.11	(0.05)	0.03	(0.03)
Cl	0.21	(0.16)	0.27	(0.03)	0.26	(0.03)	0.29	(0.07)	0.28	(0.04)	0.29	(0.02)	0.34	(0.11)
F (ppm)									0.00	(0.00)			184	(326)
Total	98.26	(1.38)	98.63	(0.83)	98.73	(1.56)	99.09	(0.92)	99.39	(1.12)	95.53	(3.48)	98.14	(1.97)

Analyses are reported as the mean, with one standard deviation in brackets. n is the number of analyses.

cannot be assumed to lie on a regression line through the magmatic liquid line of descent. Moreover, a micron-thick rim of Ab-rich plagioclase is observed around the inclusion walls (Fig. 3e, g) and suggests that some modification of plagioclase-inclusion compositions occurred as well.

Wollastonite-hosted melt inclusions are generally well formed and equant with a single shrinkage bubble, and lack textural evidence of sidewall crystallization and modification (Fig. 3d). Although Fe and Mn are weakly compatible in wollastonite, traverses from inclusion contact to 20 μm into the crystal do not show any resolvable chemical gradients that would indicate diffusion and melt-inclusion alteration. Therefore, wollastonite-hosted inclusions are probably the best inclusions to represent original compositions.

The effect of post-entrapment crystallization of a melt inclusion can be tested graphically. Fractionation vectors in Fig. 9 show the effect of 10% subtraction (crystallization) of clinopyroxene, plagioclase and wollastonite on glass compositions. Taking the fractionation vectors for the CaO vs SiO_2 plot, Fig. 9 shows that that any post-entrapment crystallization of the respective host phase would lower the CaO concentration of the trapped melt, and therefore our analyses must reflect minimum original CaO estimates, regardless of inclusion sidewall crystallization. Melt-inclusion compositions instead follow the vector for the addition of calcite to the published melt compositions. As the current methods of correcting for post-entrapment crystallization are not suitable for these compositions, no attempt has been made to account for the effects of melt-inclusion modification. In addition, these compositions overlap the compositions of Ca-contaminated interstitial glasses, and high CaO is present regardless of the host mineral phase. This shows that although post-entrapment modification may have occurred, the very high CaO values may reasonably represent minimum estimates of original melt compositions.

Intensive variables

Magmatic skarn xenolith thermobarometry

The abundance of glass and common mineral phases (clinopyroxene, plagioclase) allows for the application of thermobarometric models to the xenoliths (Fig. 11). On the basis of the uncertainty in mineral-melt equilibrium testing, and the results of testing thermobarometric models with experimental carbonate assimilation data (see Supplementary Data), the application of the glass-only equation (34) of Putirka (2008) to the clinopyroxene-saturated interstitial glasses of the magmatic skarn xenoliths with water contents estimated by difference from 100 wt % (Anderson, 1973, 1974; Devine *et al.*, 1995) provides a temperature of 829 ± 45°C (n =89). Melt inclusions, in turn, reflect a slightly higher temperature of 876 ± 49°C (n =88). These temperatures are consistent with the presence of ferrobustamite overgrowths on the coexisting wollastonite, which is thought to be stable between ~800°C and 880°C (Rutstein, 1971). A pressure of 50 MPa was assumed for thermometry, consistent with the results of fluid-inclusion barometry (our results: 34–92 MPa, and those of Clocchiatti *et al.* (1982): 67–109 MPa). Temperature estimates are lowered by a negligible 5°C per 100 MPa. Temperatures estimated for glasses within any lava attached to the xenolith, and lava interstitial glasses from the literature (with an assumed pressure of 200 MPa; cf. Preece *et al.*, 2014; Erdmann *et al.*, 2016) are higher than that of the xenolith glasses, at 937 ± 43°C. Phase equilibria estimates of pre-eruptive temperatures for Merapi are 925–950°C (Erdmann *et al.*, 2016), which

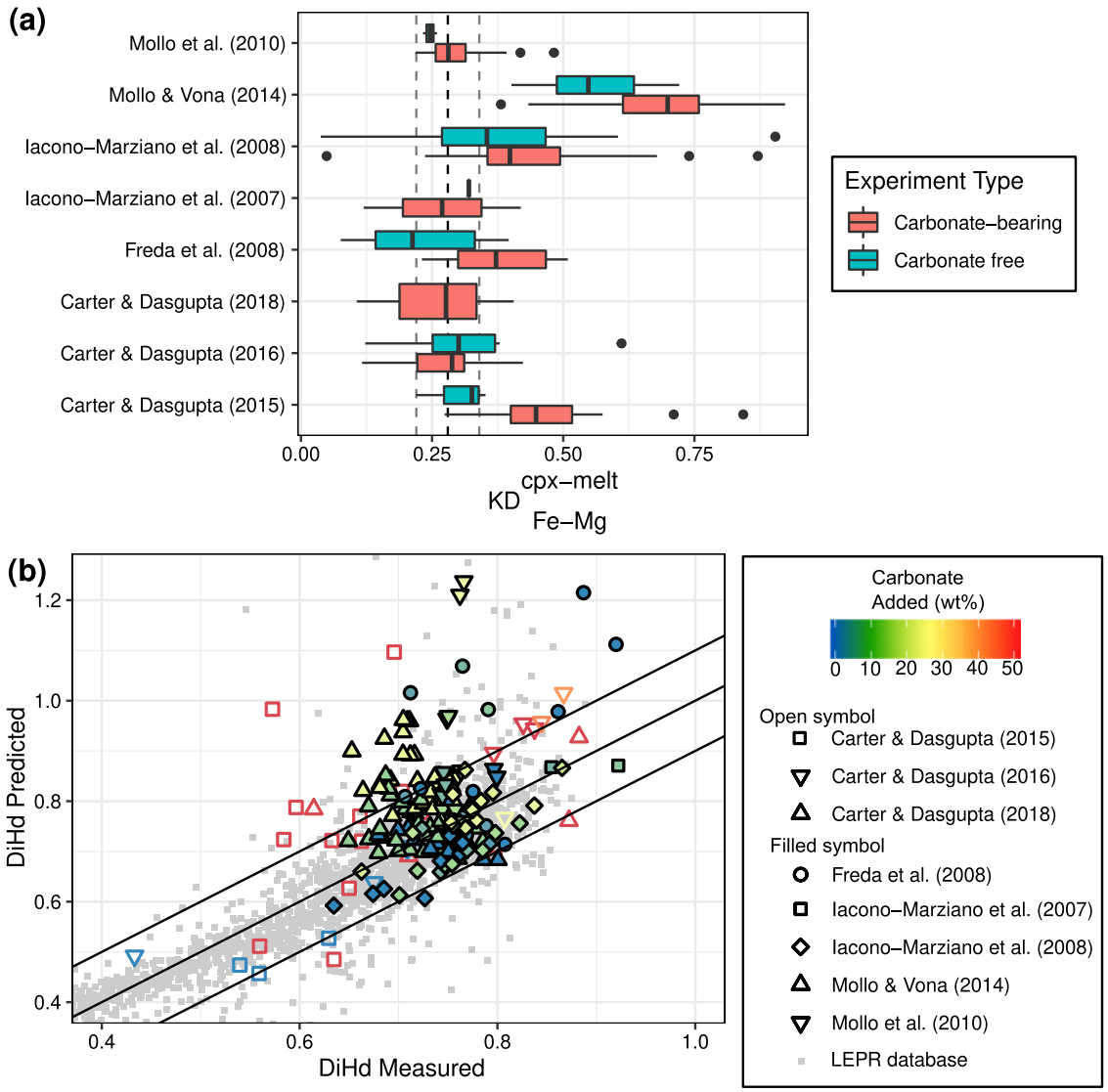

Fig. 10. (a) Box plots of $KD^{cpx-melt}_{Fe-Mg}$ values from carbonate assimilation experiments. Black circles represent outliers calculated as 1.5× interquartile range from the third quartile. Experiments with carbonate added have a general increase in $KD^{cpx-melt}_{Fe-Mg}$ values. Experiments by Carter & Dasgupta (2016) and Carter & Dasgupta (2018) use more evolved andesite and dacite compositions, compared with the remaining basaltic experiments, which were less affected by carbonate interaction. The extremely high values from Mollo & Vona (2014) are likely the result of very high experimental fO_2 conditions (up to air), which would strongly affect Fe^{2+}/Fe^{3+} partitioning between clinopyroxene and melt. (b) Comparison between measured clinopyroxene Diopside-Hedenbergite (DiHd) components and predicted ones, using the iterative approach of Neave & Putirka (2017). Light grey data are calculated from clinopyroxenes in the Library of Experimental Phase Relations (LEPR, Hirschmann *et al.*, 2008) database.

supports the higher lava glass temperature from our glass thermometry.

Additional constraints can be gained from comparison with experimental phase equilibria. The small interstitial patches of garnet, plagioclase and wollastonite in sample MX1 are stable between ~510°C and 890°C, with an $XCO_2 < 0.6$ at 100 to 200 MPa (Gordon & Greenwood, 1971; Tracy and Frost, 1991), consistent with temperatures from the glass thermometry. The R3b zone in sample MX1, comprising coexisting grossular-andradite garnet ($Adr_{0.3}$) and CaTs-clinopyroxene ($CaTs_{0.23}$) indicates temperatures of 900–950°C based on experimental phase equilibria (Huckenholz *et al.*, 1974; Gustafson, 1974).

Exoskarn T-XCO_2

Although the exoskarn xenoliths lack glass, many phases and assemblages in the exoskarn xenoliths can help constrain temperatures by comparison with experimental data and thermodynamic modelling. Spurrite + cuspidine ± larnite-bearing reaction rims between calcite and wollastonite + grossular + anorthite in samples CS11 and MXCS-0 allow temperature

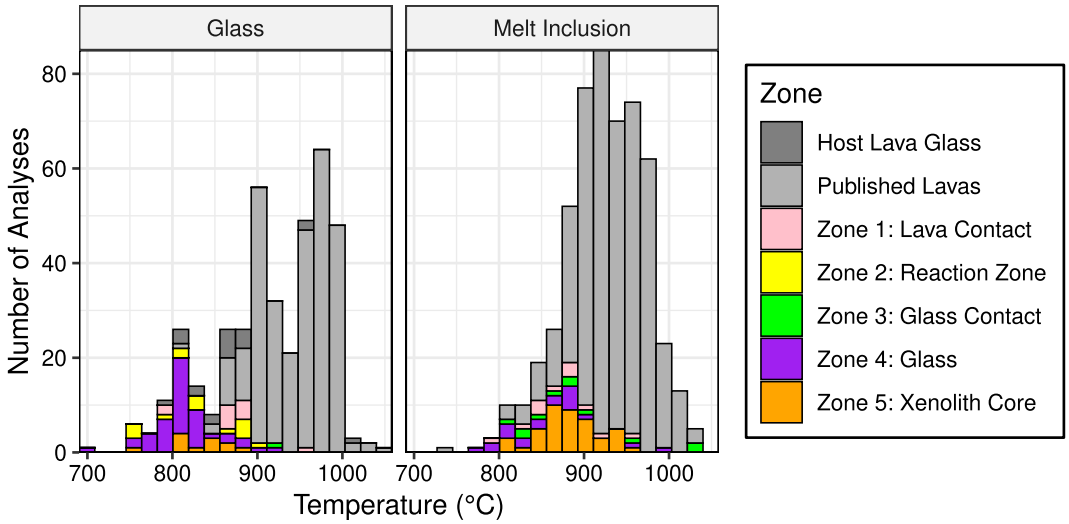

Fig. 11. Stacked histogram results of thermometry estimates for the magmatic skarn xenoliths and host lava glasses using equation (34) of Putirka (2008). Xenolith interstitial glasses produce temperatures of 829 ± 45°C (n=89). Melt inclusions have a slightly higher temperature of 876 ± 49°C (n=89). These temperatures are slightly below the thermometry estimates for published lava glass analyses, at 937 ± 43°C. Published glass data are from Preece *et al.* (2014) and Erdmann *et al.* (2016).

constraints, while additionally demonstrating the progressive interaction along a CaO-SiO_2-CO_2 system (e.g. Zharikov, 1969). The presence of spurrite and the absence of evidence for lower-temperature tilleyite-forming reactions indicate spurrite formation either by interaction between wollastonite and calcite,

$$3\overset{calcite}{CaCO_3} + 2\overset{wollastonite}{CaSiO_3} = \overset{spurrite}{Ca_5(SiO_4)_2CO_3} + 2CO_2$$

or by calcite directly with SiO_2

$$5\overset{calcite}{CaCO_3} + 2\overset{silica}{SiO_2} = \overset{spurrite}{Ca_5(SiO_4)_2CO_3} + 4CO_2$$

The former reaction indicates temperatures of ~700–1000°C (Tuttle & Harker, 1957). Spurrite is stable as low as 430°C at low CO_2 partial pressure (Henmi & Henmi, 1978), but the proximity of tens of microns to a decarbonating calcite crystal and a significant proportion of voids suggests a high CO_2 partial pressure. The latter reaction occurs at 910°C at 1 atm in the presence of chlorine or fluorine (Bolio-Arceo & Glasser, 1990). Cuspidine and fluorite are found within tens of microns of the spurrite, confirming that a reaction occurred with a fluorine-bearing fluid.

Larnite forms further from the calcite near the wollastonite contact (Deegan *et al.*, 2010; Fig. 10b) in sample MXCS-0, indicating temperatures of > 850°C (Wyllie and Haas Jr, 1965; Joesten, 1974; Treiman & Essene, 1983), following the potential reactions:

$$\overset{wollastonite}{CaSiO_3} + \overset{spurrite}{Ca_5(SiO_4)_2CO_3} = 3\overset{larnite}{Ca_2(SiO_4)} + CO_2$$

$$\overset{spurrite}{Ca_5(SiO_4)_2CO_3} = 2\overset{larnite}{Ca_2(SiO_4)} + CaO + CO_2$$

$$2\overset{calcite}{CaCO_3} + \overset{silica}{SiO_2} = 2\overset{larnite}{Ca_2(SiO_4)} + CO_2$$

The dominant mineral assemblage in these large calcite-bearing xenoliths can be described in the SiO_2-Al_2O_3-CaO system, comprising grossular garnet (Grs_{78-96}), wollastonite and anorthite. This assemblage is stable between ~510°C and 890°C at 50–200 MPa, with an increasingly restricted XCO_2 with pressure, varying from > ~0.2 to 1 at 50 MPa, and from ~0.2 to 0.4 at 200 MPa (Gordon & Greenwood, 1971; Tracy & Frost, 1991). Grossular with inclusions of calcite, wollastonite and anorthite is additionally found in the CaTs-clinopyroxene-bearing xenoliths, suggesting that the following reaction has occurred:

$$\overset{calcite}{CaCO_3} + \overset{wollastonite}{CaSiO_3} + \overset{anorthite}{CaAl_2Si_2O_8} = \overset{grossular}{Ca_3Al_2Si_3O_{12}} + CO_2$$

The equilibration temperature of CaTs-clinopyroxene and grossular-andradite-bearing exoskarn xenoliths is estimated as 900–950°C based on experimental data (Huckenholz *et al.*, 1974). Reactions involving these phases were further investigated using Theriak-Domino software (build date 3-1-2012, de Capitani & Petrakakis, 2010) using calculated whole-rock compositions in the system Si-Al-Fe-Mg-Ca-C. An upper limit of temperature for the exoskarn xenoliths is ~910°C at 100 MPa, which represents the limit of garnet stability (Fig. 12). Garnet reacts out just after melilite becomes stable at ~900°C. Exoskarn type-A xenoliths contain abundant garnet and trace amounts of gehlenite, constraining the temperature to the narrow field between 900 and 910°C. The calculated high (30 mol %) CaTs contents at the melilite-in boundary are in agreement with the high (up to 38 mol %) CaTs contents observed in these xenoliths, as are

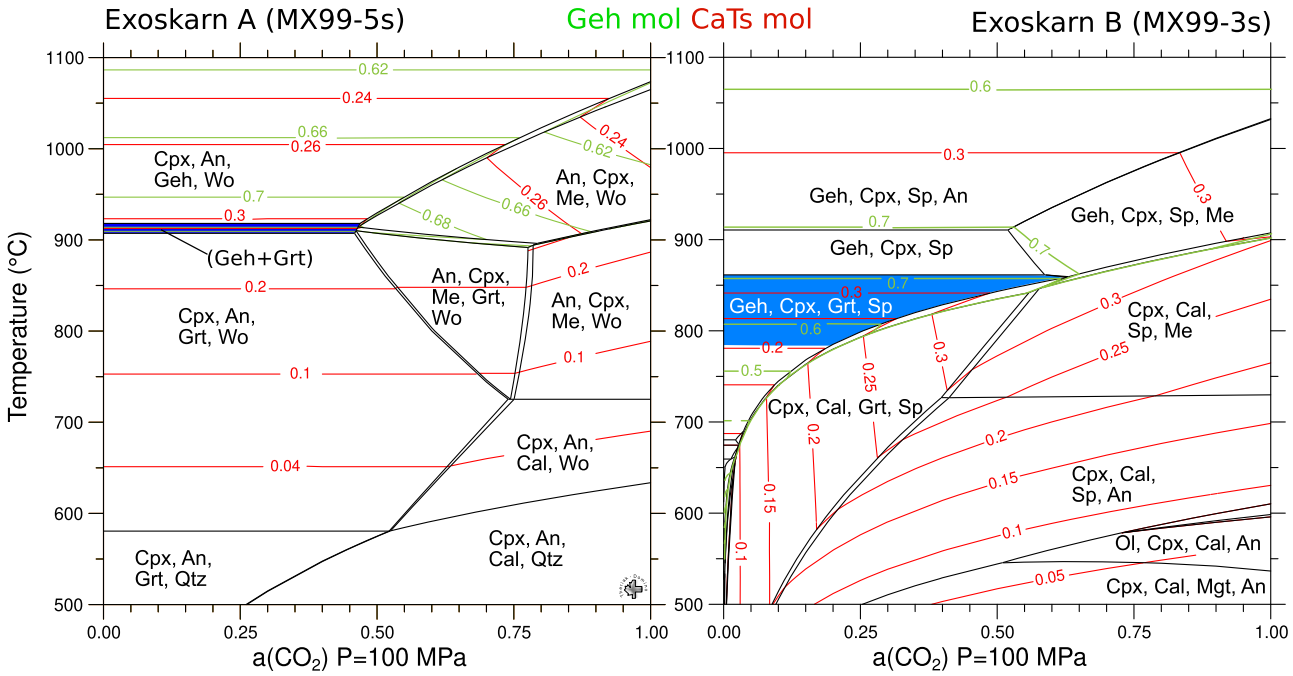

Fig. 12. Theriak-Domino (de Capitani & Petrakakis, 2010) T-XCO_2 modelling of exoskarn xenoliths. Isobaric sections at 100 MPa. Green contours show the gehlenite mole fraction. Red contours show the CaTs mole fractions. The exoskarn A xenolith (MX99-5s) formed in a narrow temperature range between ~900 and 910°C, and $XCO_2 < 0.5$. The exoskarn B xenolith (MX99-3s) mineral assemblage records temperatures between 680 and 860°C at a $XCO_2 <$ ~0.5. Abbreviations as in Table 1. Additional abbreviations: Grt, garnet (andradite-grossular); Me, meionite; Ol, olivine.

modelled gehlenite contents (> 70 mol %) compared to the observed ones (74–94 mol %). The mineral assemblage of the exoskarn type-B xenolith is constrained by a slightly lower maximum temperature, as garnet becomes unstable at 860°C (Fig. (12). A minimum temperature estimate is given as ~780°C from the high clinopyroxene CaTs component (22–39 mol %). Conditions are further constrained to $a_{CO2} < 0.5$ for both xenolith types by the absence of meionite and calcite. The results closely match the temperatures from previously cited experimental studies. These temperature estimates are similar to those estimated for the magmatic skarn xenoliths by thermobarometry.

In summary, the comparison with experimental studies and results from modelling indicate exoskarn formation temperatures up to ~910°C, with a lower limit at around 780°C for xenoliths with CaTs clinopyroxene and 510°C for xenoliths without CaTs clinopyroxene. There is no evidence for low-temperature retrograde overprint, and these temperatures overlap the temperatures estimates for the magmatic skarn xenoliths (~850°C). These temperature estimates extending to as low as 510°C, combined with the petrological differences described above, indicate a metasomatic origin for the exoskarn xenoliths instead of petrogenesis via magmatic crystallization for the magmatic skarn/endoskarn xenoliths.

Oxygen fugacity

Estimates of oxygen fugacity (fO_2) are difficult owing to the lack of mineral assemblages commonly used to determine this variable. A first-order estimate is obtained from the presence of magnetite in magmatic skarn xenoliths compared to hematite in the exoskarn xenoliths, indicating more oxidizing conditions in the latter. Two single crystal clinopyroxene oxybarometers exist that use Fe^{3+} concentrations in clinopyroxene to estimate oxygen fugacity (Cortés *et al.*, 2006; Simakin *et al.*, 2012). Although Fe^{3+} concentrations in clinopyroxenes calculated by stoichiometry (e.g. Lindsley, 1983; Droop, 1987) have been shown in some studies to have a weak correlation with measured clinopyroxene Fe^{3+} concentrations (e.g. Sobolev *et al.*, 1999), a positive correlation between clinopyroxene Fe^{3+}/Fe^{total} and fO_2 has been demonstrated from experimental data by Cortés *et al.* (2006) and Simakin *et al.* (2012). When taking a much larger dataset (the Library of Experimental Phase Relations, Hirschmann *et al.*, 2008), with high-fO_2 experiments such as those from Mollo & Vona (2014) and Sugawara (2001), and normalizing the data to the NNO (nickel–nickel oxide) buffer (cf. Cortés *et al.* 2006) using buffer equations from Frost (1991), a broad positive correlation is still observed, although with a large scatter (R^2=0.44). Fe^{3+}/Fe_{total} falls short of unity at an fO_2 of air, and all Fe is Fe^{2+} at ~ΔNNO-2. When applied to this large experimental dataset, the oxybarometer of Cortés *et al.* (2006) strongly overestimates fO_2 conditions, whilst Simakin *et al.* (2012) fail to recover experiments performed in air (Fig. 13).

We use a selection of data from experiments that span a wide fO_2 range to calibrate a new oxybarometer

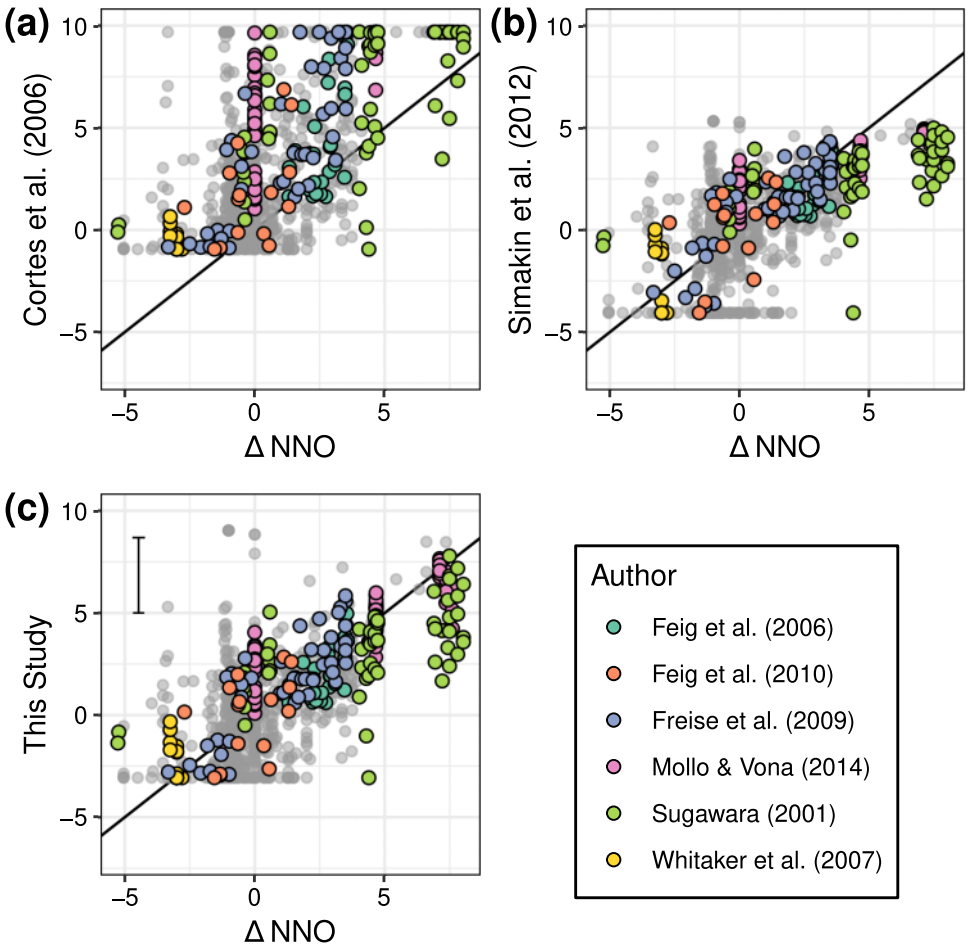

Fig. 13. Clinopyroxene-only single-crystal oxybarometer model testing. Experiments used for the calibration of the new oxybarometer are highlighted (Feig *et al.*, 2006, 2010; Berndt *et al.*, 2005; Whitaker *et al.*, 2007; Mollo & Vona, 2014). The experiments of Sugawara (2001), which cover 13 log units, and the results of applying the oxybarometers to the filtered Library of Experimental Phase Relations (LEPR Hirschmann *et al.*, 2008) are also shown. (a) Results of the Cortés *et al.* (2006) oxybarometer applied to the experimental clinopyroxenes. (b) Results of the Simakin *et al.* (2012) oxybarometer applied to the experimental clinopyroxenes. (c) Results of the model calibrated in this study applied to the experimental clinopyroxenes. The model error is shown in the top left.

that recovers high-fO_2 conditions more accurately. We use the datasets of Whitaker *et al.* (2007), Freise *et al.* (2009), Feig *et al.* (2006), Feig *et al.* (2010) and Mollo & Vona (2014) (excluding Mollo & Vona's relatively high Fe^{3+}/Fe_{total} NNO experiments). This calibration dataset spans a fO_2 between ΔNNO-5 and air, temperatures between 900°C and 1280°C, covers between 0 and 5 wt % H_2O, between 50 and 68 wt % SiO_2, and has a high coefficient of determination ($R^2 = 0.80$). Although the dataset of Sugawara (2001) spans the widest fO_2 range known to the authors (~13 log units), calculated Fe^3/Fe_{total} values have a larger scatter than those from other datasets, and therefore we exclude these from the regression. Furthermore, although Al^{IV} increases in clinopyroxene with increasing fO_2 (e.g. Mollo & Vona, 2014), adding Al^{IV} to the models gives no significant improvement on the model, and therefore we only use Fe^3/Fe_{total} for prediction. There is also no significant improvement in R^2 or the standard error when using a polynomial fit over a linear model; however, we use a polynomial fit to improve the estimates at low fO_2 marginally, as was shown by Simakin *et al.* (2012). In addition, we considered constructing a similar oxybarometer based on Fe^{3+} in garnet, as Fe^{3+} can be estimated accurately for this mineral (Arai, 2010); however, there is an insufficient range of oxygen fugacity controlled experiments in the Library of Experimental Phase Relations (LEPR; Hirschmann *et al.*, 2008) database to attempt to build a similar single-crystal oxybarometer for garnet.

For testing, we filtered the entire experimental database to clinopyroxenes equilibrated < 1 GPa, with Si a.p.f.u. < 2, Ca > 0.5 a.p.f.u., cation totals between 3.98 and 4.1, and Na_2O < 1 wt %. Our models recover the calibration dataset with a residual standard error of 1.5 log units, and the global database and additional experimental data to 1.8 log units, compared with 2.1 for Cortés *et al.* (2006) and Simakin *et al.* (2012). The

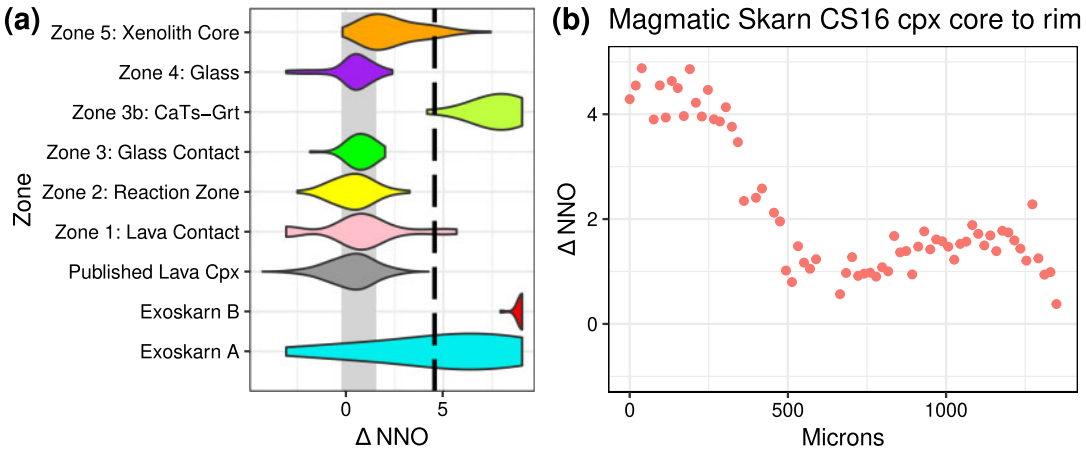

Fig. 14. fO_2 estimates from clinopyroxenes across all zones and traverses. (a) Violin density plots of oxygen fugacity estimates for xenolith clinopyroxenes. The model error has been applied as the smoothing bandwidth. The light grey field shows published estimates of Merapi magma fO_2 from other independent methods (ΔNNO −0.2 to 1.6; Gertisser, 2001; Erdmann *et al.*, 2014). Application of our model to the literature clinopyroxene dataset detailed in Fig. 7 is shown for comparison with past literature estimates. The solid dashed line is the magnetite–hematite oxygen fugacity buffer. The results show that xenolith rims (zones R1–R3) formed at fO_2 similar to magmatic conditions, whilst the cores and exoskarn xenoliths formed at much higher fO_2, up to that of air. (b) Results of application of the oxybarometer to the core-to-rim traverse of the same clinopyroxene from sample CS16 as shown in Fig. 7e. The results show an initial period of high fO_2 during initial clinopyroxene formation and vigorous carbonate–magma interaction, and then a progressive decline as the carbonate-contaminated melt precipitates mineral phases and CO_2 migrates from the reaction zone.

improvements in the error are small, in part due to a lack of high-fO_2 experiments and potentially variable data quality of the individual experiments in the LEPR database. However, the accuracy at high fO_2 is improved, which is the range of fO_2 most relevant to our Merapi xenoliths. We obtain the following equation:

$$\Delta NNO = 22.705\left(\frac{Fe^{3+}}{\sum Fe}\right)^3 - 32.400\left(\frac{Fe^{3+}}{\sum Fe}\right)^2 + 21.799\left(\frac{Fe^{3+}}{\sum Fe}\right) - 3.066$$

where Fe^{3+} and $\sum Fe$ are Fe a.p.f.u. estimated from stoichiometry (e.g. Lindsley, 1983; Droop, 1987), and ΔNNO is the deviation from the nickel–nickel oxide oxygen-fugacity buffer in log units.

Application of our oxybarometric model shows a wide spread of fO_2 values for the xenoliths (Fig. 14a). Magmatic skarn xenolith clinopyroxenes at the lava contact zone R1 and in zones R2, R3 and R4 have values similar to both the magmatic values predicted by our model and published estimates (ΔNNO −0.2 to +1.6, Gertisser, 2001; Erdmann *et al.*, 2014). Touching pyrrhotite and anhydrite crystals in zone R2 in a small subset of magmatic skarn xenolith samples additionally indicate a near-magmatic fO_2 range between ΔNNO +0.5 and +2.5 (Luhr, 2008; Parat *et al.*, 2011), consistent with other estimates. The R3b zone in sample MX1 records higher oxygen-fugacity conditions than the CaTs clinopyroxene + garnet-absent samples, at ΔNNO > +5. Xenolith core clinopyroxenes are formed through a large range of oxygen-fugacity conditions. The higher values come from the CaTs-rich clinopyroxene cores of sample CS16 (Fig. 14b). Anhydrite crystals within these clinopyroxene cores (stable at > ΔNNO+1 Carroll and Rutherford, 1987) provide further evidence for a relatively high fO_2 during early clinopyroxene formation. Exoskarn xenolith clinopyroxene indicates formation under higher fO_2 than magmatic skarn xenoliths, with values approaching that of air (∼ΔNNO + 8). While exoskarn type-A xenoliths record a large range, from ΔNNO −1 to +8, the exoskarn type-B xenolith uniquely records conditions of exclusively > ΔNNO + 5. The high fO_2 conditions recorded in the exoskarns are similar to that recorded in zone R3b of magmatic skarn xenolith MX1.

High fO_2 in skarn systems is a result of CO_2 release from carbonate, and this CO_2 can impose a fO_2 equal to or greater than the hematite-magnetite (HM) buffer (e.g. Nicholls, 1971; Wenzel *et al.*, 2002). The magnitude of fO_2 increase is proportional to the freedom CO_2 has to leave the system. An open system with a continuous flux of CO_2 increases fO_2 to higher values than are obtained in a closed system (Ganino *et al.*, 2008). The generally higher fO_2 observed in the exoskarn xenoliths may thus be a result of a prolonged open-system flux of CO_2, whereas the magmatic skarn xenoliths were rapidly processed within the magma. Magmatic skarn xenolith zone R3b, however, records a high fO_2, comparable to the exoskarns, and mineral phases in it, such as clinopyroxene, compositionally overlap exoskarn mineral compositions (Fig. 7). These compositions may be in part due to a lack of melt in this region of the magmatic skarn xenolith, restricting SiO_2 availability, and

producing as a result silica-undersaturated mineral compositions such as CaTs clinopyroxene.

Xenolith petrogenesis

Protolith

The absence of Mg-rich skarn minerals within the xenoliths (olivine, periclase, merwenite, åkermanite) and the abundance of wollastonite instead suggests a calcite-limestone protolith for the xenoliths. The Merapi xenoliths do not match any mineral assemblages produced during magma–dolomite interaction experiments; instead, they closely resemble the results of magma–limestone experiments (e.g. Zarayskiy *et al.*, 1987: wollastonite, clinopyroxene, garnet). Electron microprobe analyses of calcites (Whitley *et al.*, 2019) reveal pure calcites with < 0.2 wt % MgO + FeO + SrO, which additionally indicates a pure limestone protolith in the absence of Mg-rich skarn minerals. Furthermore, local carbonate sampled from Parangtritis (50 km south of Merapi) is limestone. The progressive chemical zonation within the xenoliths from 'magmatic' to calcic compositions (Fig. 5) shows that the Mg-Fe-Al-bearing phases source these elements from the host magma, not from a dolomite or marl.

Magmatic skarn xenoliths

The abundance of Ca-rich melt inclusions and Ca-rich groundmass glass (Fig. 3) indicate crystallization of the main skarn mineralogy of clinopyroxene, plagioclase and wollastonite from a Ca-contaminated magmatic melt, produced from the dissolution of the carbonate protolith (Fig. 9) (cf. Deegan *et al.*, 2010). Calcic melt inclusions and matrix glasses were also described from volcanic products of the 2010 eruption of Merapi (Borisova *et al.*, 2013). Thermodynamic modelling suggests the formation of Ca-rich melts via a peritectic reaction of grossular-bearing calc-silicate material with the magma (Borisova *et al.*, 2016). The Ca-rich melt inclusions are spread randomly throughout their host crystals, or, less commonly, along crystal growth zones, showing a primary origin (Roedder, 1984; Goldstein, 2003). Clinopyroxene compositions in these xenoliths are compositionally distinct from those in the exoskarn xenoliths, most notably those from the glass zone R4 (Fig. 7), supporting formation from the Ca-rich melt instead of an origin as incorporated xenocrysts from partially melted exoskarns. The Fe-rich ferro-bustamite growths on some wollastonite crystals are also consistent with crystallization from this melt, as the glass and core zones are characterized by FeO-enrichment (Figs. 6, 7). Melt inclusions in wollastonite do not comprise exclusively CaO and SiO_2, but also contain other major-element oxides such as K_2O, which can only be derived from the magmatic melt, as no K-bearing phases are found in any of the xenoliths studied. The composition of these melt inclusions cannot be explained by the dissolution of wollastonite, but supports the idea that wollastonite crystallized from a Ca-enriched melt. Experimental work at Merapi has shown that the contaminated melt takes up Sr and B from the carbonate protolith (Deegan *et al.*, 2010, 2016a), which supports the idea of dynamic element exchange between carbonates and the surrounding melt. The arrows in Fig. 9 show the addition of 10% CaO to the melt, indicating that the melt inclusions record crystallization from a melt with up to 20% CaO added. The groundmass glasses retain evidence for up to 10% added CaO, after crystallization of wollastonite and other minerals. Although whole-rock compositions at Merapi are basaltic to basaltic-andesite, the lava groundmass glasses, the melt compositions in contact with the carbonate, and xenolith glasses, are distinctly more felsic (60–76 wt % SiO_2). The melt-inclusion CaO concentrations observed in our study (Fig. 9) far exceed (up to 11.3 wt % CaO) those observed in glasses from the calcite-saturated dacite-carbonate experiments of Carter & Dasgupta (2016) (< 4.3 wt %), confirming their hypothesis that natural systems may be able to assimilate more carbonate than their closed-system experiments indicated.

Skarn minerals that contain melt inclusions and show evidence for crystallization from a carbonate-contaminated magmatic melt, instead of through metasomatic transfer, are a rare but increasingly recognized phenomenon (e.g. Fulignati *et al.*, 2001; Bin & Jin-song, 2016). Homogenization temperatures of these melt inclusions in the literature (Fulignati *et al.*, 2001; Bin & Jin-song, 2016) indicate temperatures of 860–1200°C, which are in excess of those typically experienced during metasomatic skarn formation in contact metamorphic aureoles ($<$ *c.* 800°C; Meinert, 1992), indicating direct interaction between a magmatic melt and carbonate. The trapping of melt inclusions in skarn minerals precipitated from a calcite-contaminated quartz diorite melt has been experimentally confirmed (Bin & Jin-song, 2016), and dacite–carbonate interaction experiments (Carter & Dasgupta, 2016) have been shown to crystallize wollastonite, in contrast to the production of dominantly Ca-rich melt in experiments with mafic melt compositions (Deegan *et al.*, 2010; Carter & Dasgupta, 2015).

As well as this rare and unique evidence for skarn mineral formation from carbonate-contaminated melts, and therefore exoskarn formation by this process, the magmatic skarn xenoliths also provide insights into the morphology and cumulate-forming processes at the wall-rock contact at Merapi. Carbonate assimilation has been shown to form and/or influence the mineralogy of cumulate assemblages: for example, changes to the mineral chemistry of dunites at the Ioko-Dovyren Intrusion, Russia (Wenzel *et al.*, 2002); the formation of clinopyroxenite xenoliths at Nisyros, Greece (Spandler *et al.*, 2012); and olivine+clinopyroxene+spinel cumulate xenoliths at Colli Albani (Gaeta *et al.*, 2009; Di Rocco *et al.*, 2012). Reaction between carbonate and magmatic melt increases the stability of clinopyroxene and, in more evolved melts, of plagioclase also

(e.g. Mollo *et al.*, 2010). This results in a wall-rock grading from a cumulate zone adjacent to the magma body (endoskarn), to skarn assemblages at the limestone contact (exoskarn). Skarn-derived Ca-rich melts are inferred (Wenzel *et al.*, 2002; Gaeta *et al.*, 2009) to be the main source of carbonate components contaminating the magmatic melt. Our magmatic skarn xenoliths are perfect examples of these processes. Zones R1 to R3 constitute the cumulate zone formed under the influence of carbonate assimilation. Similar to cumulates at Ioko-Dovyren (Wenzel *et al.*, 2002) and Colli Albani (Gaeta *et al.*, 2009), clinopyroxenes and plagioclase in these zones show only relatively subtle variations in mineral chemistry from magmatic-derived mineral compositions that reveal their origin through carbonate contamination. The CaO-enriched, glass-rich zone R4 captures the process of magmatic melt contamination, and the xenolith cores in some samples preserve very rare instances of the actual calcite carbonate melt (see Whitley *et al.*, 2019). This carbonate melt has since only been inferred to occur during other instances of carbonate assimilation (Wenzel *et al.*, 2002; Barnes *et al.*, 2005; Gaeta *et al.*, 2009), whilst the magmatic skarns at Merapi preserve and demonstrate direct evidence for its existence.

A syn-magmatic origin for these xenoliths, i.e. formation by direct magma–carbonate contact during magmatic events such as eruptive periods, is consistent with the presence of glass and additionally with the low pressures of 37–93 MPa (corresponding to < 3.5 km) estimated from fluid-inclusion barometry. These pressures are similar to some pressure estimates derived from re-equilibrated melt inclusions in magmatic clinopyroxenes at Merapi (Nadeau *et al.*, 2013*b*; Preece *et al.*, 2014), and they are lower than pressures estimated for the main pre-eruptive magma chamber or reservoir at Merapi (100–400 MPa, corresponding to depths of ~4–15 km; Commer *et al.*, 2006; Chadwick *et al.*, 2013; Costa *et al.*, 2013; Preece *et al.*, 2014; Erdmann *et al.*, 2016; Deegan *et al.*, 2016b). This indicates that the fluid inclusions re-equilibrated during ascent, or formed at very shallow crustal pressures. The lack of a 're-equilibration tail' (Hansteen & Klügel 2008) and no evidence for pressures > 100 MPa in our fluid-inclusion dataset suggest that re-equilibration is unlikely, and instead are indicative of fluid-inclusion formation in small ephemeral pre-eruptive reservoirs or during magmatic ascent during eruptive periods.

Patchy zoned clinopyroxenes with prominent irregular resorption surfaces (Fig. 7) show that this syn-magmatic carbonate interaction is a dynamic process, under temporarily variable imposed oxygen-fugacity conditions caused by rapid CO_2 release (Fig. 14) (cf. Mollo *et al.*, 2010). Variations in the ability of this CO_2 to migrate from the reaction site (Ganino *et al.*, 2008; Blythe *et al.*, 2015) may cause the variation in oxygen fugacity across texturally similar samples, and even within xenolith zones. Al, Fe^{3+}-rich clinopyroxene cores and andraditic-rich garnet indicate high initial oxygen-fugacity conditions (Figs. 7, 14; Meinert, 2005; Mollo & Vona, 2014), whilst diopside-rich cores indicate high initial carbonate-derived Ca activity in the melt (Zarayskiy *et al.*, 1987). Increasing CO_2 release causes clinopyroxene Fe-enrichment in the mantle and rims (Zarayskiy *et al.*, 1987) to higher values than observed in magmatic clinopyroxenes in the later stages of xenolith formation (Fig. 7). Fe is additionally concentrated in plagioclase as An concentrations decrease (Fig. 6).

Although we propose that the magmatic skarn xenoliths reflect crystallization from a Ca-contaminated melt, it is interesting to note that their mineralogical zonation still bears a strong resemblance to contact metamorphic zoned bimetasomatic skarns and experimental reconstructions of these, such as produced during granodiorite–calcite interaction experiments (Zarayskiy *et al.*, 1987). Magmatic skarn xenolith samples with a garnet + CaTs clinopyroxene zone (zone R3b in Fig. 1) represent the exo/endoskarn transition in natural skarns, where carbonate-derived elements are transferred to the magmatic system (clinopyroxene + plagioclase endoskarns, zones R1–R3). In turn, certain magma-derived elements are transferred to the carbonate protolith forming garnet + wollastonite + DiHd/CaTs clinopyroxene exoskarns (zone R3b and the xenolith cores), reflected also in the chemistry of the individual zones (Fig. 5).

The dissolution of carbonate in high-temperature mafic magmatic melts has been experimentally confirmed to operate on the order of hours (Deegan *et al.*, 2010; Jolis *et al.*, 2013), but mineral equilibration is slower (cf. Carter and Dasgupta, 2016). First-order constraints on the timescales of carbonate interaction at Merapi can be tentatively placed using the growth rate of xenolith mineral phases such as clinopyroxenes. Experimental and measured growth rates for euhedral clinopyroxenes in basaltic to andesitic magmatic systems are on the order of 10^9 to 10^7 cm/s (e.g. Kouchi *et al.*, 1983; Simakin *et al.*, 2003; Orlando *et al.*, 2008; Kilgour *et al.*, 2014). Assuming similar growth rates for the clinopyroxenes in the xenoliths, a typical 300-μm clinopyroxene in zone R4, which has a composition entirely different from that of the Merapi magmatic clinopyroxenes (Fig. 7) and therefore formed uniquely during magma–carbonate interaction, could have formed in 3.5 to 347 days. Measurements of the growth rate of skarn formation between granodiorite and calcite, and between quartz and brucite marble in the experiments of Zarayskiy *et al.* (1987) indicate similar timescales. Although clinopyroxene growth rates are poorly constrained, especially in magma–carbonate systems, it is conceivable that the xenoliths could have formed on shorter timescales, for example in the lead-up to and during eruptive periods. The associated CO_2 release may then be able to influence eruption dynamics (cf. Troll *et al.*, 2012). Future work utilizing diffusive timescales would potentially increase the accuracy of these timescale estimates and aid hazard assessment at Merapi.

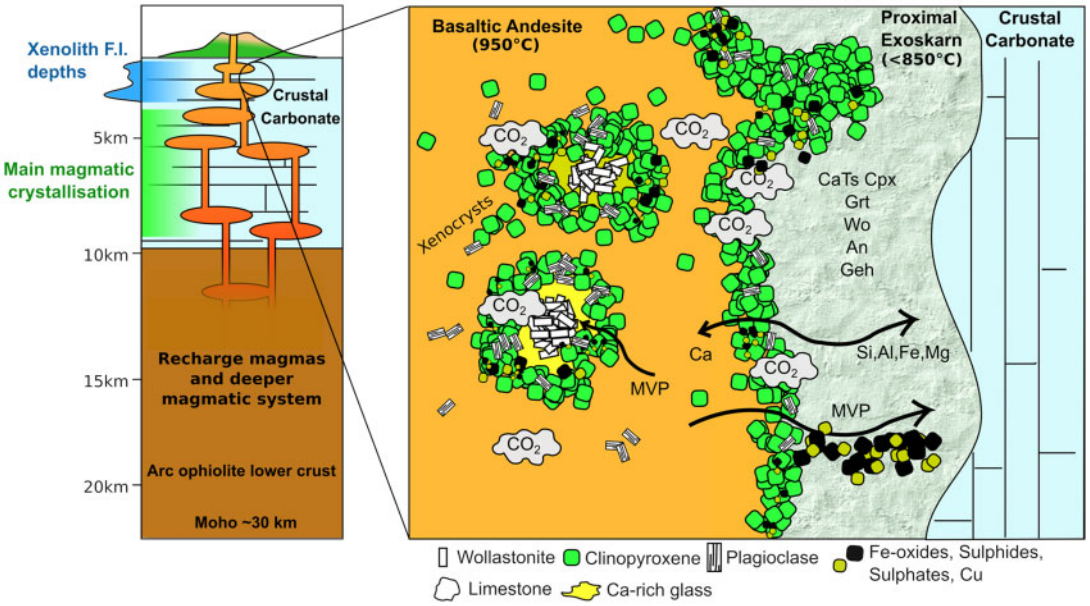

Fig. 15. Summary of the processes occurring during magma–carbonate interaction at Merapi. Carbonate is rapidly digested, forming a Ca-rich contaminated melt, from which wollastonite and other phases precipitate, forming the magmatic skarn xenoliths. Proximal to the magmatic melt, clinopyroxene and plagioclase form from Ca transfer to the melt from the carbonate. The abundance of melt in the xenoliths allows disaggregation and disperses xenolith crystals into the magma (e.g. Deegan *et al.*, 2010). The magmatic volatile phase (MVP, cf. Nadeau *et al.*, 2010; Preece *et al.*, 2014) infiltrates the xenoliths, forming rare halogen- and sulphur-bearing minerals. At the wall-rock contact, abundant clinopyroxene forms, partially insulating the carbonate and skarn. Magma-derived elements are transferred to the wall rock, influenced by the increasing oxygen fugacity caused by CO_2 flushing, forming the exoskarn mineralogy. Regions of main magma crystallization from Chadwick *et al.* (2013), Preece *et al.* (2014) and Erdmann *et al.* (2016). Moho depth from Wölbern & Rümpker (2016). Description of the lower crust from van Bemmelen (1949).

In summary, we propose that the magmatic skarn xenoliths are syn-magmatic in origin, forming as a result of limestone dissolution into a magmatic melt, from which skarn minerals precipitate (Fig. 15). Localized changes in oxygen fugacity caused by the CO_2 released to the fluid phase influenced the composition of the minerals formed. Variable transfer of Ca from limestone, and magma-derived elements, form zonations similar to those observed in metasomatic skarns, but at above solidus temperatures. The composition of the zones is controlled by element transfer between magma and limestone and by the stability and abundance of the major minerals that form in the respective zones. Our evidence of syn-magmatic magma–carbonate interaction is in agreement with previous studies on Merapi magma–carbonate interaction (Deegan *et al.*, 2010, 2016*a*; Troll *et al.*, 2012), at Vesuvius (Blythe *et al.*, 2015; Jolis *et al.*, 2015) and at Colli Albani (Iacono-Marziano *et al.*, 2007; Freda *et al.*, 2011), which all note the likely very rapid, syn-eruptive timescales of carbonate dissolution and CO_2 liberation. If correct, this process has the potential to enhance eruption explosivity owing to external CO_2 additions.

Exoskarn xenoliths

Exoskarn xenoliths contain dominantly Al+Si+Ca-bearing phases, and $<$ 10 wt % FeO+MgO based on calculated whole-rock compositions. Although the high Al could be indicative of a marl protolith, we believe that these samples come from a calcite-bearing protolith with input from magmatically derived elements, on the basis of calcite oxygen isotopes showing evidence of interaction with magmatic fluids (Whitley *et al.*, 2019), and the presence of F-Cl-S-rich phases most likely derived from magmatic volatiles.

The exoskarn xenoliths lack the interstitial glass, melt inclusions and mineralogical zonation of the magmatic skarn xenoliths, with only a clinopyroxene $\pm$ plagioclase reaction rim at the lava contact. Melt-inclusion compositions within these rim clinopyroxenes are indistinguishable from the lava groundmass glasses (Fig. 9). The core assemblage (garnet + CaTs clinopyroxene + wollastonite + anorthite $\pm$ gehlenite) is distinct from the magmatic skarn xenoliths (wollastonite $\pm$ glass $\pm$ DiHd clinopyroxene $\pm$ garnet $\pm$ anorthite). The much higher fO_2 conditions recorded in the clinopyroxenes (Fig. 14) indicate that these xenoliths experienced a longer period of CO_2 flushing than the magmatic skarn xenoliths did (cf. Ganino *et al.*, 2008). This, coupled with the distinct mineralogy, a lack of glass and a lack of mineralogical zonation, suggests that the exoskarn xenoliths originate from a contact metamorphic aureole (exoskarn) around the upper crustal Merapi magma reservoir system (Fig. 15). The dominance of high-temperature anhydrous mineral assemblages indicates that they are sourced proximal to the magma

reservoir. Contact metamorphic aureoles can be extensive in size (Aarnes *et al.*, 2010). We therefore we expect low-temperature distal skarn assemblages to be present at Merapi, but these may not have been frequently sampled during this study, possibly because of the high-temperature 'skarn shell' (cf. Fulignati *et al.*, 2001; Jolis *et al.*, 2015) being overrepresented in our dataset.

The presence of spinel, as observed in one of our samples (MX99-3s), has been noted in several case studies on magma–carbonate interaction (e.g. Wenzel *et al.*, 2002; Gaeta *et al.*, 2009; Spandler *et al.*, 2012). For instance, hercynitic spinel is widespread in skarns from the Italian volcanic provinces. Skarns from the Colli Albani Volcanic District (Italy) contain Al-rich spinel in textural equilibrium with glass, which has been interpreted to reflect the melting of calcite and mixing of this melt with the host magma (Gaeta *et al.*, 2009). Metasomatic development through leaching has been invoked to explain the occurrence of banded forsterite–spinel skarns in ejecta from the 1631 Vesuvius eruption (Pascal *et al.*, 2009). Experimental work on magma–carbonate interaction with andesitic (Carter & Dasgupta, 2016) and basanitic (Conte *et al.*, 2009) magmas also produced aluminous spinel. Clearly, the presence of aluminous spinel is a common characteristic of carbonate assimilation. None of these studies, however, shows the unique texture and association with gehlenite, as in sample MX99-3s, and we classify this sample as exoskarn (type B) based on the lack of glass and the mineralogical differences from the more common magmatic skarns at Merapi.

Volatiles and metal transport

The numerous F-Cl-S phases identified in the xenoliths record evidence of interaction with a magmatic-derived volatile phase (MVP; cf. Nadeau *et al.*, 2010; Preece *et al.*, 2014) during the formation of the xenoliths. Although F-Cl-S-bearing phases indicate the presence of an aqueous fluid, there is no clear evidence of the role of H_2O during xenolith formation. Silicate magma has a limited capacity to dissolve the excess liberated crustal-derived CO_2, and any increase in melt CO_2 would strongly reduce the solubility of H_2O (e.g. Tamic *et al.*, 2001), increasing the free H_2O available during magma–carbonate interaction. The xenoliths, however, contain anhydrous mineral assemblages, and fluid inclusions are two-phase liquid CO_2 + vapour CO_2, with only very rare small fluid inclusions containing unidentified daughter crystals. Excess CO_2 in the magma causes the typical wollastonite-forming reaction $SiO_2 + CaCO_3 \rightarrow CaSiO_3 + CO_2$ to favour the reactants and promote skarn mineral formation.

F-Cl-S-bearing phases are found within both magmatic and exoskarn xenoliths; however, they are not found in every magmatic skarn xenolith sample. In the magmatic skarn xenoliths, they are found in zone R2 (anhydrite surrounding pyrrhotite ± cubanite) and zone R3b (ellestadite) and as interstitial patches the wollastonite-dominant cores. These patches contain cuspidine, fluorite and the wadalite-like mineral, whilst anhydrite, apatite and cotunnite ($PbCl_2$) are found as accessory phases elsewhere in the cores. Pyrrhotite, cubanite, Fe-oxides and apatite are sometimes found as daughter crystals in melt inclusions. The presence of fluorine-bearing phases in sample MX1 is closely related to the presence of calcite with a melt-like texture, consistent with fluorine lowering the melting temperature of calcite (Jago & Gittins, 1991; Gorzkowska *et al.*, 1988*a*, 1988*b*; see Whitley *et al.*, 2019 for more detail). Chlorine and limited data for F in the Ca-rich xenolith core interstitial glass and melt inclusions do not show elevated concentrations compared with the lavas. This suggests that the volatile-rich minerals are unlikely to have precipitated directly from the melt, like the wollastonite, clinopyroxene and plagioclase, but are instead the result of interaction with this magmatic-derived volatile phase. In sample MX1, the melt-like calcite is in places replaced by the wadalite-like mineral, which retains the calcite texture (Fig. 3). Instances where garnet is replaced by this wadalite-like phase may be the result of reaction with magmatic HCl (e.g. Fujita *et al.*, 2001). Calcite additionally reacts with fluorine to form fluorite as distinct crystal phases, and as radial growths around a vesicle touching calcite (Fig. 3a, b), suggesting that fluorine is an important component of the volatile phase.

The exoskarn xenoliths additionally contain phases enriched in magmatic-derived volatiles. For instance, ellestadite is found throughout the xenoliths, and rare pyrrhotite and anhydrite are present in some samples, but the majority of volatile-rich phases (cuspidine, anhydrite, ellestadite, fluorite, spurrite) are concentrated in the reaction rims around residual large calcite crystals. A magmatic fluid source for these mineral phases is evidenced by calcite oxygen isotopic shifts towards magmatic values (Whitley *et al.*, 2019) and elevated trace-element LREE/HREE in these calcites compared with marine limestone (Supplementary Fig. S5; Supplementary Table S1).

The presence of the magmatic-derived volatile phase within the xenoliths indicates the potential for economic metal mineralization beneath Merapi and similar carbonate-hosted arc volcanoes in the region. Oxidized silicic calc-alkaline arc intrusions are frequently associated with porphyry Cu, Zn, Pb and Fe deposits (Meinert, 2005). Ubiquitous calc-silicate xenoliths at Merapi provide evidence for skarn formation, and garnet and clinopyroxene compositions in these xenoliths overlap those characteristic of Cu, Zn and Fe skarns (Meinert, 1992). Although these economic metals are rare in our studied xenoliths, our data suggest that ongoing mineralization may occur at depth beneath Merapi within the upper part of the plumbing system, during the later stages of magmatic evolution at Merapi.

Sulphur-bearing arc magmas are important sources of Cu, and Cu transport has been noted across the Sunda arc (Nadeau *et al.*, 2010; Agangi & Reddy, 2016). Globules of Cu-rich sulphide melt are found in the

Merapi lavas, recording evidence of Cu-rich sulphide melts exsolving from primitive magma, which are later dissolved in the magmatic-derived volatile phase and distributed through more evolved magmas, and potentially into the host-rock system (Nadeau *et al.*, 2010, 2013a). As previously discussed, the xenoliths are evidence of interaction between this Cu-S-enriched fluid phase and carbonate. In the magmatic skarn xenoliths, Cu is found as cubanite and as a minor constituent in pyrrhotite in zone R2, which both minerals are generally surrounded by anhydrite. Disproportionation of SO_2 into sulphide and sulphate is a potential mineralization process in carbonate and calcium-bearing rocks. It can occur on the timescale of hours (Mavrogenes & Blundy, 2017), and may have formed the coexisting pyrrhotite + cubanite + anhydrite in the xenoliths. Within the magmatic skarn xenolith cores, Cu is rare, only found as a cubanite inclusion in a plagioclase-hosted melt inclusion, and as a minor constituent in pyrrhotite inclusions within CaTs-rich clinopyroxene cores. The relative abundance of Cu in zone R2 compared with the core (and exoskarn xenoliths) shows limited transfer of the magmatic-derived volatile phase into the xenolith cores, and/or conditions unfavourable for Cu deposition. Oxygen fugacity is estimated to be similar to typical oxidized arc magma conditions in zone R2 ($\sim\Delta$NNO + 1), producing favourable conditions for sulphur transport and deposition (e.g. Hattori, 2018). The higher oxygen fugacity estimated in some xenolith cores from the presence of anhydrite and CaTs clinopyroxene cores ($\leq \Delta$NNO + 4) is potentially too high for Cu transfer, as an upper limit to mineralization at the hematite–magnetite ($\sim\Delta$NNO + 4) buffer may exist for porphyry copper deposition (Sun *et al.*, 2013). The large volumes of CO_2 released during decarbonation of the original carbonate, which causes this fO_2 increase, combined with magmatic CO_2, strongly reduces Cu solubility in the fluid phase (van Hinsberg *et al.*, 2016; Kokh *et al.*, 2017). Vesicles are found within zones proximal to the host lava and the core, suggesting that a high XCO_2 in zone R2 may promote the deposition of Cu before it can be transferred fully into the xenolith core. Xenolith formation temperatures are additionally higher than those estimated for the bulk of Cu and Au deposition in copper porphyry systems (starting $< 700^\circ$C and dominantly $< 400^\circ$C), where fluid immiscibility produces coexisting vapour-rich and saline fluid inclusions (Sillitoe, 2010), which are not observed in the xenoliths studied here.

Our model, in which carbonate is assimilated into a melt from which skarn minerals precipitate (magmatic skarns), has been discussed as a process occurring in many Chinese Cu-Fe-Au-deposits (e.g. Bin & Jin-song, 2016). The xenoliths of this study demonstrate that Cu-Fe sulphides can be formed during this process, and may be capable, at least in part, of producing metal sulphide deposits. Magnetite, hematite and Fe-enrichment in some silicate phases may additionally indicate iron oxide ore potential. Whilst we only have xenoliths that show Cu deposition proximal to the Merapi magma reservoir (no low-temperature hydrous skarn phases observed), Cu deposition may occur at greater distances into the contact aureole. Percolation of a Cu-bearing magmatic volatile phase through the carbonate over a longer period of time, on cooling when large amounts of magmatic fluids are released, has the potential to promote sulphide and Fe-oxide deposition, enhancing ore-forming potential such as observed in copper porphyry systems (e.g. Landtwing *et al.*, 2005; Sillitoe, 2010).

Implications of carbonate interaction for the Merapi magmatic system

Xenocryst cargo

Calc-silicate xenoliths are ubiquitous in Merapi eruptive deposits, showing that magma–carbonate interaction is an ongoing process at Merapi. The amount of interaction is debated in the literature, with estimates of mixing up to 40% recorded in some samples on the basis of isotopic modelling (Troll *et al.*, 2013; Borisova *et al.*, 2013, 2016). Although our study cannot elaborate on estimating the volume of carbonate that interacts with Merapi magmas, our data suggest that calc-silicate-derived crystals (xenocrysts) may be more difficult to recognize in erupted magmatic deposits than previously appreciated, as we discuss below.

Incorporation of skarn-derived minerals into the Merapi magmatic system has been shown previously (Chadwick *et al.* 2007; Deegan *et al.*, 2010; Borisova *et al.*, 2016; Deegan *et al.*, 2016b). Chadwick *et al.* (2007) suggested that 6% to 12% of crystalline material at Merapi may be crust-derived, based on elevated $^{87}Sr/^{86}Sr$ plagioclase compositions and distinct major-element plagioclase chemistry. Similarly, thermodynamic-geochemical models for the 2010 Merapi eruption are consistent with the incorporation of 18% of crustal calc-silicate material (Borisova *et al.*, 2016). Based on a detailed oxygen isotope study, Borisova *et al.* (2016) were even able to distinguish two stages of magma–crust interaction, resulting in distinct xenocryst plagioclase $\delta^{18}O$ values related either to high-T altered crustal rocks depleted in ^{18}O or to ^{18}O-enriched assimilated carbonate material. Our data show that both plagioclase and clinopyroxene compositions are produced during magma–carbonate interaction in zones R1 and R2 that completely overlap magmatic compositions in respect to major elements (Figs. 6, 7). These minerals are formed as a result of Ca transfer from carbonate to the melt, such as occurs within endoskarns. Increased stability of clinopyroxene and plagioclase in carbonate-contaminated melts has been experimentally confirmed across a range of magmatic compositions (e.g. Iacono-Marziano *et al.*, 2007; Mollo *et al.*, 2010; Carter & Dasgupta, 2016), and with rhyoliteMELTS (version 1.2; Gualda *et al.*, 2012; Ghiorso, 2016), which successfully reproduced Ca-contaminated xenolith glass and basaltic andesite compositions. Mineral compositions that are distinct from

those found in the magma occur from zone R3 to the xenolith core, but, to our knowledge, no highly CaTs-enriched, skarn-derived clinopyroxenes have yet been detected in the magmatic products. Although Al-rich clinopyroxenes (up to 8 wt %) are discussed in Costa *et al.* (2013), and were attributed to higher-pressure magmatic crystallization, we found none in our literature data synthesis that compositionally matched our specific skarn clinopyroxenes. Clinopyroxene compositions matching zones R3 and R4, which lie on the Di–Hd join and are volumetrically more abundant, are also exceedingly rare in the lavas, with only 3 out of the 431 analyses reported in Preece (2014) overlapping these compositions. The lack of these compositions may be due to a volumetrically smaller amount of 'exotic' compositions in the xenolith cores compared with magmatic-type compositions in the xenolith endoskarn rims. Alternatively, dissolution into the magma, and/or re-equilibration with the magma might also be a possible explanation. Indeed, Carter & Dasgupta (2016) showed that in carbonate assimilation experiments, within 48 hours initially compositionally variable clinopyroxenes had equilibrated to a diopsidic composition. Some crystals that are a result of magma–carbonate interaction may therefore be 'cryptic' and distinguishable from magmatic crystals only on the basis of their isotope or trace-element chemistry (e.g. Chadwick *et al.*, 2007; Borisova *et al.*, 2016). Another consequence of this finding is that clinopyroxene thermobarometry may include carbonate-interaction pressures and temperatures in their output. Although in situ oxygen isotope evidence for magma–carbonate interaction in Merapi clinopyroxene shows limited crustal additions to the bulk of the crystals (Deegan *et al.*, 2016b), a small number of the clinopyroxenes analysed by Deegan *et al.* (2016b) have anomalously high oxygen isotope ratios ($\delta^{18}O$ values of up to c. 7‰), which may be a result of magma–carbonate interaction. Furthermore, studies utilizing in situ isotope analysis of other mineral phases such as plagioclase for Sr (Chadwick *et al.*, 2007) and oxygen (Borisova *et al.*, 2016) have demonstrated the presence of xenocrysts and contaminated mineral zones, consistent with the usually shallow crystallization of intermediate plagioclase (e.g. Chadwick *et al.*, 2013). Whilst our plagioclase data for the glass-rich zone R4 have high-FeO that overlaps some literature values for plagioclase in lavas, and therefore may suggest that high-FeO plagioclase in lavas might be xenocrystic, this is more likely to be a result of disequilibria due to quenching of the xenolith glass. For example, FeO in plagioclase increases with cooling rate, producing plagioclase with up to 2.33 wt % FeO in 15°C/min experiments (Mollo *et al.*, 2011). The zone R4 plagioclase crystals contain up to 1.7 wt % FeO, and similarly wollastonite crystals in zone R4 have thin Fe-rich ferro-bustamite overgrowths, indicating that the cooling rate may have a more pronounced impact on Fe-rich mineral rims in the xenoliths.

Magma composition

Much of the experimental work on magma–carbonate interaction focuses on reproducing the highly potassic, silica-undersaturated compositions erupted at volcanoes such as Vesuvius and Colli Albani (e.g. Iacono-Marziano *et al.*, 2007; Mollo *et al.*, 2010; Jolis *et al.*, 2013). Strong silica-undersaturation from carbonate assimilation in Italian volcanoes is a result of the increased stability of clinopyroxene taking up SiO_2, coupled with the redissolution of olivine, which drives melts towards silica undersaturation (e.g. Mollo *et al.*, 2010). Recent Merapi lava whole-rock compositions range from ~50 to 68 wt % SiO_2, and the interstitial glasses within these record pre-eruptive melts with 60–75 wt % SiO_2 (Fig. 9). These would not be driven to silica-undersaturation by an increase in clinopyroxene or plagioclase precipitation due to these minerals containing lower SiO_2 concentrations than melt compositions. Whole-rock compositions instead traverse a differentiation vector defined by that of the typical arc magma plagioclase and clinopyroxene differentiation assemblage (Fig. 9; cf. Handley *et al.*, 2014), although at a slightly elevated CaO. It is interesting to note, however, that while the overall major-element chemistry at Merapi is not dominated by a carbonate assimilation signature, very rare, highly localized phonolitic leucite-bearing silica-undersaturated melts were identified in some Merapi calc-silicate xenoliths by Brouwer (1928, 1945). These results demonstrate that these exotic compositions can be formed at Merapi during very localized periods of extremely high levels of carbonate interaction, but the quantities of melt generated are volumetrically negligible.

In addition to the effects of crystal fractionation on the major-element chemistry, lower-temperature, high-SiO_2 melts such as those represented by the groundmass lava glass compositions at Merapi have a lower capacity to assimilate material than hotter mafic melts (e.g. Wenzel *et al.*, 2002; Barnes *et al.*, 2005; Gaeta *et al.*, 2009; Jolis *et al.*, 2015), and instead favour the formation of skarn minerals (e.g. wollastonite) that cause only small apparent changes to melt compositions (Spandler *et al.*, 2012; Carter & Dasgupta, 2016). These minerals may become trapped as a cumulate or exoskarn layer (see above, e.g. Gaeta *et al.*, 2009; Di Rocco *et al.*, 2012) at the wall-rock contact, and only have a small impact on the melt composition during skarn recycling and xenocryst incorporation (e.g. Di Rocco *et al.*, 2012; Jolis *et al.*, 2015). The discrepancy between limited whole-rock major-element evidence for magma–carbonate interaction (cf. Costa *et al.*, 2013; Handley *et al.*, 2014) and the high levels of interaction recorded in multiple isotope systems (Chadwick *et al.*, 2007; Troll *et al.*, 2013; Borisova *et al.*, 2013, 2016) may thus be due to a combination of the lower capacity of the magmatic melt to incorporate carbonate material, and the relatively limited mobility of Ca in these relatively low-temperature, high-SiO_2 Merapi pre-eruptive melts compared with the

higher mobilities usually displayed by isotopes of trace elements (e.g. Sr, B). This decoupling has been observed in high-temperature (1200°C) carbonate interaction experiments (Deegan *et al.*, 2010, 2016*a*; Blythe *et al.*, 2015). Moreover, quantitative modelling of magma–carbonate interaction demonstrated that low-to-moderate amounts of carbonate assimilation cause only limited changes to the major-element chemistry of the magma (Spandler *et al.*, 2012). Although there is no doubt that magma–carbonate interaction is an important petrogenetic process at Merapi, the degree of major-element compositional change may not be prominent enough to distinguish the modified magma from the overall spectrum of Merapi magmas (cf. Spandler *et al.*, 2012).

Merapi volatile budget

Carbonate assimilation at Merapi has been shown to have a strong impact on the composition of the gases released to the atmosphere. The release of crust-derived CO_2 has been proposed by identification of elevated $\delta^{13}C$ and He isotopes in fumarole gases (Troll *et al.*, 2012, 2013 and references therein). An increase in these isotopic tracers has additionally been observed during eruptive periods, attributed to a positive feedback loop of wall-rock fracturing during eruption, and increased CO_2 liberation from magma–carbonate interaction on this increased surface area (Deegan *et al.*, 2011; Troll *et al.*, 2012; Carr *et al.*, 2018). Our work shows that the magmatic skarn xenoliths may represent snapshots of this syn-magmatic carbonate interaction, and therefore eruptive flare-ups could potentially be influenced by temporal increases in carbonate interaction (cf. Troll *et al.*, 2012; Carr *et al.*, 2018). The 2010 eruption was preceded by an influx of hotter volatile-rich magma that exceeded the capacity of the shallow storage system (Costa *et al.*, 2013; Preece *et al.*, 2016; Carr *et al.*, 2020). This increased heat and volume would have caused both increased thermal decarbonation and fracturing, which could penetrate deeper into the bedrock. A positive feedback would then occur, where increased decarbonation promotes a decrease in water solubility, producing bubbles and more explosive behaviour, promoting more fracturing, resulting in temporal increases in carbonate interaction (Deegan *et al.*, 2011; Troll *et al.*, 2012; Carr *et al.*, 2018; 2020). Dome instability from weakened fractured/altered wall rock could also contribute to magmatic overpressure through increasing fracturing, and a resulting larger surface area of the carbonate available to react (Mollo *et al.*, 2012). In the magmatic skarn xenoliths, residual calcite is present only in trace quantities, and the $\delta^{13}C$ compositions of these calcites are exceptionally negative (down to –29‰), demonstrating extremely efficient decarbonation in the magmatic skarn xenoliths (Whitley *et al.*, 2019). It is unlikely that this is exclusive to Merapi, and indeed, temporal increases in carbonate assimilation leading to increased explosivity has been proposed elsewhere, for example at Colli Albani (Freda *et al.*, 2011) and Vesuvius (Jolis *et al.*, 2015). Crustal CO_2 release is not restricted to eruptive periods however, and decarbonation reactions in the exoskarn additionally contribute to the CO_2 budget. The current CO_2 output at Merapi compared with estimated contact metamorphic aureole volumes around a Merapi reservoir demonstrate that this CO_2 release is rapid, on timescales of just thousands of years (Whitley *et al.*, 2019). When considering volcanoes that interacted with crustal carbonate, at present and in the geological past (cf. Mason *et al.*, 2017; Carter and Dasgupta, 2018), CO_2 release such as evidenced at Merapi may have the potential to modify long-term climatic trends.

CONCLUSIONS

A detailed mineralogical, petrological and geochemical study of a range of calc-silicate (skarn-type) xenoliths from Merapi volcano shows that two distinct types of xenoliths are present: magmatic skarn xenoliths that record syn-magmatic magma–carbonate interaction that preserves abundant CaO-rich glass; and fragments of the metasomatic exoskarn aureole around the Merapi magma reservoir. Thermobarometry indicates that the CaO-rich glass-bearing magmatic skarn xenoliths formed at ~850°C. Fluid inclusions record shallow pressures of < 100 MPa, corresponding to depths < 3.7 km. These xenoliths are the physical representation of carbonate entrained during eruptive events, which we interpret to increase eruption intensity during rapid decarbonation. The disaggregated nature of some of these xenoliths, and the similarity in the geochemistry of lava and some xenolith minerals indicate that skarn-derived xenocrysts may be difficult to recognize at Merapi. Experimental comparisons and thermodynamic modelling indicate formation temperatures of 510 to 910°C for the range of mineralogies shown in the metasomatic exoskarn xenoliths. A newly developed oxybarometric model indicates a wide range of fO_2 conditions during xenolith formation. Magmatic skarn xenoliths are predominantly formed around the NNO buffer, similar to magmatic values, whilst the cores of these xenoliths can reach values above the HM buffer in the presence of an increased amount of newly released CO_2. Protracted periods of CO_2 flushing caused conditions predominantly above the NNO buffer during exoskarn formation, covering the full range between NNO and air. High fO_2 in both xenolith types promoted the formation of andradite garnet and highly aluminous clinopyroxene compositions. A magmatic volatile phase present at Merapi reacts with the xenoliths to form rare Ca-Al-Si-F-Cl phases such as cuspidine, ellestadite and wadalite-like phases. Evidence of xenolith formation during eruptive timescales demonstrates that magma–carbonate interaction and subsequent CO_2 release could affect eruption intensity, as recently suggested for Merapi and similar carbonate-hosted

volcanoes elsewhere. In addition, copper and occasionally Fe (and likely other associated elements of economic value such as Zn) are carried within this fluid and are found concentrated in the outer shells of some of the xenoliths, indicating the potential for ongoing skarn-type mineralization at depth beneath Merapi and similar volcanoes hosted within a carbonate basement worldwide.

ACKNOWLEDGEMENTS

We thank Barbara Mader and Peter Appel (Kiel University) for assistance with microprobe analyses, Petra Herms (Kiel University) for advice about fluid-inclusion analysis, Vladimir Zholobenko (Keele University) for assistance with Raman analysis, and Luke Hepworth for additional calcite EPMA analyses. Peter Greatbatch's and David Wilde's (Keele University) thin-section preparation skills are greatly appreciated. We also thank Dorota Środek (University of Silesia) for discussion about the unusual skarn minerals. Massimio d'Antonio and Anastassia Borisova are thanked for providing constructive reviews that helped to improve the manuscript, and we also thank Gerhard Wörner for editorial handling. Financial support from NERC (grant IMF620/0517), Keele University, the Keele Postgraduate Association, and the Swedish Research Council is gratefully acknowledged.

SUPPLEMENTARY DATA

Supplementary Data are available at *Journal of Petrology* online.

REFERENCES

Aarnes, I., Svensen, H., Connolly, J. A. D. & Podladchikov, Y. Y. (2010). How contact metamorphism can trigger global climate changes: modelling gas generation around igneous sills in sedimentary basins. *Geochimica et Cosmochimica Acta* **74**, 7179–7195.

Agangi, A. & Reddy, S. M. (2016). Open-system behaviour of magmatic fluid phase and transport of copper in arc magmas at Krakatau and Batur volcanoes, *Indonesia. Journal of Volcanology and Geothermal Research* **327**, 669–686.

Aiuppa, A., Fischer, T. P., Plank, T., Robidoux, P. & Di Napoli, R. (2017). Along-arc, inter-arc and arc-to-arc variations in volcanic gas CO_2/S*T* ratios reveal dual source of carbon in arc volcanism. *Earth-Science Reviews* **168, 24–47.**

Anderson, A. (1973). The before-eruption water content of some high-alumina magmas. *Bulletin Volcanologique* **37**, 530–552.

Anderson, A. T. (1974). Evidence for a picritic, volatile-rich magma beneath Mt. Shasta, California. *Journal of Petrology* **15**, 243–267.

Andreastuti, S., Alloway, B. & Smith, I. (2000). A detailed tephrostratigraphic framework at Merapi Volcano, Central Java, Indonesia: implications for eruption predictions and hazard assessment. *Journal of Volcanology and Geothermal Research* **100**, 51–67.

Arai, H. (2010). A function for the R programming language to recast garnet analyses into end-members: revision and porting of Muhling and Griffin's method. *Computers & Geosciences* **36**, 406–409.

Barnes, C. G., Prestvik, T., Sundvoll, B. & Surratt, D. (2005). Pervasive assimilation of carbonate and silicate rocks in the Hortavær igneous complex, north-central Norway. *Lithos* **80**, 179–199.

Berndt, J., Koepke, J. & Holtz, F. (2005). An experimental investigation of the influence of water and oxygen fugacity on differentiation of MORB at 200 MPa. *Journal of Petrology* **46**, 135–167.

Bin, Z. & Jin-song, Z. (2016). The main features of magmatic skarns and their formation mechanism. *AshEse Journal of Engineering* **2**, 22–65.

Blythe, L. S., Deegan, F. M., Freda, C., Jolis, E. M., Masotta, M., Misiti, V., Taddeucci, J. & Troll, V. R. (2015). CO_2 bubble generation and migration during magma–carbonate interaction. *Contributions to Mineralogy and Petrology* **169**, 1–16.

Bolio-Arceo, H. & Glasser, F. P. (1990). Formation of spurrite, $Ca_5(SiO_4)_2CO_3$. *Cement and Concrete Research* **20**, 301–307.

Borisova, A. Y., Gurenko, A. A., Martel, C., Kouzmanov, K., Cathala, A., Bohrson, W. A., Pratomo, I. & Sumarti, S. (2016). Oxygen isotope heterogeneity of arc magma recorded in plagioclase from the 2010 Merapi eruption (Central Java, Indonesia). *Geochimica et Cosmochimica Acta* **190**, 13–34.

Borisova, A. Y., Martel, C., Gouy, S., Pratomo, I., Sumarti, S., Toutain, J.-P., Bindeman, I. N., de Parseval, P. & Métaxian, J.-P. (2013). Highly explosive 2010 Merapi eruption: evidence for shallow-level crustal assimilation and hybrid fluid. *Journal of Volcanology and Geothermal Research* **261**, 193–208.

Borisova, A. Y., Toutain, J.-P., Dubessy, J., Pallister, J., Zwick, A. & Salvi, S. (2014). H_2O-CO_2-S fluid triggering the 1991 Mount Pinatubo climactic eruption (Philippines). *Bulletin of Volcanology* **76**, 800.

Brouwer, H. (1928). Production of trachyte and phonolite from pyroxene andesitic magma associated with limestone. *Journal of Geology* **36**, 545–548.

Brouwer, H. A. (1945). *The Association of Alkali Rocks and Metamorphic Limestone in a Block Ejected by the Volcano Merapi (Java).* Koninklijke Nederlandse Akademie van Wetenschappen, Amsterdam, **48**, 166–189.

Büttner, S. H. (2012). Rock Maker: an MS Excel™ spreadsheet for the calculation of rock compositions from proportional whole rock analyses, mineral compositions, and modal abundance. *Mineralogy and Petrology* **104**, 129–135.

Camus, G., Gourgaud, A., Mossand-Berthommier, P.-C. & Vincent, P.-M. (2000). Merapi (Central Java, Indonesia): an outline of the structural and magmatological evolution, with a special emphasis to the major pyroclastic events. *Journal of Volcanology and Geothermal Research* **100**, 139–163.

Caricchi, L., Sheldrake, T. E. & Blundy, J. (2018). Modulation of magmatic processes by CO2 flushing. Earth and Planetary Science Letters **491**, 160–171.

Carr, B. B., Clarke, A. B. & de' Michieli Vitturi, M. (2018). Earthquake induced variations in extrusion rate: a numerical modeling approach to the 2006 eruption of Merapi Volcano (Indonesia). *Earth and Planetary Science Letters* **482**, 377–387.

Carr, B. B., Clarke, A. B. & de' Michieli Vitturi, M. (2020). Volcanic conduit controls on effusive-explosive transitions and the 2010 eruption of Merapi Volcano (Indonesia). *Journal of Volcanology and Geothermal Research* **392**, 106767.

Carroll, M. R. & Rutherford, M. J. (1987). The stability of igneous anhydrite: experimental results and implications for sulfur

behavior in the 1982 El Chichon trachyandesite and other evolved magmas. *Journal of Petrology* **28**, 781–801.

Carter, L. B. & Dasgupta, R. (2015). Hydrous basalt–limestone interaction at crustal conditions: implications for generation of ultracalcic melts and outflux of CO_2 at volcanic arcs. *Earth and Planetary Science Letters* **427**, 202–214.

Carter, L. B. & Dasgupta, R. (2016). Effect of melt composition on crustal carbonate assimilation: implications for the transition from calcite consumption to skarnification and associated CO_2 degassing. *Geochemistry, Geophysics, Geosystems* **17**, 3893–3916.

Carter, L. B. & Dasgupta, R. (2018). Decarbonation in the Ca-Mg-Fe carbonate system at mid-crustal pressure as a function of temperature and assimilation with arc magmas–Implications for long-term climate. *Chemical Geology* **492**, 30–48.

Chadwick, J. P., Troll, V. R., Ginibre, C., Morgan, D., Gertisser, R., Waight, T. E. & Davidson, J. P. (2007). Carbonate assimilation at Merapi Volcano, Java, Indonesia: insights from crystal isotope stratigraphy. *Journal of Petrology* **48**, 1793–1812.

Chadwick, J. P., Troll, V. R., Waight, T. E., van der Zwan, F. M. & Schwarzkopf, L. M. (2013). Petrology and geochemistry of igneous inclusions in recent Merapi deposits: a window into the sub-volcanic plumbing system. *Contributions to Mineralogy and Petrology* **165**, 259–282.

Charlu, T. V., Newton, R. C. & Kleppa, O. J. (1981). Thermochemistry of synthetic $Ca_2Al_2SiO_7$ (gehlenite)-$Ca_2MgSi_2O_7$ (åkermanite) melilites. *Geochimica et Cosmochimica Acta* **45**, 1609–1617.

Clocchiatti, R., Joron, J. L., Kerinec, F. & Treuil, M. (1982). Quelques données préliminaires sur la lave du dôme actuel du volcan Mérapi (Java, Indonésie) et sur ses enclaves. *Comptes rendus de l'Académie des Sciences Paris* **295**, 817–822.

Commer, M., Helwig, S. L., Hördt, A., Scholl, C. & Tezkan, B. (2006). New results on the resistivity structure of Merapi Volcano (Indonesia), derived from three-dimensional restricted inversion of long-offset transient electromagnetic data. *Geophysical Journal International* **167**, 1172–1187.

Conte, A. M., Dolfi, D., Gaeta, M., Misiti, V., Mollo, S. & Perinelli, C. (2009). Experimental constraints on evolution of leucite-basanite magma at 1 and 10^{-4} GPa: implications for parental compositions of Roman high-potassium magmas. *European Journal of Mineralogy* **21**, 763–782.

Cortés, J. A., Wilson, M., Condliffe, E. & Francalanci, L. (2006). The occurrence of forsterite and highly oxidizing conditions in basaltic lavas from Stromboli volcano, *Italy. Journal of Petrology* **47**, 1345–1373.

Costa, F., Andreastuti, S., Bouvet de Maisonneuve, C. & Pallister, J. S. (2013). Petrological insights into the storage conditions, and magmatic processes that yielded the centennial 2010 Merapi explosive eruption. *Journal of Volcanology and Geothermal Research* **261**, 209–235.

Danyushevsky, L., Della-Pasqua, F. & Sokolov, S. (2000). Re-equilibration of melt inclusions trapped by magnesian olivine phenocrysts from subduction-related magmas: petrological implications. *Contributions to Mineralogy and Petrology* **138**, 68–83.

de Capitani, C. & Petrakakis, K. (2010). The computation of equilibrium assemblage diagrams with Theriak/Domino software. *American Mineralogist* **95**, 1006–1016.

Deegan, F. M., Troll, V. R., Freda, C., Misiti, V. & Chadwick, J. P. (2011). Fast and furious: crustal CO_2 release at Merapi volcano, *Indonesia. Geology Today* **27**, 63–64.

Deegan, F. M., Troll, V. R., Freda, C., Misiti, V., Chadwick, J. P., McLeod, C. L. & Davidson, J. P. (2010). Magma–carbonate interaction processes and associated CO_2 release at Merapi Volcano, Indonesia: insights from experimental petrology. *Journal of Petrology* **51**, 1027–1051.

Deegan, F. M., Troll, V. R., Whitehouse, M. J., Jolis, E. M. & Freda, C. (2016a). Boron isotope fractionation in magma via crustal carbonate dissolution. *Scientific Reports* **6**, 30774.

Deegan, F. M., Whitehouse, M. J., Troll, V. R., Budd, D. A., Harris, C., Geiger, H. & Hålenius, U. (2016b). Pyroxene standards for SIMS oxygen isotope analysis and their application to Merapi volcano, Sunda arc, Indonesia. *Chemical Geology* **447**, 1–10.

Deer, W. A., Howie, R. A. & Zussman, J. (1997). *Rock-Forming Minerals. Single-Chain Silicates, Volume 2A*, 2nd edn. London: The Geological Society.

Del Moro, S., Renzulli, A. & Tribaudino, M. (2011). Pyrometamorphic processes at the magma–hydrothermal system interface of active volcanoes: evidence from buchite ejecta of Stromboli (Aeolian Islands, Italy). *Journal of Petrology* **52**, 541–564.

Devine, J. D., Gardner, J. E., Brack, H. P., Laynet, G. D. & Rutherford, M. J. (1995). Comparison of microanalytical methods for estimating H_2O contents of silicic volcanic glasses. *American Mineralogist* **80**, 319–328.

Di Rocco, T., Freda, C., Gaeta, M., Mollo, S. & Dallai, L. (2012). Magma chambers emplaced in carbonate substrate: petrogenesis of skarn and cumulate rocks and implications for CO_2 degassing in volcanic areas. *Journal of Petrology* **53**, 2307–2332.

Droop, G. (1987). A general equation for estimating Fe^{3+} concentrations in ferromagnesian silicates and oxides from microprobe analyses, using stoichiometric criteria. *Mineralogical Magazine* **51**, 431–435.

Erdmann, S., Martel, C., Pichavant, M., Bourdier, J.-L., Champallier, R., Komorowski, J.-C. & Cholik, N. (2016). Constraints from phase equilibrium experiments on pre-eruptive storage conditions in mixed magma systems: a case study on crystal-rich basaltic andesites from Mount Merapi, *Indonesia. Journal of Petrology* **57**, 535–560.

Erdmann, S., Martel, C., Pichavant, M. & Kushnir, A. (2014). Amphibole as an archivist of magmatic crystallization conditions: problems, potential, and implications for inferring magma storage prior to the paroxysmal 2010 eruption of Mount Merapi, *Indonesia. Contributions to Mineralogy and Petrology* **167**, 1016.

Feig, S. T., Koepke, J. & Snow, J. E. (2006). Effect of water on tholeiitic basalt phase equilibria: an experimental study under oxidizing conditions. *Contributions to Mineralogy and Petrology* **152**, 611–638.

Feig, S. T., Koepke, J. & Snow, J. E. (2010). Effect of oxygen fugacity and water on phase equilibria of a hydrous tholeiitic basalt. *Contributions to Mineralogy and Petrology* **160**, 551–568.

Freda, C., Gaeta, M., Giaccio, B., Marra, F., Palladino, D. M., Scarlato, P. & Sottili, G. (2011). CO_2-driven large mafic explosive eruptions: the Pozzolane Rosse case study from the Colli Albani Volcanic District (Italy). *Bulletin of Volcanology* **73**, 241–256.

Freise, M., Holtz, F., Nowak, M., Scoates, J. S. & Strauss, H. (2009). Differentiation and crystallization conditions of basalts from the Kerguelen large igneous province: an experimental study. *Contributions to Mineralogy and Petrology* **158**, 505.

Frezzotti, M.-L., Andersen, T., Neumann, E.-R. & Simonsen, S. L. (2002). Carbonatite melt–CO_2 fluid inclusions in mantle xenoliths from Tenerife, Canary Islands: a story of trapping, immiscibility and fluid–rock interaction in the upper mantle. *Lithos* **64**, 77–96.

Frezzotti, M.-L., Peccerillo, A., Zanon, V. & Nikogosian, I. (2004). Silica-rich melts in quartz xenoliths from Vulcano Island and their bearing on processes of crustal anatexis and crust–magma interaction beneath the Aeolian Arc, Southern Italy. *Journal of Petrology* **45**, 3–26.

Frost, B.R. (1991). Introduction to oxygen fugacity and its petrologic importance. *Reviews in Mineralogy and Geochemistry* **25**, 1–9.

Fujita, S., Suzuki, K., Ohkawa, M., Shibasaki, Y. & Mori, T. (2001). Reaction of hydrogrossular with hydrogen chloride gas at high temperature. *Chemistry of Materials* **13**, 2523–2527.

Fulignati, P., Kamenetsky, V. S., Marianelli, P. & Sbrana, A. (2013). PIXE mapping on multiphase fluid inclusions in endoskarn xenoliths of AD 472 eruption of Vesuvius (Italy). *Periodico di Mineralogia* **82**, 291–297.

Fulignati, P., Kamenetsky, V. S., Marianelli, P., Sbrana, A. & Mernagh, T. P. (2001). Melt inclusion record of immiscibility between silicate, hydrosaline, and carbonate melts: applications to skarn genesis at Mount Vesuvius. *Geology* **29**, 1043–1046.

Fulignati, P., Marianelli, P., Santacroce, R. & Sbrana, A. (2004). Probing the Vesuvius magma chamber–host rock interface through xenoliths. *Geological Magazine* **141**, 417–428.

Gaeta, M., Rocco, T. D. & Freda, C. (2009). Carbonate assimilation in open magmatic systems: the role of melt-bearing skarns and cumulate-forming processes. *Journal of Petrology* **50**, 361–385.

Galuskin, E. V., Galuskina, I. O., Bailau, R., Prusik, K., Gazeev, V. M., Zadov, A. E., Pertsev, N. N., Jeżak, L., Gurbanov, A. G. & Dubrovinsky, L. (2013). Eltyubyuite, $Ca_{12}Fe^{3+}_{10}Si_4O_{32}Cl_6$–the Fe^{3+} analogue of wadalite: a new mineral from the Northern Caucasus, Kabardino-Balkaria, Russia. *European Journal of Mineralogy* **25**, 221–229.

Galuskin, E. V., Gfeller, F., & Galuskina, I. O., Armbruster, T., Bailau, R. & Sharygin, V. V. (2015). Mayenite supergroup, part I: recommended nomenclature. *European Journal of Mineralogy* **27**, 99–111.

Ganino, C., Arndt, N. T., Zhou, M.-F., Gaillard, F. & Chauvel, C. (2008). Interaction of magma with sedimentary wall rock and magnetite ore genesis in the Panzhihua mafic intrusion, SW China. *Mineralium Deposita* **43**, 677–694.

Gertisser, R. (2001). Gunung Merapi (Java, Indonesien): Eruptionsgeschichte und magmatische Evolution eines Hochrisiko-Vulkans. Ph.D. thesis, University of Freiburg, Freiburg, Germany.

Gertisser, R., Charbonnier, S. J., Keller, J. & Quidelleur, X. (2012). The geological evolution of Merapi volcano, Central Java, Indonesia. *Bulletin of Volcanology* **74**, 1213–1233.

Gertisser, R., Charbonnier, S. J., Troll, V. R., Keller, J., Preece, K., Chadwick, J., Barclay, J. & Herd, R. (2011). Merapi (Java, Indonesia): anatomy of a killer volcano. *Geology Today* **27**, 57–62.

Gertisser, R. & Keller, J. (2003a). Temporal variations in magma composition at Merapi Volcano (Central Java, Indonesia): magmatic cycles during the past 2000 years of explosive activity. *Journal of Volcanology and Geothermal Research* **123**, 1–23.

Gertisser, R. & Keller, J. (2003b). Trace element and Sr, Nd, Pb and O isotope variations in medium-K and high-K volcanic rocks from Merapi Volcano, Central Java, Indonesia: evidence for the involvement of subducted sediments in Sunda arc magma genesis. *Journal of Petrology* **44**, 457–489.

Ghiorso, M.S. (2016). Modeling carbonate assimilation into crustal magmas: Quantifying overpressure and eruption triggers. *Goldschmidt Conference Abstracts 934*, Yokohama, Japan.

Glasser, F. (1995). Comments on wadalite, $Ca_6Al_5Si_2O_{16}Cl_3$, and the structures of garnet, mayenite and calcium chlorosilicate. Addendum. *Acta Crystallographica Section C: Crystal Structure Communications* **51**, 340.

Goff, F., Love, S. P., Warren, R. G., Counce, D., Obenholzner, J., Siebe, C. & Schmidt, S. C. (2001). Passive infrared remote sensing evidence for large, intermittent CO_2 emissions at Popocatépetl volcano, Mexico. *Chemical Geology* **177**, 133–156.

Goldstein, R. H. (2003). Petrographic analysis of fluid inclusions. In: Samson, I., Anderson, A. & Marshall, D. (eds), *Fluid Inclusions: Analysis and Interpretation, Mineral Association of Canada Short Course.* Vancouver: Mineralogical Association of Canada, pp. 9–53.

Gordon, T. M. & Greenwood, H. J. (1971). The stability of grossularite in H_2O-CO_2 mixtures. *American Mineralogist* **56**, 1674–1688.

Gorzkowska, I., Maciejewski, M. & Rudnicki, R. (1988a). Thermal decomposition of $CaCO_3$ in the presence of calcium fluoride. *Journal of Thermal Analysis and Calorimetry* **33**, 983–990.

Gorzkowska, I., Maciejewski, M. & Rudnicki, R. (1988b). Application of DTA and TG to studies of the $CaCO_3$-CaF_2 phase diagram. *Journal of Thermal Analysis and Calorimetry* **33, 991-995.**

Grew, E. S., Locock, A. J., Mills, S. J., Galuskina, I. O., Galuskin, E. V. & Hålenius, U. (2013). Nomenclature of the garnet supergroup. *American Mineralogist* **98**, 785–811.

Gualda, G. A., Ghiorso, M. S., Lemons, R. V. & Carley, T. L. (2012). Rhyolite-MELTS: a modified calibration of MELTS optimized for silica-rich, fluid-bearing magmatic systems. *Journal of Petrology* **53**, 875–890.

Gustafson, W.I. (1974). The stability of andradite, hedenbergite, and related minerals in the system Ca-Fe-Si-O-H. *Journal of Petrology* **15**, 455–496.

Handley, H. K., Blichert-Toft, J., Gertisser, R., Macpherson, C. G., Turner, S. P., Zaennudin, A. & Abdurrachman, M. (2014). Insights from Pb and O isotopes into along-arc variations in subduction inputs and crustal assimilation for volcanic rocks in Java, Sunda arc, Indonesia. *Geochimica et Cosmochimica Acta* **139**, 205–226.

Hansteen, T.H. & Klügel, A. (2008). Fluid inclusion thermobarometry as a tracer for magmatic processes. *Reviews in Mineralogy and Geochemistry* **69**, 143–177.

Hartley, M. E., Bali, E., Maclennan, J., Neave, D. A. & Halldórsson, S. A. (2018). Melt inclusion constraints on petrogenesis of the 2014–2015 Holuhraun eruption, Iceland. *Contributions to Mineralogy and Petrology* **173**, 10.

Hattori, K. (2018). Porphyry copper potential in Japan based on magmatic oxidation state. *Resource Geology* **68**, 126–137.

Henmi, C. & Henmi, K. (1978). Synthesis of spurrite and tilleyite at low CO_2 partial pressure. *Mineralogical Journal* **9**, 106–110.

Hirschmann, M., Ghiorso, M., Davis, F., Gordon, S., Mukherjee, S., Grove, T., Krawczynski, M., Medard, E. & Till, C. (2008). Library of Experimental Phase Relations (LEPR): a database and Web portal for experimental magmatic phase equilibria data. *Geochemistry, Geophysics, Geosystems* **9**, Q03011.

Holland, T. J. B. & Powell, R. (1998). An internally consistent thermodynamic data set for phases of petrological interest. *Journal of Metamorphic Geology* **16**, 309–343.

Huckenholz, H., Lindhuber, W. & Springer, J. (1974). The join $CaSiO_3$-Al_2O_3-Fe_2O_3 of the CaO-Al_2O_3-Fe_2O_3-SiO_2 quaternary system and its bearing on the formation of granditic garnets and fassaitic pyroxenes. *Neues Jahrbuch fur Mineralogie, Abhandlungen* **121**, 160–207.

Iacono-Marziano, G., Gaillard, F. & Pichavant, M. (2007). Limestone assimilation and the origin of CO_2 emissions at the Alban Hills (Central Italy): constraints from experimental petrology. *Journal of Volcanology and Geothermal Research* **166**, 91–105.

Iacono-Marziano, G., Gaillard, F. & Pichavant, M. (2008). Limestone assimilation by basaltic magmas: an experimental re-assessment and application to Italian volcanoes. *Contributions to Mineralogy and Petrology* **155**, 719–738.

Innocenti, S., del Marmol, M.-A., Voight, B., Andreastuti, S. & Furman, T. (2013). Textural and mineral chemistry constraints on evolution of Merapi Volcano, *Indonesia. Journal of Volcanology and Geothermal Research* **261**, 20–37.

Jago, B. C. & Gittins, J. (1991). The role of fluorine in carbonatite magma evolution. *Nature* **349**, 56–58.

Joesten, R. (1974). Local equilibrium and metasomatic growth of zoned calc-silicate nodules from a contact aureole, Christmas Mountains, Big Bend region, Texas. *American Journal of Science* **274**, 876–901.

Jolis, E. M., Freda, C., Troll, V. R., Deegan, F. M., Blythe, L. S., McLeod, C. L. & Davidson, J. P. (2013). Experimental simulation of magma–carbonate interaction beneath Mt. Vesuvius, Italy. *Contributions to Mineralogy and Petrology* **166**, 1335–1353.

Jolis, E., Troll, V., Harris, C., Freda, C., Gaeta, M., Orsi, G. & Siebe, C. (2015). Skarn xenolith record crustal CO_2 liberation during Pompeii and Pollena eruptions, Vesuvius volcanic system, central Italy. *Chemical Geology* **415**, 17–36.

Kerinec, F. (1982). Le Mérapi, volcan actif d'arc insulaire (Java): Pétrographie et géochimie des matériaux solides; *implications géotectoniques*. Ph.D. thesis, Université Paris-Sud, Orsay, France.

Kilgour, G. N., Saunders, K. E., Blundy, J. D., Cashman, K. V., Scott, B. J. & Miller, C. A. (2014). Timescales of magmatic processes at Ruapehu volcano from diffusion chronometry and their comparison to monitoring data. *Journal of Volcanology and Geothermal Research* **288**, 62–75.

Kokh, M. A., Akinfiev, N. N., Pokrovski, G. S., Salvi, S. & Guillaume, D. (2017). The role of carbon dioxide in the transport and fractionation of metals by geological fluids. *Geochimica et Cosmochimica Acta* **197**, 433–466.

Komorowski, J.-C., Jenkins, S., Baxter, P. J., Picquout, A., Lavigne, F., Charbonnier, S., Gertisser, R., Preece, K., Cholik, N. & Budi-Santoso, A. (2013). Paroxysmal dome explosion during the Merapi 2010 eruption: processes and facies relationships of associated high-energy pyroclastic density currents. *Journal of Volcanology and Geothermal Research* **261**, 260–294.

Kouchi, A., Sugawara, Y., Kashima, K. & Sunagawa, I. (1983). Laboratory growth of sector zoned clinopyroxenes in the system $CaMgSi_2O_6$-$CaTiAl_2O_6$. *Contributions to Mineralogy and Petrology* **83**, 177–184.

Landtwing, M. R., Pettke, T., Halter, W. E., Heinrich, C. A., Redmond, P. B., Einaudi, M. T. & Kunze, K. (2005). Copper deposition during quartz dissolution by cooling magmatic–hydrothermal fluids: the Bingham porphyry. *Earth and Planetary Science Letters* **235**, 229–243.

Lindsley, D. H. (1983). Pyroxene thermometry. *American Mineralogist* **68**, 477–493.

Luhr, J. F. (2008). Primary igneous anhydrite: progress since its recognition in the 1982 El Chichón trachyandesite. *Journal of Volcanology and Geothermal Research* **175**, 394–407.

Mason, E., Edmonds, M. & Turchyn, A. V. (2017). Remobilization of crustal carbon may dominate volcanic arc emissions. *Science* **357**, 290–294.

Matthews, S., Marquillas, R., Kemp, A., Grange, F. & Gardeweg, M. (1996). Active skarn formation beneath Lascar Volcano, northern Chile: a petrographic and geochemical study of xenoliths in eruption products. *Journal of Metamorphic Geology* **14**, 509–530.

Mavrogenes, J. & Blundy, J. (2017). Crustal sequestration of magmatic sulfur dioxide. *Geology* **45**, 211–214.

Meinert, L. D. (1992). Skarns and skarn deposits. *Geoscience Canada* **19**, 145–162.

Meinert, L. D., Dipple, G. M. & Nicolescu, S. (2005). World skarn deposits. In: Hedenquist, J. W., Thompson, J. F. H., Goldfarb, R. J. & Richards, J. P. (eds) *Economic Geology One Hundredth Anniversary Volume*. Littleton, Colorado, pp. 299–336.

Melluso, L., Conticelli, S., D'Antonio, M., Mirco, N. P. & Saccani, E. (2003). Petrology and mineralogy of wollastonite-and melilite-bearing paralavas from the Central Apennines, *Italy. American Mineralogist* **88**, 1287–1299.

Mollo, S., Blundy, J. D., Giacomoni, P., Nazzari, M., Scarlato, P., Coltorti, M., Langone, A. & Andronico, D. (2017). Clinopyroxene-melt element partitioning during interaction between trachybasaltic magma and siliceous crust: clues from quartzite enclaves at Mt. Etna volcano. *Lithos* **284**, 447–461.

Mollo, S., Gaeta, M., Freda, C., Di Rocco, T., Misiti, V. & Scarlato, P. (2010). Carbonate assimilation in magmas: a reappraisal based on experimental petrology. *Lithos* **114**, 503–514.

Mollo, S., Heap, M. J., Iezzi, G., Hess, K. U., Scarlato, P. & Dingwell, D. B. (2012). Volcanic edifice weakening via decarbonation: a self-limiting process? *Geophysical Research Letters*, **39**, L15307.

Mollo, S., Putirka, K., Iezzi, G., Del Gaudio, P. & Scarlato, P. (2011). Plagioclase–melt (dis) equilibrium due to cooling dynamics: implications for thermometry, barometry and hygrometry. *Lithos* **125**, 221–235.

Mollo, S., Putirka, K., Misiti, V., Soligo, M. & Scarlato, P. (2013). A new test for equilibrium based on clinopyroxene–melt pairs: clues on the solidification temperatures of Etnean alkaline melts at post-eruptive conditions. *Chemical Geology* **352**, 92–100.

Mollo, S. & Vona, A. (2014). The geochemical evolution of clinopyroxene in the Roman Province: a window on decarbonation from wall-rocks to magma. *Lithos* **192**, 1–7.

Morimoto, N. (1988). Nomenclature of pyroxenes. *Mineralogy and Petrology* **39**, 55–76.

Muhling, J. R. & Griffin, B. J. (1991). On recasting garnet analyses into end-member molecules—revisited short note. *Computers & Geosciences* **17**, 161–170.

Nadeau, O., Stix, J. & Williams-Jones, A. E. (2013a). The behavior of Cu, Zn and Pb during magmatic–hydrothermal activity at Merapi volcano, Indonesia. *Chemical Geology* **342**, 167–179.

Nadeau, O., Williams-Jones, A. E. & Stix, J. (2013b). Magmatic-hydrothermal evolution and devolatilization beneath Merapi volcano, *Indonesia. Journal of Volcanology and Geothermal Research* **261**, 50–68.

Nadeau, O., Williams-Jones, A.E. & Stix, J. (2010). Sulphide magma as a source of metals in arc-related magmatic hydrothermal ore fluids. *Nature Geoscience* **3**, 501–505.

Nakamura, M. & Shimakita, S. (1998). Dissolution origin and syn-entrapment compositional change of melt inclusion in plagioclase. *Earth and Planetary Science Letters* **161**, 119–133.

Neave, D. A. & Putirka, K. (2017). A new clinopyroxene-liquid barometer, and implications for magma storage pressures under Icelandic rift zones. *American Mineralogist* **102**, 777–794.

Newhall, C., Bronto, S., Alloway, B., Banks, N., Bahar, I., Marmol, M. D., Hadisantono, R., Holcomb, R., McGeehin, J. & Miksic, J. (2000). 10,000 years of explosive eruptions of Merapi Volcano, Central Java: archaeological and modern implications. *Journal of Volcanology and Geothermal Research* **100**, 9–50.

Nicholls, I. (1971). Calcareous inclusions in lavas and agglomerates of Santorini volcano. *Contributions to Mineralogy and Petrology* **30**, 261–276.

Nielsen, R. L. (2011). The effects of re-homogenization on plagioclase hosted melt inclusions. *Geochemistry, Geophysics, Geosystems* **12**, Q0AC17.

Orlando, A., D'Orazio, M., Armienti, P. & Borrini, D. (2008). Experimental determination of plagioclase and clinopyroxene crystal growth rates in an anhydrous trachybasalt from Mt Etna (Italy). *European Journal of Mineralogy* **20**, 653–664.

Parat, F., Holtz, F. & Streck, M. J. (2011). Sulfur-bearing magmatic accessory minerals. *Reviews in Mineralogy and Geochemistry* **73**, 285–314.

Pascal, M.-L., Di Muro, A., Fonteilles, M. & Principe, C. (2009). Zirconolite and calzirtite in banded forsterite-spinel-calcite skarn ejecta from the 1631 eruption of Vesuvius: inferences for magma-wallrock interactions. *Mineralogical Magazine* **73**, 333–356.

Pascal, M.-L., Katona, I., Fonteilles, M. & Verkaeren, J. (2005). Relics of high-temperature clinopyroxene on the join di–cats with up to 72 mol.% $Ca(Al,Fe^{3+})AlSiO_6$ in the skarns of Ciclova and Magureaua Vatei, Carpathians, Romania. *Canadian Mineralogist* **43, 857-881.**

Povoden, E., Horacek, M. & Abart, R. (2002). Contact metamorphism of siliceous dolomite and impure limestones from the Werfen formation in the eastern Monzoni contact aureole. *Mineralogy and Petrology* **76**, 99–120.

Preece, K. (2014). Transitions between effusive and explosive activity at Merapi volcano, Indonesia: a volcanological and petrological study of the 2006 and 2010 eruptions. Ph.D. thesis, University of East Anglia, Norwich, UK.

Preece, K., Gertisser, R., Barclay, J., Berlo, K. & Herd, R. A. (2014). Pre-and syn-eruptive degassing and crystallisation processes of the 2010 and 2006 eruptions of Merapi volcano, *Indonesia. Contributions to Mineralogy and Petrology* **168**, 1–25.

Preece, K., Gertisser, R., Barclay, J., Charbonnier, S. J., Komorowski, J.-C. & Herd, R. A. (2016). Transitions between explosive and effusive phases during the cataclysmic 2010 eruption of Merapi volcano, Java, Indonesia. *Bulletin of Volcanology* **78**, 54.

Putirka, K. (2008). Thermometers and barometers for volcanic systems. *Reviews in Mineralogy and Geochemistry* **69**, 61–120.

Putirka, K. (1999). Clinopyroxene+liquid equilibria to 100 kbar and 2450 K. *Contributions to Mineralogy and Petrology* **135**, 151–163.

Putirka, K., Johnson, M., Kinzler, R., Longhi, J. & Walker, D. (1996). Thermobarometry of mafic igneous rocks based on clinopyroxene-liquid equilibria, 0–30 kbar. *Contributions to Mineralogy and Petrology* **123**, 92–108.

Reagan, M., Handley, H., Gertisser, R., Turner, M., Berlo, K. & Preece, K. (2017). U-series evidence for ongoing skarnification beneath Merapi Volcano, Indonesia. *IAVCEI 2017 Conference Abstracts*. Portland, OR, p. 883.

Roedder, E., 1984. *Fluid Inclusions*. *Reviews in Mineralogy Volume 12*. Washington: Mineralogical Society of America.

Rutstein, M. S. (1971). Re-examination of the wollastonite-hedenbergite ($CaSiO_3$-$CaFeSi_2O_6$) equilibria. *American Mineralogist* **56**, 2040–2052.

Rutstein, M. S. & White, W. B. (1971). Vibrational spectra of high-calcium pyroxenes and pyroxenoids. *American Mineralogist* **56**, 877–887.

Schwarzkopf, L., Schmincke, H.-U. & Troll, V. (2001). Pseudotachylite on impact marks of block surfaces in block-and-ash flows at Merapi volcano, Central Java, Indonesia. *International Journal of Earth Sciences* **90**, 769–775.

Sillitoe, R. H. (2010). Porphyry copper systems. *Economic Geology* **105**, 3–41.

Simakin, A. G., Salova, T. P. & Armienti, P. (2003). Kinetics of clinopyroxene growth from a hydrous hawaiite melt. *Geochemistry International* **41**, 1165–1175.

Simakin, A., Salova, T. & Bondarenko, G. (2012). Experimental study of magmatic melt oxidation by CO_2. *Petrology* **20**, 593–606.

Smyth, H., Hall, R., Hamilton, J. & Kinny, P. (2005). East Java: Cenozoic basins, volcanoes and ancient basement. In: 30th Annual Convention of the Indonesian Petroleum Association, Jakarta, Indonesia: Indonesian Petroleum Association, pp. 251–266.

Sobolev, V. N., McCammon, C. A., Taylor, L. A., Snyder, G. A. & Sobolev, N. V. (1999). Precise Moessbauer milliprobe determination of ferric iron in rock-forming minerals and limitations of electron microprobe analysis. *American Mineralogist* **84**, 78–85.

Span, R. & Wagner, W. (1996). A new equation of state for carbon dioxide covering the fluid region from the triple-point temperature to 1100 K at pressures up to 800 MPa. *Journal of Physical and Chemical Reference Data* **25**, 1509–1596.

Spandler, C., Martin, L.H. & Pettke, T. (2012). Carbonate assimilation during magma evolution at Nisyros (Greece), South Aegean Arc: Evidence from clinopyroxenite xenoliths. *Lithos* **146**, 18–33.

Sterner, S. M. & Pitzer, K. S. (1994). An equation of state for carbon dioxide valid from zero to extreme pressures. *Contributions to Mineralogy and Petrology* **117**, 362–374.

Sugawara, T. (2001). Ferric iron partitioning between plagioclase and silicate liquid: thermodynamics and petrological applications. *Contributions to Mineralogy and Petrology* **141**, 659–686.

Sun, W., Liang, H., Ling, M., Zhan, M., Ding, X., Zhang, H., Yang, X., Li, Y., Ireland, T. R., Wei, Q. & Fan, W. (2013). The link between reduced porphyry copper deposits and oxidized magmas. *Geochimica et Cosmochimica Acta* **103**, 263–275.

Surono, M., Jousset, P., Pallister, J., Boichu, M., Fabrizia, M., Buongiorno, A. B., Rodriguez, F. C., Andreastuti, S., Prata, F. & Schneider, D. (2012). The 2010 explosive eruption of Java's Merapi volcano – a '100-year' event. *Journal of Volcanology and Geothermal Research* **241–242**, 121–135.

Tamic, N., Behrens, H. & Holtz, F. (2001). The solubility of H_2O and CO_2 in rhyolitic melts in equilibrium with a mixed CO_2–H_2O fluid phase. *Chemical Geology*, **174**, 333–347.

Tracy, R. J. & Frost, B. R. (1991). Phase equilibria and thermobarometry of calcareous, ultramafic and mafic rocks, and iron formations. *Reviews in Mineralogy and Geochemistry* **26**, 207–289.

Treiman, A. H. & Essene, E. J. (1983). Phase equilibria in the system CaO-SiO_2-CO_2. *American Journal of Science* **283**, 97–120.

Troll, V. R., Deegan, F. M., Jolis, E. M., Harris, C., Chadwick, J. P., Gertisser, R., Schwarzkopf, L. M., Borisova, A. Y., Bindeman, I. N. & Sumarti, S. (2013). Magmatic differentiation processes at Merapi Volcano: inclusion petrology and oxygen isotopes. *Journal of Volcanology and Geothermal Research* **261**, 38–49.

Troll, V. R., Hilton, D. R., Jolis, E. M., Chadwick, J. P., Blythe, L. S., Deegan, F. M., Schwarzkopf, L. M. & Zimmer, M. (2012). Crustal CO_2 liberation during the 2006 eruption and earthquake events at Merapi volcano, *Indonesia. Geophysical Research Letters* **39, L11302.**

Tuttle, O. F. & Harker, R. I. (1957). Synthesis of spurrite and the reaction wollastonite+calcite $\rightleftharpoons$ spurrite+carbon dioxide. *American Journal of Science* **255**, 226–234.

van Bemmelen, R. W. (1949). *The Geology of Indonesia*. The Hague: Government Printing Office.

van Hinsberg, V. J., Berlo, K., Migdisov, A. A. & Williams-Jones, A. E. (2016). CO_2-fluxing collapses metal mobility in magmatic vapour. *Geochemical Perspectives Letters* **2**, 169–177.

Voight, B., Constantine, E. K., Siswowidjoyo, S. & Torley, R. (2000). Historical eruptions of Merapi volcano, central Java, Indonesia, 1768–1998. *Journal of Volcanology and Geothermal Research* **100**, 69–138.

Wenzel, T., Baumgartner, L. P., Brügmann, G. E., Konnikov, E. G. & Kislov, E. V.(2002). Partial melting and assimilation of dolomitic xenoliths by mafic magma: the Ioko-Dovyren intrusion (North Baikal Region, Russia). *Journal of Petrology* **43**, 2049–2074.

Whitaker, M. L., Nekvasil, H., Lindsley, D. H. & Di Francesco, N. J. (2007). The role of pressure in producing compositional diversity in intraplate basaltic magmas. *Journal of Petrology* **48**, 365–393.

Whitley, S., Gertisser, R., Halama, R., Preece, K., Troll, V. R. & Deegan, F. M. (2019). Crustal CO_2 contribution to subduction zone degassing recorded through calc-silicate xenoliths in arc lavas. *Scientific Reports* **9, 8803.**

Wölbern, I. & Rümpker, G. (2016). Crustal thickness beneath Central and East Java (Indonesia) inferred from P receiver functions. *Journal of Asian Earth Sciences* **115**, 69–79.

Wyllie, P. J. & Haas, J. L. Jr (1965). The system CaO-SiO_2-CO_2-H_2O: 1. Melting relationships with excess vapor at 1 kilobar pressure. *Geochimica et Cosmochimica Acta* **29**, 871–892.

Zanon, V. & Nikogosian, I. (2004). Evidence of crustal melting events below the island of Salina (Aeolian arc, southern Italy). *Geological Magazine* **141**, 525–540.

Zarayskiy, G. P., Zharikov, V. A., Stoyanovskaya, F. M. & Balashov, V. N. (1987). The experimental study of bimetasomatic skarn formation. *International Geology Review* **29**, 629–758.

Zharikov, V. A. (1969). High temperature mineral equilibria in the system CaO-SiO_2-CO_2. *Geochemistry International* **6**, 853–869.